Numerical study on the behaviour of jointed rock under train loads

Jin Yan

A Thesis

In

The Department

of

Building, Civil, and Environment Engineering

Presented in Partial Fulfillment of the Requirements

For the Degree of

Master of Applied Science (Geotechnical Engineering) at

Concordia University

Montréal, Québec, Canada

October 2023

CONCORDIA UNIVERSITY

School of Graduate Studies

This is to certify that the thesis prepared

By: Jin Yan

Entitled: Numerical study on the behaviour of jointed rock under train loads

and submitted in partial fulfillment of the requirements for the degree of

Master of Applied Science (Geotechnical Engineering)

complies with regulations of the University and meets the accepted standards with respect to originality and quality.

Signed by the final Examining Committee:

_____ Chair

Dr. A. M. Hanna

_____ Examiner

Dr. A. Soliman

_____ Examiner

Dr. A. M. Hanna

_____ Supervisor

Dr. B. Li

Approved by _____

Dr. C. An Graduate Program Director

_____ 2023 _____

Dean of Faculty *Dr. M. Debbabi*

ABSTRACT

Numerical study on the behaviour of jointed rock under train loads

Jin Yan

Railway lines through mountainous terrain are frequently laid on jointed rock. Loads are transferred to the jointed rock component during the operation of high-axle heavy-haul freight trains, reducing the strength of the intact rock block and improving mobility. When a railway embankment is adjacent to a rock slope, failures in jointed rock mass can be triggered when the train load exceeds a specific level. Therefore, it is essential to investigate the impact of train speed on slope stability as well as the combination of pertinent factors that may cause embankment failure on jointed rock slopes. This research is conducted using the finite element shear strength reduction approach in two-dimensional models to analyze the slope stability of jointed rock and railway embankments under drainage conditions. A practical site is selected and related geomechanical parameters are retrieved from the literature. Various parameters are investigated for the relevant variables, including rock properties and joint characteristics. The crucial value for the factor of safety arising from the maximum safe train speed is set at 1.3 for all cases modeled. The maximum train speed is determined for cases with different joint orientations and joint spatial distributions. Cases for embankments sitting adjacent to slopes with different slope angles are also simulated and the corresponding maximum train speeds are established. Furthermore, this study also provides information on the slow speeds that can be adopted for different conditions to ensure the train safety.

Keywords: Jointed rock, slope stability, safe train speed, numerical modeling, safety factor

ACKNOWLEDGEMENTS

First and foremost, I would like to express my heartfelt thanks to my supervisor, Dr. Biao Li, for his selfless help, guidance, and advice throughout my master's studies, both in research and life.

I am grateful to my parents and friends for their support and encouragement during tough times, and the difficulties often dissipated in my communication with them.

Finally, I would like to express my gratitude to the examination committee for reading this thesis and providing critical comments. I also would like to acknowledge the financial support received from Dr. Zsaki through the ENCS FRS fund in the early stages of this study, which makes this research possible.

Table of Contents

List of Figures

List of Tables

List of Symbols

a_h	=	Asperity height
A	=	Bearing area of cross tie
b	=	Infill thickness
c	=	Cohesion
$c^{'}$	=	Effective cohesion
c^{*}	=	Reduced cohesion
C_d	=	Dispersion coefficient
C_s	=	Rock infills' stiffness coefficient
D	=	Disturbance factor
DF	=	Distribution factor of axle load carried by a single tie
E_s	=	Young's modulus of the joint infills
$F_{(i)}$	=	Internal force in the spring caused by its current deformed state
FS	=	Factor of safety
$\{F\}$	=	Vector of all incremental element nodal forces
$\{F\}_e$	=	Nodal load vector of the element
GSI	=	Geological Strength Index
h	=	Jointed rock slope height
$I_R\,, m_R\,, n_R$	=	Direction cosines of the mean orientation of the joint set
IF	=	Impact factor
K	=	Stiffness of the spring
$k_1,\ k_2$	=	Constants related to surface roughness and applied normal stress
K_n	=	Normal joint stiffness
K_s	=	Shear joint stiffness
$[k]$	=	Global elastic stiffness matrix
$[k]_e$	=	Element stiffness matrix
l	=	Joint length
L	=	Influence length of an axle load or adjacent axle loads
L_1, L_2	=	The length and height of the joint mapping area
L_{axle}	=	Two axle loads for train operation
L_s	=	The horizontal scan line of length
$\bar{l}$	=	Approximate average length of joints
m_b	=	Reduced value of the intact rock parameter
m_i	=	Intact rock constant
n	=	Step number
N_{app}	=	Number of discontinuities at the joints
N_c	=	Number of joints contained within the mapping region
N_t	=	Number of joints in the transect of the mapping region
$N^{'}$	=	Number of discontinuities
N''	=	Number of joints intersecting the scanline
p	=	Joint persistence

P	=	Applied load
P_0	=	The probability that the pole angle is not greater than the mean orientation
P_{avg}	=	Average ballast pressure
s	=	Joint spacing in RS2 models
S	=	True spacing of joints
S_{app}	=	Surface-mapped spacing of joints
$s_m,\ a$	=	Material constants which depend upon the characteristics of the rock mass
SD	=	Standard deviation
SRF	=	Stress reduction factor
$\bar{S}$	=	Average joint spacing
t	=	Loading pulse duration
T	=	Tensile strength
U	=	Displacement
ΔU	=	Displacement increment
u	=	Displacement in x direction
v	=	Train speed
α	=	Dip direction (dip azimuth)
α_R	=	Mean and standard deviation of dip direction
θ	=	Joint orientation
ϕ	=	Friction angle
ϕ^*	=	Internal friction angle
ψ	=	Dip angle
ψ_R	=	Mean and standard deviation of the dip
σ	=	Normal stress
σ_1	=	Major principal stress
σ_3	=	Minor principal stress
σ_{ci}	=	Uniaxial compressive strength
σ_n	=	Normal stress under the constant normal load condition
σ'	=	Effective stress
τ	=	Shear strength
τ_p	=	Peak shear strength of the infilled joint
τ_o	=	Peak shear strength of the clean joint
$\{\delta\}$	=	Vector of all incremental element nodal displacements
$\{\delta\}_e$	=	Nodal displacement vector of the element

Chapter 1 Introduction

1.1 Background

Canada, as a major industrial country, has manufacturing, agriculture, and tourism as the main pillars of the national economy, with transportation making a significant contribution since it ensures convenient travel for people and a smooth flow of products in the domestic and international markets. Indeed, the contribution of the transportation and warehousing industry to Canada's gross domestic product (GDP) has grown annually since 2011, with the annual GDP growth rate of the transportation industry exceeding the growth rate of the entire economy in the past five years (Transport Canada, 2020).

The railway system runs from east to west across Canada, and it also involves almost all economic industries in Canada. The passenger sector, including commuting, intercity, and tourism, is mainly operated by VIA Rail Canada Inc. More than four-fifths (83.5%) of Canadian rail freight routes are carried by Canadian National Railway Company (CN) and Canadian Pacific Railway Company (CP) (Transport Canada, 2018). It is mainly used for long-distance transportation of heavy goods, such as coal, grains, chemicals and building materials, which can be loaded into containers. Containers can quickly transfer goods from railways to airplanes, trucks or ships, making cargo transportation more efficient. Figure 1.1 shows Canada's total rail traffic flow in 2020 changed with the average of 2017–2019. Compared with the average of the previous three years, changes in rail traffic mainly reflect in the Atlantic Corridor region of Canada, where 5% of rail traffic growth areas are the most concentrated. On the routes from southern Ontario to the U.S. border and east to New Brunswick, most of the rail traffic remained unchanged or even dropped by more than 5%.

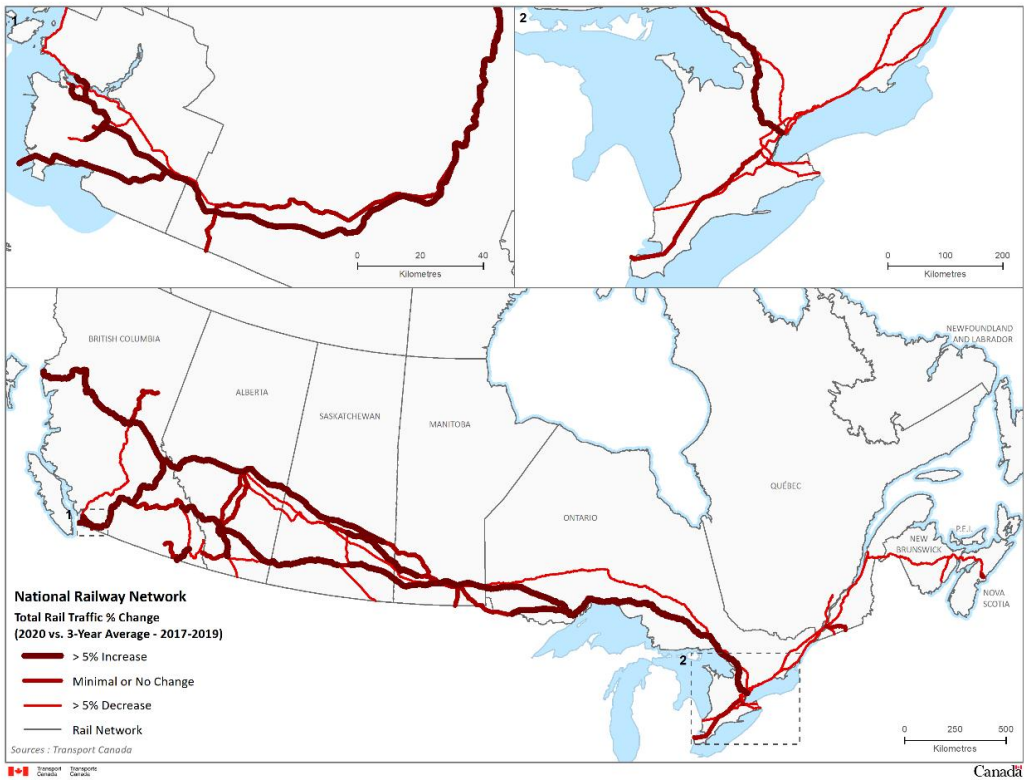

Figure 1.1 Rail system flow comparison (Transport Canada, 2020)

In the past 10 years, the number of railway accidents has changed year by year. Shown in Figure 1.2, there were about 1,100 rail accidents in 2010. In the following six years, railway accidents fluctuated downward and dropped to their lowest value in 2016 (just over 900). In the next three years, the number of railway traffic accidents increased rapidly. After reaching the highest value of 1,256 in 2019, this figure dropped to 965 in 2020, which was nonetheless more than one tenth of the average value from 2010 to 2020 (TSB, 2020). To cope with the potential safety hazards in the Canadian railway transportation system, the Transportation Safety Board collects and analyzes transportation accident data, improving railway transportation safety. The following two typical safety accidents are related to derailment caused by discontinuous rock joints during train operation.

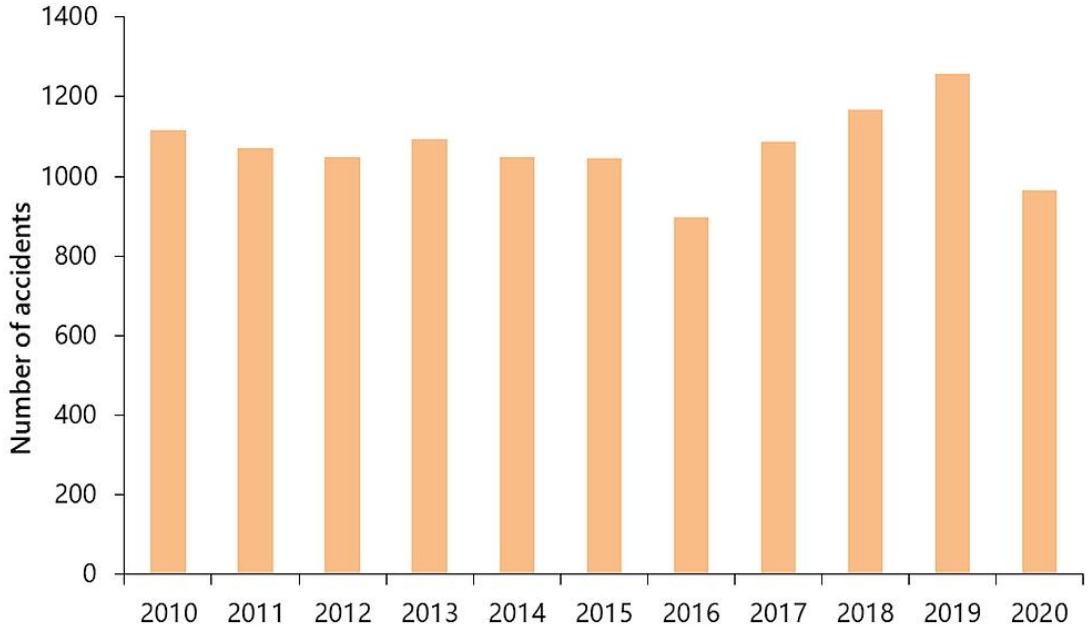

Figure 1.2 Rail accidents from 2010 to 2020 (TSB, 2020).

On January 20, 1995, Canadian Pacific Limited (CP) freight train No. 981-20 traveling from east to west derailed from a 125-foot-high rock cliff into a lake at Mile 111.0 of the Nelson Subdivision near Procter, British Columbia, mainly because it collided with falling rocks (TSB, 1996). The accident caused two people to drown, and another person was slightly injured. Part of the diesel oil that leaked into the lake was ignited; and some lead sulfide was leaked at the same time. Analysis shows that there was soil in the cracks on the rock surface. Due to the force generated by the roots of nearby plants and surface runoff, the crack network that appeared on the rock surface a few years prior gradually spread, and the rock's supporting force was insufficient, which led to failure with three locomotives and the first two cars behind the locomotive off track.

Another case occurred on the Quebec North Shore and Labrador Railway. The ore unit train BNL-212J suffered a derailment accident on November 6, 2014 (TSB, 2016). It ran to Mile 14.65 of the Wacouna Subdivision near Tellier, Quebec, where a rock slide caused the accident. The lead two locomotives led the following nine cars, which derailed and rolled sideways down the embankment into the Moisie River (Figure 1.3), inflicting severe injuries on the locomotive engineer. Around 1,000 liters of diesel fuel leaked in this incident, and about 100 ft of track were destroyed. Investigation at the scene revealed that during the buildup, the rock body where the slide occurred

fractured vertically, allowing water to flow out along the steep surface. The cut slope moved quickly along the sliding surface due to the expansion of the cracks. The front edge of the landslide body collapsed, and the train moved towards overturning on the left side.

Figure 1.3 The scene of ore train BNL-212J derailment accident (TSB, 2016).

The majority of these incidents are triggered by the formation and expansion of joints in the rock mass, which result in the collapse of a rock slope. The railway administration has strengthened the management of road maintenance personnel and expanded the scope of inspection of rocky slopes to create more systematic planning initiatives for reducing rock slope instability. Therefore, stability research on jointed rocks is crucial for secure railway operations. However, there are very limited literatures addressing the railway embankment stability under rock slopes. The present study is intended to carry out some preliminary investigation on this topic.

1.2 Research Objectives and Scope

The involvement of joints in rock is directly related to the strength of the rock mass and the slope stability. As a major component supporting embankment, the strength of rock mass determines to a large extent whether the embankment will be destroyed or not. When a train passes on a collapsed embankment, derailment is inevitable, which not only causes damage to the railway but also poses a great threat to the safety of people, property, and the surrounding environment. In this research, the geometry of the embankment, rock properties, joint spacing and orientation, are used as quantitative standards to obtain the maximum safe driving speed and maximum load capacity of high-axle heavy-haul freight trains on a given slope. The specific objectives are as follows:

- To determine the characteristics and external factors of the jointed rock that affect the stability of the railway embankment and the magnitude of the influencing factors.
- To develop a two-dimensional finite element model of the railway embankment on a slope with jointed rocks traversing mountainous terrains with different slope ratios.

- To explore the influence of different train speeds on the stability of railway embankments laid on jointed rocks.
- To confirm the maximum train speed and load allowed to travel on jointed rocks under different quantitative conditions.

This research does not consider any changes in the properties of the soil and rocks along the track and assumes that the train is moving in a straight line. In addition, the research models were analyzed under constant temperature conditions. The two-dimensional model of the infinitely long tangent segment in this research applies to all parts of the running train.

1.3 Research Methodology

An appropriate research methodology lends credibility to results by explaining the research process, data sources, and the adoption of appropriate data collection techniques. In this thesis, both qualitative and quantitative methods are used, including:

a. Collection and collation of existing references

Data of embankment geometry, rock properties, joint spacing and orientation, and trainloads should be obtained from the literature for a selected site.

b. FEM-based simulation using RS2 software

The impact factors studied in the literature review are input as basic parameters in the RS2 software. Different finite element railway embankment models are established for the research.

c. Parametric study

According to the influencing factors, two numerical model groups of the railway embankment are established, which are:

i. Set I: Jointed rock slope model beneath the railroad.

ii. Set II: Jointed rock slope model under moving train load conditions.

The *control variable method* is adopted to investigate each principal model parameter. A control group is set up for each model to eliminate the influence of other confounding factors on the numerical results. The changes of the following independent variables are controlled for each group of models, and parametric study is conducted on dependent variables that produce correlations including:

i. Various slope geometries are considered with different train loads, which are characterized by slope height, and slope ratio.

ii. Different joint spacing, orientations, and lengths are retained in the jointed rock.

d. Data analysis

Descriptive statistics are obtained of the data generated by each experimental model under different conditions, with group analysis and comparative analysis. Next, the correlation analysis of the data results of the overall parameter study investigates the stability tendency of railroad-jointed rock slopes under different conditions. The charts of the maximum safe train speed that can be sustained

by jointed rock mass embankments with different properties is developed.

In general, the finite element method (FEM) is applied to assess the stability of jointed rock mass slopes using deformation. Shear strength reduction (SSR) is one of the conventional finite element slope analysis methods (Hammah et al., 2005). A thorough evaluation of slope stability in jointed networks is performed.

1.4 Thesis Outline

The thesis is composed of five chapters. In this chapter, a background investigation is first completed to explain the pivotal importance of rail transportation in the Canadian transportation system. Then, two cases of train derailment accidents show that the gradual expansion of cracks in jointed rocks causes slope instability, which leads to the collapse of the subgrade under the train. Finally, the objectives, scope, and research methods are explained. A summary of the remaining chapters is provided below.

Chapter 2 presents a literature review, including the background of the jointed rock mass and the related content of using numerical methods to analyze slope stability. By studying the load transfer mechanism generated by the train passing on the rails, the critical factors that determine whether the railway embankment can be put into use are obtained to further study the relationship between these factors and the operation of freight trains. The next step is to compare slope stability analysis methods and determine the most suitable approach for this research. Furthermore, the constitutive models of rocks and infilling soil are described.

Chapter 3 delineates the development of the numerical models. In implementing the SSR method, the RS2 software is confirmed to be an effective modeling tool, especially for jointed rock masses.

Chapter 4 analyzes the parameters of the two groups of jointed rock mass and different loads. Additionally, it summarizes the correlation between the characteristics of jointed rocks under the railway embankment and slope stability considering the influence of the load on the model.

Chapter 5 presents conclusions, limitations and recommendations for future studies.

Chapter 2 Literature Review

2.0 Introduction

The stability of jointed rock slopes has received substantial attention. The goal of this research is to investigate the impacts of slope instability on jointed rock masses associated with moving loads generated by train operation, which is currently understudied. This chapter contains five sections that summarize the background of current related research to inform the parameter selection of the numerical model and the analysis approach in the later part of the thesis. The damage patterns induced by joints in rock slopes are first summarized, and the utility of the Monte Carlo approach for probabilistic slope instability analysis is proven. Following this, the load transmission mechanism on the rail from sleeper through ballast and subballast to the subgrade layer is discussed, as well as the ballast bearing load calculation method. The model parameters and methods for measuring slope stability are then described, demonstrating the benefits of using the finite element shear strength reduction (FE-SSR) method to analyze jointed rock slopes in this study. Finally, common rock constitutive models are presented that can be examined using the FEM.

2.1 Analysis for jointed rock masses

This section examines the mechanism of joint extension in rock masses and how it affects embankment slopes. In jointed rock engineering, analytical approaches for estimating failure probabilities using finite elements are reviewed. These are related to the applicability of rock slope uncertainty.

2.1.1 Extension mechanism of joints in rock mass

Regional compressive stresses, folding, faulting, and uplift or cooling may have transformed rock masses in mountainous terrain over hundreds of millions of years. Extensional fractures, also known as joints, result from deformation and breakage (Burg, 2020). Cracks can be damaged mechanically in three forms (Figure 2.1). A tensile stress perpendicular to the fracture surface is applied to Mode I, an extension or dilatant joint, causing a total displacement in the direction of the tensile stress (Zhu, 2017). Internal shear crack and inverse plane crack are Modes II and III, respectively, where shear stresses parallel to the fracture surface generate crack displacement in general agreement with the fracture surface direction. Cracks in such shear joints have a higher probability of becoming faults.

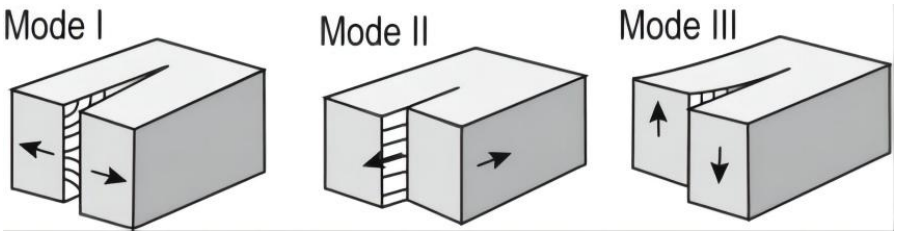

Figure 2.1 Three mechanical modes of cracks (Zhu, 2017).

Many researchers, both in Canada and abroad, have studied the damage mode of jointed rock and have yielded promising results. Lajtai (1974) investigated jointed rock's uniaxial compression and

brittle degradation. Smooth wing cracks with an expansion direction parallel to the direction of loading and maximal principal stress were found in a sample of a single joint, followed by secondary cracks expanding along the direction of pre-existing joints and perpendicular to the precast joint direction (Figure 2.2).

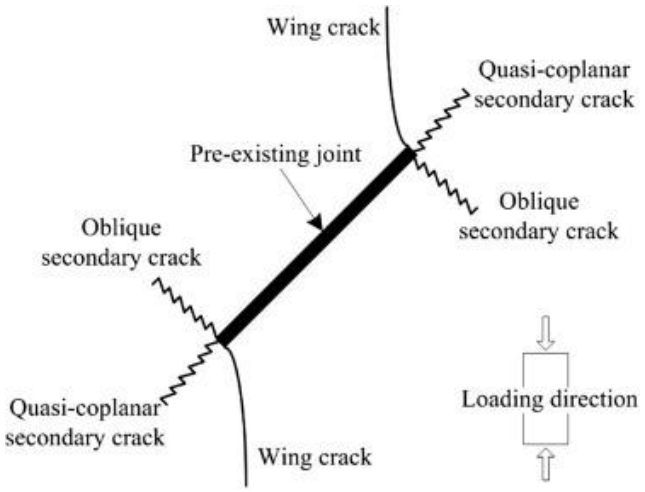

Figure 2.2 Cracking pattern during compression (Bobet & Einstein, 1998).

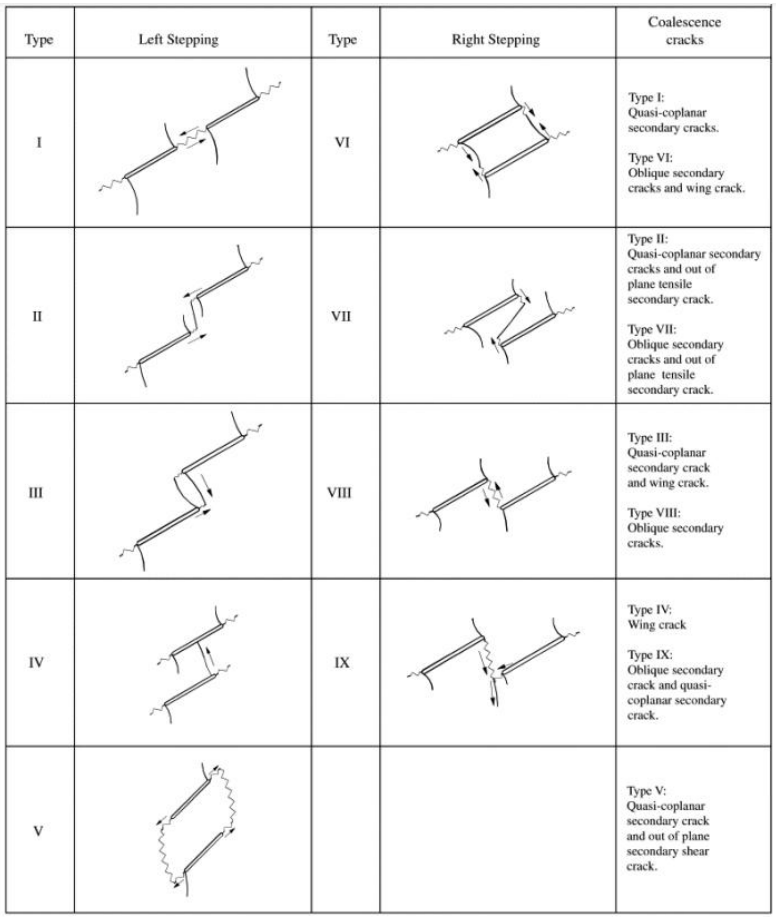

Figure 2.3 The penetration mechanism of the two joints (Reyes & Einstein, 1991).

Bobet and Einstein concluded that the geometric conditions of the joints and the confining pressure under uniaxial compression govern a rock sample with two joints (Bobet & Einstein, 1998). Reyes

and Einstein discovered (Figure 2.3) that if the two joints overlapped, the wing fractures would extend to become penetration; If the joints don't overlap, shear damage tends to occur (Reyes & Einstein, 1991). Tension, shear, and hybrid penetration are the three extension types for the joints. Under uniaxial compression conditions, the three joints create penetration mostly along two of the joints (Sagong & Bobet, 2002), following the path of least stress.

The dip angle of the joints (Li et al., 2000), the number of joints, geometric parameters, and lateral stresses (Lin et al., 2000) all have a substantial impact on the damage mechanism of multi-joint rock masses. Under the same stress conditions, Zhou (2014) found that multijointed rock shows similar damage patterns to two-jointed rock.

2.1.2 Development of jointed rocks in slopes

The intersection of the Mohr diagram with the rock strength failure envelope can be used to determine the kind of failure of the jointed rock. The rock suffers tensile failure when there is no dihedral angle between conjugate fractures; when the dihedral angle exceeds a particular magnitude, the rock suffers shear failure (Figure 2.4). When the stress circle intersects the failure envelope on the side of the tensile stress, hybrid shear failure occurs (extension and shear fracture coexist at the joint). In comparison to σ_3 in tension, the jointed rock is less prone to failure when both the major principal stress (σ_1) and the minor principal stress (σ_3) are in compression (Hammah et al., 2005).

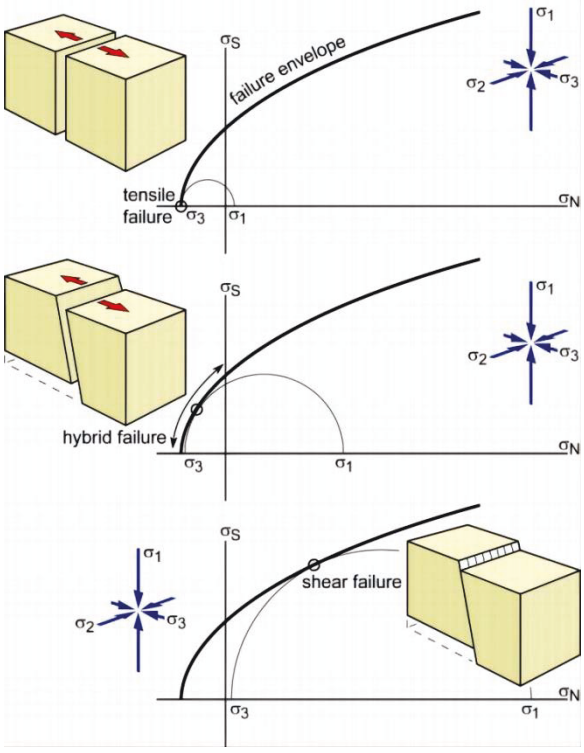

Figure 2.4 Failure modes of the joint (Burg, 2020).

In most cases, joints are randomly arranged into groups termed joint sets inside the actual rock mass. Each set of joints has a similar shape and orientation (Burg, 2020). Jointed rock slopes can exhibit a variety of failure patterns depending on the interaction of multiple joint sets (Zhu, 2017), mainly divided into sliding and toppling (Figure 2.5). Sliding is a type of slope instability dominated by

shear failure, and its slip surface morphology can be classified into four categories. Plane sliding [Figure 2.5 (a)] results in displacement along a single fracture surface with a greater dip angle than the rock's internal friction angle. Figure 2.5 (b) depicts circular sliding (the slip surface is virtually arc-shaped), which is most common in extensively fractured rocks, with tensional fracture expansion at the back edge of the landslide early on and fracture penetration at the slide bed later (Hoek & Bray, 1981). During the slip, the slope angle is constantly creeping. The stepped failure mode [Figure 2.5 (c)] is characterized by steep and moderately sloping structural surfaces, and it is frequently encountered on high slopes both in Canada and beyond (Zhu, 2017). On hard, blocky rock slopes, tensile cracking occurs on steeply dipping structural surfaces, while shear slip occurs on gently dipping structural surfaces in a zigzag compound pattern. The inclination of the combined intersection line of structural surfaces formed by two sets of discontinuous joints tends to the slope inclination, and the value of the dip angle is between the slope angle and the internal friction angle, resulting in wedge slides [Figure 2.5 (d)]. Toppling failure [Figure 2.5 (e)] is a collapse caused by rock gravity through moving surfaces. The slope's reversed structural face is misshapen to develop a discontinuous surface, and the rock gradually tilts outward before collapsing.

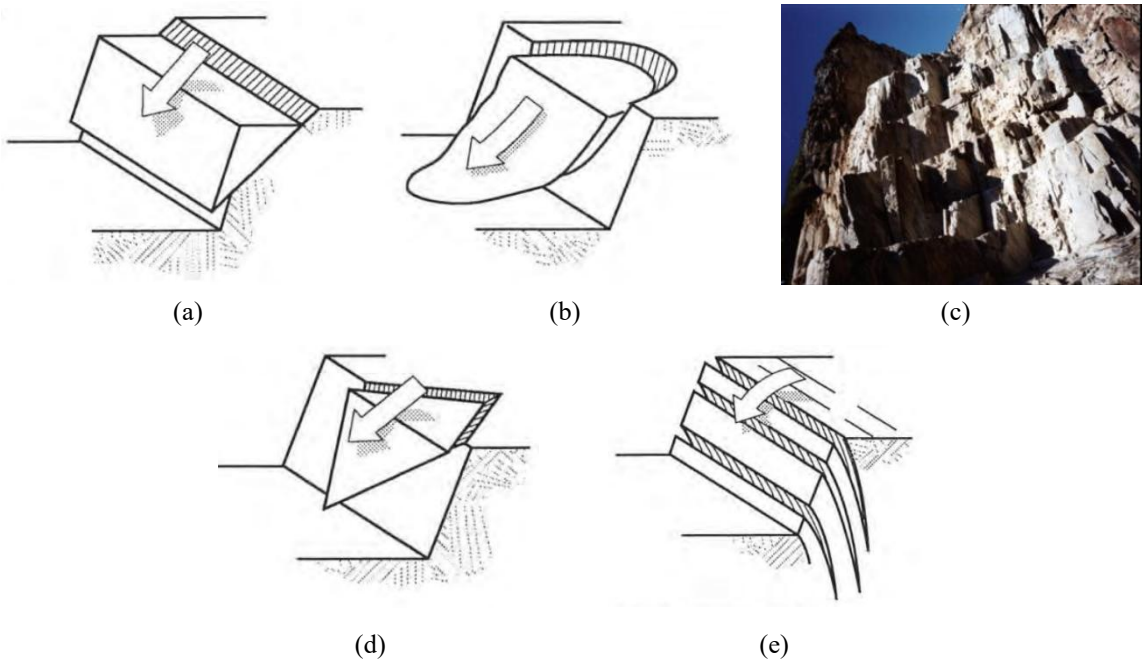

Figure 2.5 Types of jointed rock slope failures: (a) Plane failure; (b) Circular failure; (c) Stepped failure surface formed by the Randa rock avalanche; (d) Wedge failure; (e) Toppling failure. (Hoek & Bray, 1981; Zhu, 2017)

2.1.3 Application of jointed networks

The joint network has the ability to regulate the effect of each parameter's variability on slope stability. Each model constructs a joint network from one or more distinct joint sets. The slope failure can be determined using different joint networks to produce safety factor values.

There are six main joint networks that can be generated using various statistical or deterministic approaches (Rocscience, 2023). Figure 2.6 (a) depicts a standard Parallel Deterministic joint network model with fixed spacing, orientation, length, and persistence, with randomization in joint position.

Figure 2.6 (b) presents a Parallel Statistical joint network model in which a statistical distribution defines each set of joints' spacing, length, and persistence. The Cross Jointed model in Figure 2.6 (c) is generated by the intersection of two sets of parallel joints, where the spacing value of joint planes can follow the statistical distribution model. The Poisson point process is used to locate the joint centers of the Baecher joint network model (Baecher et al., 1977) in Figure 2.6 (d). The Veneziano joint model is identified based on the Poisson line process (Dershowitz, 1984), as shown in Figure 2.6 (e). Both have the ability to construct complicated joint network models with unpredictable joint lengths and orientations. The joints in the Veneziano model are in the same plane and have random persistence, whereas the joints in the Baecher model are independent segments that commonly terminate at intact rocks. The Voronoi joint network is refined by non-overlapping boundary segments of convex polygons (Dershowitz, 1984), with parameters defining the average lengths of the edges and the density of subdivided areas, as illustrated in Figure 2.6 (f).

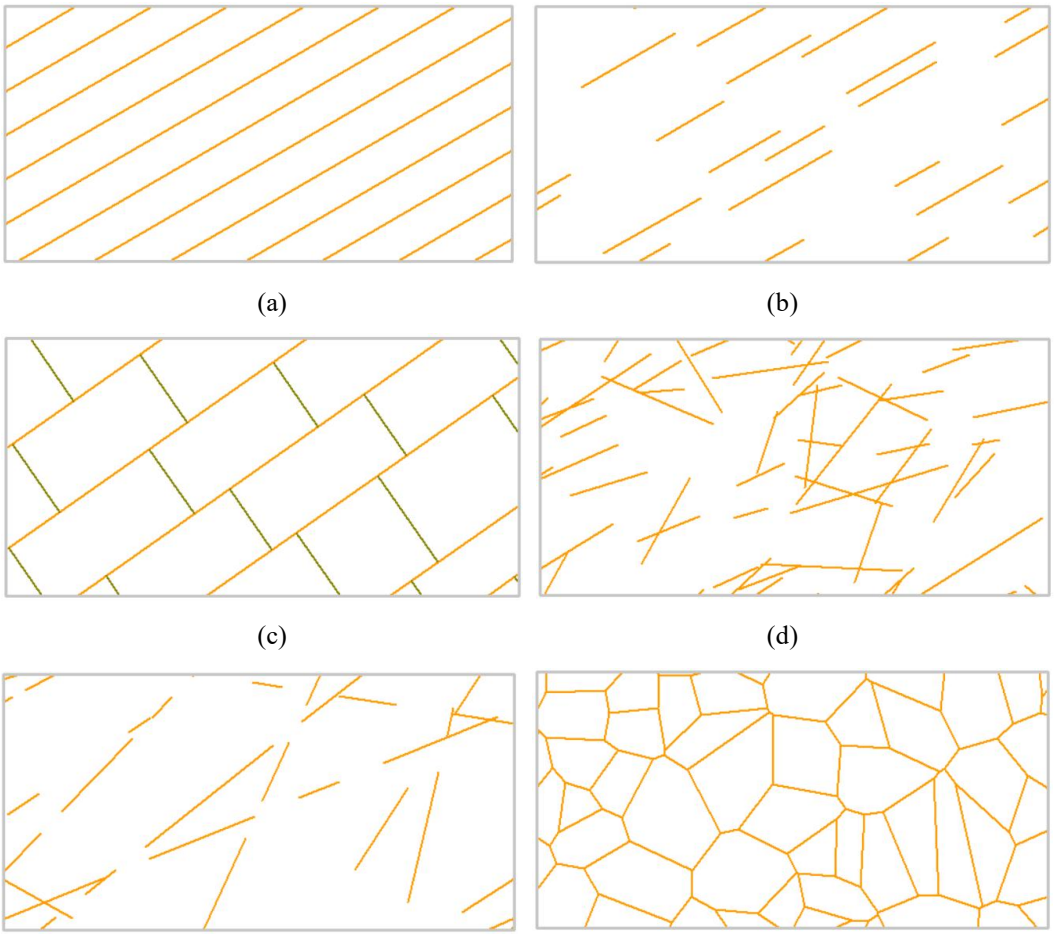

Figure 2.6 (a) An example of the Parallel Deterministic model with infinite joint length and 30° inclination;
(b) An example of the Parallel Statistical model with random joint spacing, length and persistence;
(c) An example of the Cross Jointed model with 35° bedding plane inclination;
(d) An example of the Baecher model with random joint length and orientation;
(e) An example of the Veneziano model with random joint length, orientation and persistence;
(f) An example of the Voronoi model with irregular polygons. (Rocscience, 2023)

Various forms of joint geometry modeling approaches are applied to simulate distinct joint networks

in the rock mass. In this study, only one set of Parallel Deterministic joints is employed in each model to directly observe the impact of each type of joint geometry on slope stability. In the case that joint ends are open, the ends of the joint boundary can be represented by two nodes that move relative to one another in the finite element mesh, whereas in the closed case the joint ends cannot slide or open.

2.2 Analysis of moving loads on the railway embankment

By analysing the railway track structure and the types of loads applied to the track and foundation during transportation, this part investigates the mechanism of load transfer through the track structure. The mechanism is a fantastic resource for track and subgrade design and rehabilitation (Li et al., 2015).

2.2.1 Railway track structure

The stability of the embankment slope is directly connected to the loading created by trains when rails are built on rock embankments. The track structure's layout is critical since it is responsible for transmitting wheel loads from the track superstructure to the substructure (Li et al., 2015). Ballasted and ballastless tracks are the two types of railway tracks (Figure 2.7). Sleepers are placed on crushed stone ballast, making ballasted track inexpensive and simple to lay. Its bigger pores allow for better track drainage (Esveld, 2001). The roadbed of a ballastless track does not require gravel. The rail sleepers are installed directly on the concrete slab, ensuring smooth train movement and extending the track's service life. However, due to its high construction cost and limited scope for improvement, ballastless track is not widely used in North America (Xu, 2019). Hence, ballasted track is the subject of this thesis.

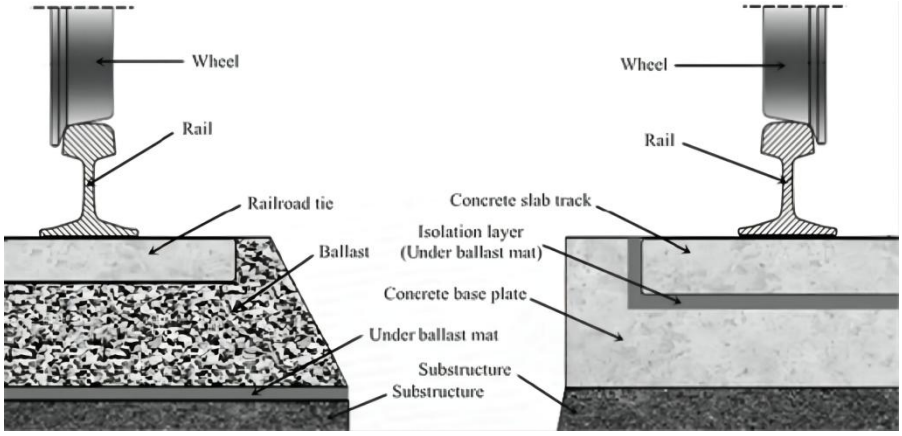

Figure 2.7 Longitudinal view of ballasted track and ballastless track (Sheng et al., 2020).

There are two sections to a ballasted track (Figure 2.8). Rails, sleepers, ballast, and subballast are all part of the superstructure. To sustain the trains, the rails and sleepers form a flat structure. The sleepers are in charge of conveying and dispersing the rails' wheel loads to the ballast and subballast, which is composed of loose rock aggregate; this is often crushed stone (30/60 mm gradation) according to Andrade's survey. The ballast bed absorbs some of the compressive loads and helps to keep the substructure in good shape (Andrade, 2008). The formation and base layers of the

subgrade provide suitable load-bearing strength and stability. The combined influence of the superstructure and substructure ensures train movements' reliability and longevity (Li et al., 2015).

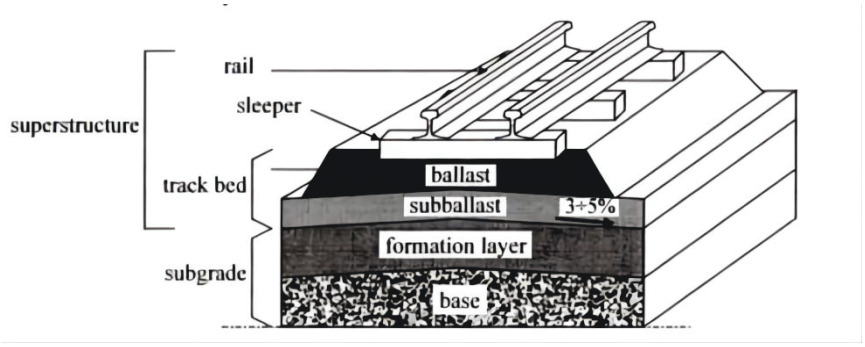

Figure 2.8 Components of a ballasted track (Profillidis, 2014).

2.2.2 Loading covering the railway track foundation

The type of wheel load that the track is subjected to, including static, cyclic, and dynamic loading, determines the state of load transfer from the wheels to the track foundation (Li et al., 2015). The moving loads created by the wheels can be transferred to the elements in the foundation below the track during train movement. Figure 2.9 depicts the three stress states corresponding to different elements under the same wheel load in the vertical and lateral directions. The normal stresses in both directions are classified as σ_1 and σ_3 depending on the magnitude of the values when the element is placed directly beneath the wheel load.

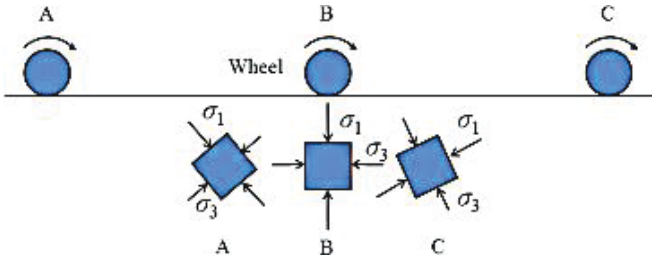

Figure 2.9 Stress state of the elements in track foundation (Guo et al., 2016).

a. There are two types of static loading on the railway foundation. The live load is the weight of the train, which is followed by the dead load, the weight of the track, and the roadbed combined. According to Li et al. (2015), the live load is the concentrated point load that is spread after the wheels and track make contact. Because the load is gradually diffused from the top to the bottom of the track structure, the tension created reduces as the depth of the track foundation increases. Conversely, as the depth of the foundation increases, the stresses caused by the dead load increase, whereas the stress generated in the ballast or even at the top of the foundation is minimal (Li et al., 2015).

b. The moving load causes a series of repetitive loads on the track, known as load pulses, throughout train operation.

   The substructure is swiftly assaulted with these repeating pulses. The geotechnical mass of the foundation responds to changes in the loading rate (Li et al., 2015).The fluctuation of the pulse rate, defined by the duration of the loading pulse (Equation 2.1), can be determined by the train's

operating speed and the depth considered.

$$t = \frac{L}{v} \tag{2.1}$$

where the influence length of an axle load or adjacent axle loads for a particular depth of ballast or subgrade over the train speed determines the duration of the loading pulse.

Haimson et al. (1972) concluded that cyclic loading causes deformation equivalent to that generated by static loading after the peak. The mechanical behaviour of the rock can be affected by the frequency and number of pulses as well as the duration of the cycles. With a stress threshold close to the yield stress, rock deformation can induce fatigue damage (Ge, 1987). Wang et al. (2008) proposed that cyclic loading often occurs during the yield deformation phase of rock masses.

c. Vehicle suspension has little or no action in the short term or responds for long periods of time, resulting in dynamic (wheel) loading. Wheel or rail deterioration or failure, such as unrounded wheels, tilted rail joints, misaligned welds, and so on, is able to cause vehicle suspension non-action (Indraratna et al., 2011). Long rail wavelengths may cause impact loads to be generated and transferred to the track substructure for an extended period of time. The value of static wheel loads differs from the loads delivered to the track during train operation (Li et al., 2015), and the impact load factor can be used to calculate their association.

2.2.3 Load transfer mechanism

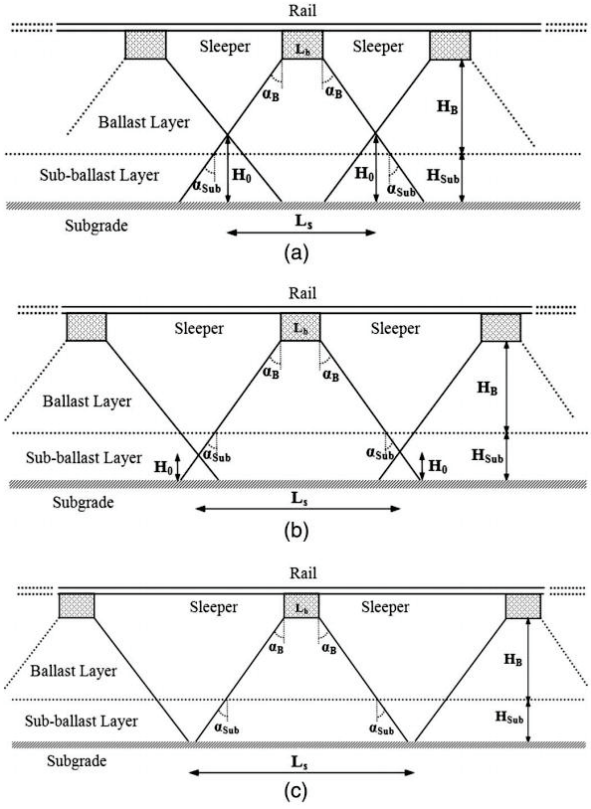

Figure 2.10 Stress transfer in the track foundation: (a) stress overlapping initiation from ballast layer; (b) stress overlapping initiation from subballast layer; (c)without stress overlap areas. (Mosayebi et al., 2020)

As the load reaches the substructure layer, high-frequency stress components dissipate quickly, whereas low-frequency static or dynamic wheel loads continue to spread and propagate to deeper structural layers with increasing depth (Li et al., 2015). Figure 2.10 depicts the profile of stress transmission in each layer of the track structure, with sleeper spacing and ballast and subballast depth determining whether stresses overlap and start to overlap from the ballast or subballast layer. Bourdeau and Harr (1989) postulated that the material's continuity and homogeneity change in each layer of the track structure and that the load transmission of a single layer generates random fluctuations in the horizontal direction due to particle interaction. As a result, the vertical stresses in the area below the sleeper will not be evenly distributed. Zhang et al. (2016) suggested a modified stress spread model in 2016 to adjust for this (Figure 2.11).

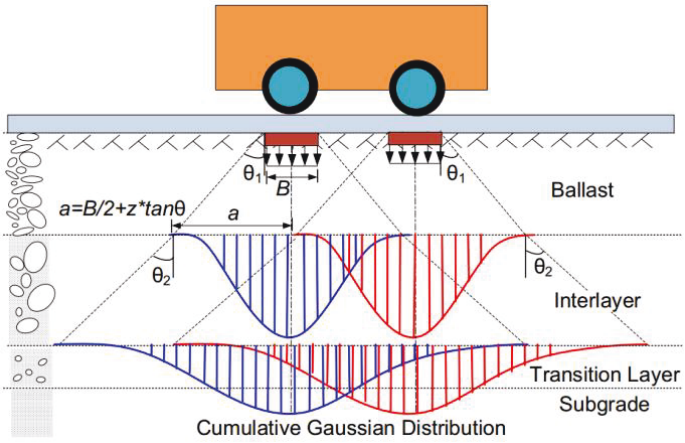

Figure 2.11 Modified spread model (Zhang et al., 2016).

The American Railway Engineering and Maintenance of Way Association (AREMA) recommends calculating the average pressure using a specific formula (Equation 2.2) in Chapter 30 of the 2012 manual to tackle the problem of ballast pressure at the bottom of the sleeper not being uniformly covered by the ballast.

$$P_{avg} = \frac{L_{axle}(1+\frac{IF}{100})(\frac{DF}{100})}{A} \quad (2.2)$$

where P_{avg} is the average bearing pressure at the sleeper-ballast connection boundary and L_{axle} denotes two axle loads for train operation, both in pounds-force (lbf). The maximum P_{avg} value for timber sleepers is 65 psi, while the value for concrete sleepers should not exceed 85 psi (AREMA, 2018). The impact factor (*IF*) represents the dynamic force effect caused by wheel-rail abnormalities. *DF* is the load distribution factor, and *A* indicates the bearing area of the ballast.

According to AREMA (2018), the distribution factor is linearly proportional to centre-to-centre sleeper spacing, as shown in Figure 2.12. When the degree of track modulus and sleeper type varies, the same sleeper spacing has distinct distribution factors.

In the 2018 operation manual, AREMA describes numerous methods for calculating bearing area (A). Part 10 of Chapter 16 mentions that newly constructed tracks can be used to determine average pressure, considering two thirds of the sleeper footprint as the effective bearing area. L_{eff} is one third the length of a sleeper (L; Figure 2.13). The entire footprint of the sleepers is considered the value of A for existing tracks, according to Chapter 30 (AREMA, 2018).

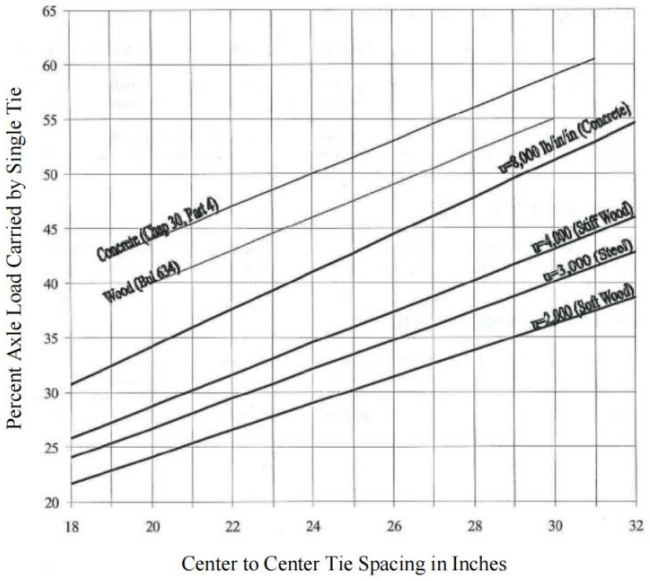

Figure 2.12 Estimated loads distribution (AREMA, 2018).

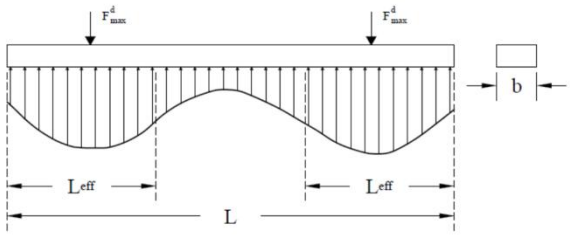

Figure 2.13 Assumed pressure distribution (Kerr, 2003; AREMA, 2010).

2.3 Key parameters of the model

The major goal of this section is to define the parameters and a believable range of physical models that can be developed for jointed rock track foundations when parameters for the freight train, rail construction, foundation, and drainage system are all accessible. As a result, the dimensions of the freight train and the embankment, the values of the moving loads, slope inclination ratios, joint spacing as well as orientation, and jointed rock properties should be taken into account.

2.3.1 Parameters related to locomotive and freight cars

Wagons are hauled by one or more locomotives with the ability to move both people and cargo along the railway. Figure 2.14 depicts the two most frequent freight car capacities currently in use in North America. Figure 2.14 (a) represents the maximum gross rail load (GRL) of a four-axle railcar carrying 100 tons of freight, whereas Figure 2.14 (b) indicates the maximum GRL of a four-axle railcar carrying 110 tons of cargo, with the latter being utilized more frequently. On freight trains, the 840 mm and 920 mm diameter wheels are commonly utilized, with the 920 mm diameter wheels being more widespread today (Technical Specialist Rolling Stock Performance Standards, 2013).

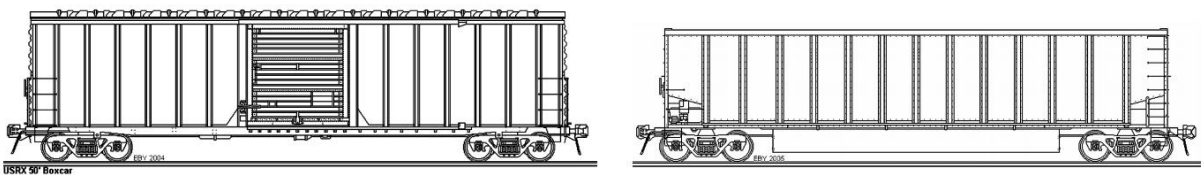

(a) (b)

Figure 2.14 (a) Nominal capacity of 100 tons; (b) Nominal capacity of 110 tons (AREMA, 2012).

Axle load and operating speed are two critical factors in freight train design. The typical number of axles for different rolling stocks, as well as the corresponding static axle load magnitudes under no-load and full-load conditions, are shown in Table 2.1. The reasonable operating speed of freight trains is depicted in Table 2.2, with the lowest speed on branch lines and the highest speed on main lines.

Table 2.1 Static axle loads of different rolling stocks (Esveld, 2001).

	Number of axles	Empty load per axle (kN)	Fully loaded weight per axle (kN)
Trams	4	50	70
Light-rail	4	80	100
Passenger coach	4	100	120
Passenger motor coach	4	150	170
Locomotives	4 or 6	215	N/A
Freight wagon	2	120	225
Heavy haul (USA & Australia)	2	120	250–350

Table 2.2 Operating speed ranges for different railway lines (Esveld, 2001).

	Freight trains (km/h)	Passenger trains (km/h)
Branch lines	30–40	N/A
Secondary lines	60–80	80–120
Main lines	100–120	160–200
High speed lines	N/A	250–300

The freight train in this study is a four-axle per car freight train with a per-axle weight of 36,000 lbs (160 kN), and the maximum speed for operation on the main line is set at 120 km/h.

2.3.2 Parameters for railway track structure

The parametric characteristics of the superstructure and substructure of the railway track required for this analysis are described below.

(a) Superstructure

The track gauge (TRG) is the rail spacing measured 14 mm below the rolling surface (Profillidis, 2014). Four sizes of track gauges are commonly used in North America and Europe, with the values

given in Figure 2.15. (Starns, 2012). In around 10% of the world (Saputro et al., 2020), metric gauge (1,067 mm) is utilized, primarily on secondary lines. Due to axle pressure limits, the metric gauge is technically designed for lower maximum speeds and smaller locomotive and wagon sizes. With test speeds of up to 400 km/h in China and axle pressures of 20 to 30 tons, the standard gauge (1,435 mm) is widely used in China, North America, and some European countries today, accounting for more than 60% of global use (Saputro et al., 2020). To prevent standard gauge trains from using tracks that are not suitable for the gauge type, Russia, Finland, and India employ broad gauges (1,524 mm and 1,676 mm).

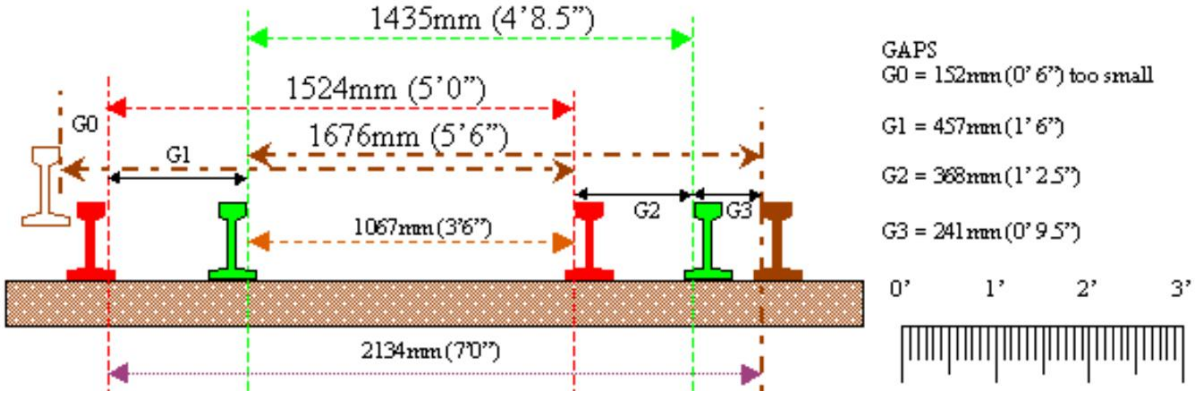

Figure 2.15 Comparison of TRGs (Starns, 2012).

Sleepers (cross ties) are put beneath the rail to help distribute the strain on the ballast. Sleepers have traditionally been made of wood (both hardwood and softwood) and have been shown to be effective in both heavy and high-speed track operations (RTA, 2016). They are still used in several Western countries. Wooden sleepers are used with any track section and are ideal for saline and coastal environments due to their low cost, light weight, and ease of transport and manufacture. However, since wood is susceptible to insect infestation, fire attack, and humidity and has poor creep resistance, wooden sleepers have a short service life.

As wood was scarce after World War II, concrete rail sleepers became increasingly popular in Europe and Asia (Esveld, 2001). Although concrete sleepers are heavy and cannot be used for bridges or crossings, they provide higher lateral stability and are less prone to corrosion, with a long service life that is cost-effective in the long run (Laryea et al., 2014). Steel sleepers, which are lightweight, recyclable, and have a similarly long life to concrete sleepers, are used on a small number of tracks, such as secondary lines in the United Kingdom. Steel sleepers are expensive and chemically susceptible, making them unsuitable for saline areas (Profillidis, 2014). If a derailment happens, the damaged steel cannot be reused.

Strong, durable tropical timber is becoming a prominent material for railroad construction in North America, with wood accounting for 91.5% of the railroad sleeper market share in 2008 (Railway Track & Structures, 2008). The geometric dimensions and mechanical characteristics of several timber sleepers, as well as typical sleeper material properties in North America, are shown in Tables 2.3 and 2.4. As wood outperforms concrete in terms of tensile and compressive strength, timber sleepers are a preferable choice for this investigation (Table 2.4).

Table 2.3 Material and strength properties of several timber sleepers in North America (RTA, 2016).

Material & Strength Properties			Oak	North Mixed Hardwo-ods	South Mixed Hardwo-ods	South -ern Pine	West -ern Soft -woods	Eastern Soft -woods	Douglas-Fir
Dimen -sions	Based on	Nominal	Southern Red Oak	White Birch	Silver Maple	Short -leaf Pine	Pon -derosa Pine	Eastern Hemlock	Coastal Douglas-Fir
	Length (TLE) [ft (mm)]	8.5 (2,591)	8.5 (2,591)	8.5 (2,591)	8.5 (2,591)	8.5 (2,591)	8.5 (2,591)	8.5 (2,591)	8.5 (2,591)
	Width (TWD) [in (mm)]	9 (229)	9 (229)	9 (229)	9 (229)	9 (229)	9 (229)	9 (229)	9 (229)
	Thickness (TTH) [in (mm)]	7 (178)	7 (178)	7 (178)	7 (178)	7 (178)	7 (178)	7 (178)	7 (178)
	Cross-sectional area [In^2 (mm^2)]	63 (40,645)	63 (40,645)	63 (40,645)	63 (40,645)	63 (40,645)	63 (40,645)	63 (40,645)	63 (40,645)
	Spacing [in (mm)]	19.5 (495)	19.5 (495)	19.5 (495)	19.5 (495)	19.5 (495)	19.5 (495)	19.5 (495)	19.5 (495)
Weight [lbs (kg)]			218 (98,883)	205 (92,986)	179 (81,193)	192 (87,090)	156 (70,760)	156 (70,760)	182 (82,554)
Moment of Inertia [In^4 (mm^4)]			257 (1.070 ×10e8)	257 (1.070 ×10e8)	257 (1.070 ×10e8)	257 (1.070 ×10e8)	257 (1.070 ×10e8)	257 (1.070 ×10e8)	257 (1.070 ×10e8)
Section Modulus [In^3 (mm^3)]			73.5 (1.204 ×10e6)	73.5 (1.204 ×10e6)	73.5 (1.204 ×10e6)	73.5 (1.204 ×10e6)	73.5 (1.204 ×10e6)	73.5 (1.204 ×10e6)	73.5 (1.204 ×10e6)

Table 2.4 Mechanical characteristics of different railway sleepers (Profillidis, 2014).

Material	Modulus of elasticity (MPa)	Poisson's ratio	Tensile strength (MPa)	Compressive strength (MPa)
Reinforced-concrete sleeper	2.94×10e4	0.25	2.94	29.42
Prestressed-concrete sleeper	4.90×10e4	0.25	5.88	8.83
Tropical timber sleeper	2.45×10e4	0.25	9.81	98.07
Rail (steel)	2.06×10e5	0.30	686.47	588.40

In this study, 1,435 mm track gauge and timber sleepers with 2,591 mm length, 229 mm width, and 495 mm center-to-center spacing are considered for the superstructure design of Canadian railroads.

(b) Substructure

The typical track substructure parameters are shown in Figure 2.16. The ballast section depth (BDD) of a single tangent track is measured from below the line rail. The distance between the end of the sleeper and the ballast side slope (BSS) refers to the shoulder width of the ballast section (BSW). The confining pressure to transmit vertical loads in the ballast layer is typically provided by a BSS value of 2H:1V (value ratio between the horizontal and vertical axes). On standard gauge main lines, AREMA (2010) recommends that both BDD and BSW be no less than 12 in (304.8 mm) to provide adequate longitudinal and transverse strength support for the track. To reduce weather disturbance to the roadbed, a compacted depth (SBD) of at least 6 in (152.4 mm) is necessary for the subballast section (Indraratna et al., 2011), with a common compacted SBD value of 12 in (304.8 mm) being used in the main track calculations. To meet the top of the roadbed with appropriate drainage, the ratio of the subballast side slope (SBS) should be in the range of 24H:1V to 40H:1V (AREMA, 2012). The SBS inclination must be raised properly when the subballast material has low permeability.

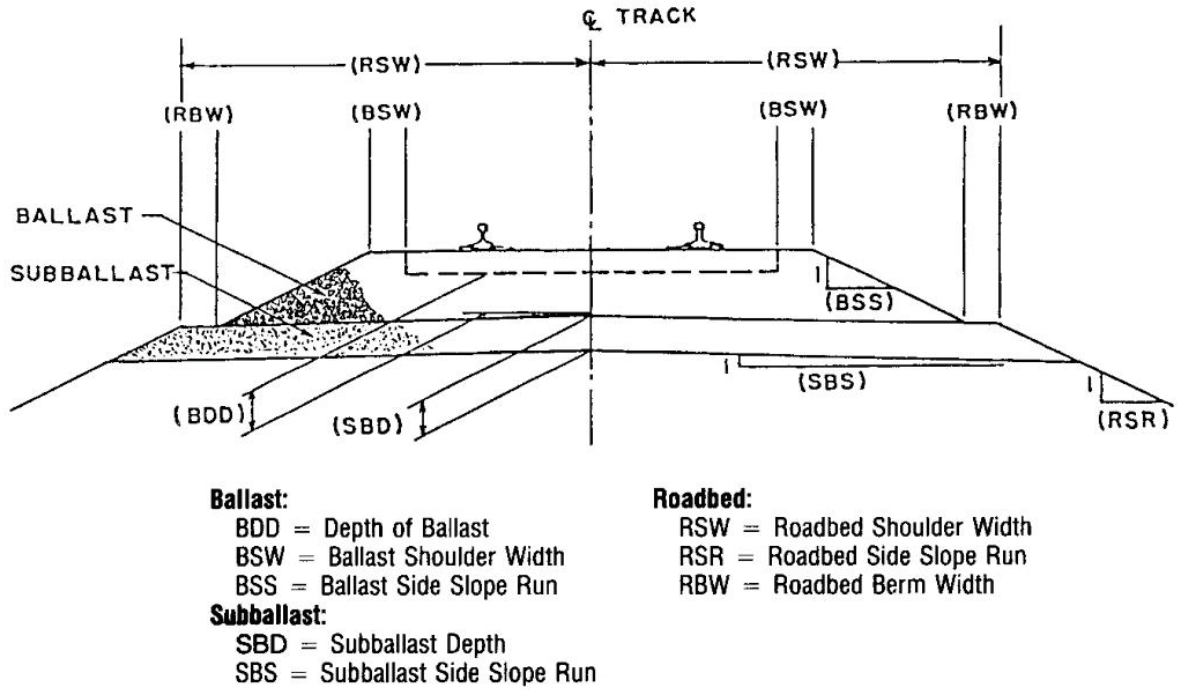

Figure 2.16 Single track substructure (AREMA, 2010).

Table 2.5 Mechanical characteristics of substructure materials (Profillidis, 2014; Li et al., 2015; Allan, 2012)

Material	Elasticity modulus (MPa)	Poisson's ratio	Cohesion c (kPa)	Friction angle ϕ (°)
Ballast	127.49	0.2	96.25	44
Subballast	196.13	0.3	95	40
Rock subgrade	2,942	0.2	1,471	20

The subgrade (roadbed) is a natural soil or rock fill layer that is over 2,000 mm thick (Egeli & Uşun, 2012). The mechanical properties of materials widely used for track structures with rock as the

roadbed are shown in Table 2.5. Table 2.6 provides typical Young's modulus and Poisson's ratio ranges for several rocks.

Table 2.6 Range for Young's modulus and Poisson ratio for different types of rock (Lake et al., 2006).

Lithology	Young's modulus (GPa)	Poisson's ratio
Soft sandstone	0.7–6.9	0.2–0.35
Medium sandstone	13.8–34.5	0.15–0.25
Hard sandstone	41.4–68.9	0.1–0.15
Limestone	55.1–82.7	0.3–0.35
Coal	0.7–6.9	0.35–0.45
Shale	6.9–68.9	0.28–0.43

The AREMA manual specifies (AREMA, 2012) the steepest slope of 2H:1V for filling soft rock inside slopes up to 30 ft. If hard rock is used, the slope can be as steep as 1.5H:1V. The minimum slope ratio for hard rock fill up to 50 ft in depth is 2H:1V. According to CN (2019), the side slope of embankments must be at least 2H:1V. As a result, the recommended value for the steepest slope typical of rock slopes in railway substructures is 2H:1V. In this study, the ballast slope is set at 2H:1V, and the ratio of 2H:1V is used in the roadbed side slope.

2.3.3 Parameters for ditch

The cut section of a rail line carved out of a rock slope comprises the back and front slopes, the embankment that ensures the railroad's safety during operation, the jointed rock cut slope, and a reliable drainage system. The segment of the railway embankment in zone A is available in Figure 2.17. The drainage ditches (zone B) and catchment ditches (zone C) add additional width between the embankment and the rock slope to convey potential surface runoff and seepage from the back slope as well as to catch snow or rock debris falling from the cut surface to prevent them from bouncing back into the track area (AREMA, 2010).

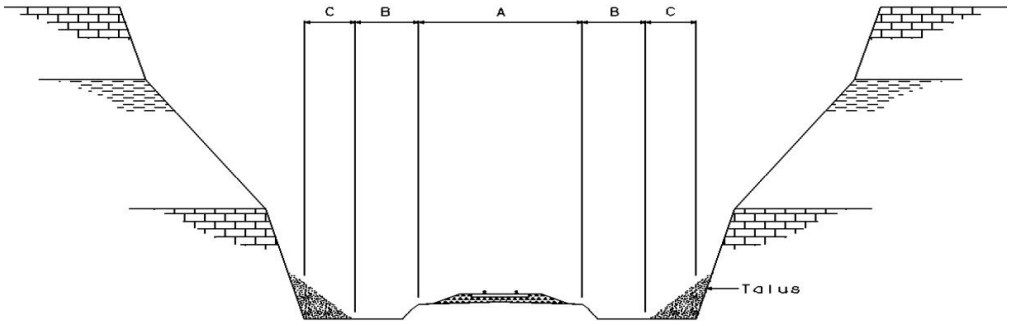

Figure 2.17 The rock cut base (AREMA, 2010).

For most railway ditch sections, trapezoidal designs are commonly chosen since the ditch must provide enough working width for the ditch cleaning machines (AREMA, 2010). To consider the drainage conditions and the capacity of the rock fragments being evaluated in the cut, it is critical to consider the ditch's width, depth, and slope. The important figure that will provide freeboard and

prevent rainfall infiltration into the subballast section is 2 ft (609.6 mm) below the roadbed's shoulder, which is the minimum depth that is advised. The minimum recommended trapezoidal ditch bottom width is 3 ft (914.4 mm), and the typical slope on both sides is 2H:1V (CN, 2019). The placement of the ditch guarantees the stability of the surrounding excavation and fill.

2.3.4 Rock slope angle

Depending on its level of integrity, weathering, and fracture, the rock within the same cut section should be chosen for varied slope angles. The slope is primarily governed by bedding planes— joints that are typically perpendicular to the bedding, fracture patterns, and faulting— all of which impact the rock slope's stability. The design slope angles of typical rocks are covered in Table 2.7 for four different scenarios.

Table 2.7 Factors in rock slope design (AREMA, 2012).

Rock condition	Slope design
Hard rock with random joints	Providing there are no adverse bedding planes or joint systems, ground water pressures are low and blasting is presplit, slopes of 70° are stable.
Layered rock	An accurate joint survey is important. If rock dips with the slope, and dip angle is greater than angle of friction, critical slope is at angle of dip. If bedding is horizontal, stability is as for massive rock. If bedding dips into slope, critical slope is between 70° and 90°; local rock falls may be frequent.
Fractured or weathered rocks	Stability can be analyzed using shear strength parameters derived from field observations. Angle of friction for angular crushed rock varies between 45°–50°.
Clay-shale rocks	Specialist advice is required as unloaded shale tends to decrease in strength with time.

2.3.5 Properties of jointed rock

The main geological parameters determining the stability of jointed rock slopes are joint orientation, spacing, length, and persistence; joint infill is also significant in slope design (Wyllie, 1999). All aspects of these discontinuities must be considered in the design and evaluation of slope stability.

2.3.5.1 Joint orientation

Identifying the orientation of the joints is the first step in assessing the creation of a potentially unstable surface on a slope. A simplified application can be used to aggregate the data once the orientation information has been received from sources such as surface and subterranean mapping, diamond drill core, and so forth (Hoek & Bray, 1981). Figure 2.18 (a) proposes that the terms *dip* (angle ψ) and *dip direction* (angle α) be used appropriately to denote joint orientation.

a. *Dip* is the maximum inclination of a discontinuity to the horizontal, ranging from 0° to 90° (both positive and negative on the x-axis).

b. *Dip direction (dip azimuth)* is the maximum dip of the dip line in the horizontal plane, measured clockwise from north, which ranges from 0° to 360°.

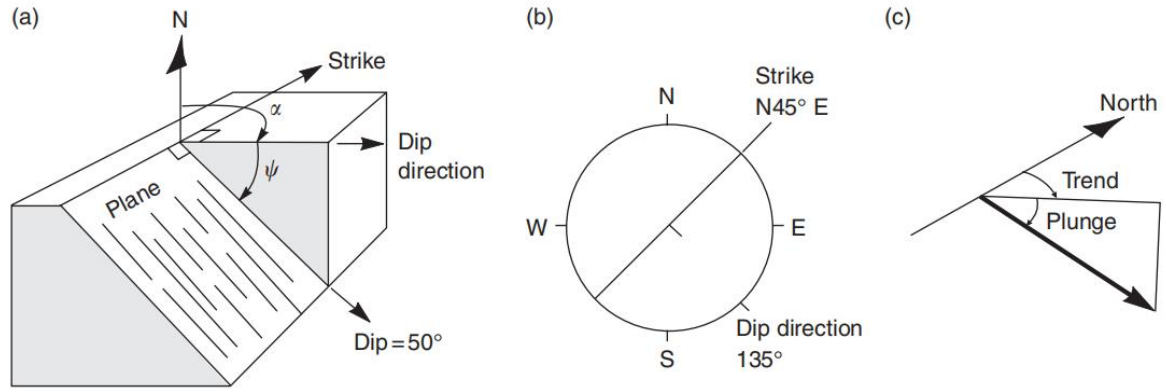

Figure 2.18 Definition of joint orientation: (a) Planar features (dip and dip direction); (b) Plan view of plane; (c) Linear features (plunge and trend) (Hoek & Bray, 1981).

The "Strike" trajectory identifies the point at which the inclined joint plane and the horizontal reference plane intersect and form a right angle with the dip direction. According to Figure 2.18 (b), the plane's strike is at N45E, while its dip is at 50SE, making its plane orientation 50/135 (dip/dip direction).

Planes can be depicted as lines, and lines are depicted as points in stereographic projections since they do not take one dimension into account (Norrish & Wyllie, 1996). In Figure 2.18 (c), the phrases "Plunge" and "Trend" indicate the line's direction. A positive plunge is one that is below the horizontal, which refers to the line's dip. Trend corresponds to the plane's dip direction, which is the direction of the line's horizontal projection measured clockwise from the north. The reference sphere's axis is fixed in the northern direction, and the equatorial plane is horizontal to form the conceptual core of the stereographic projection. Figure 2.19 depicts the line and plane representing the joint in the reference sphere.

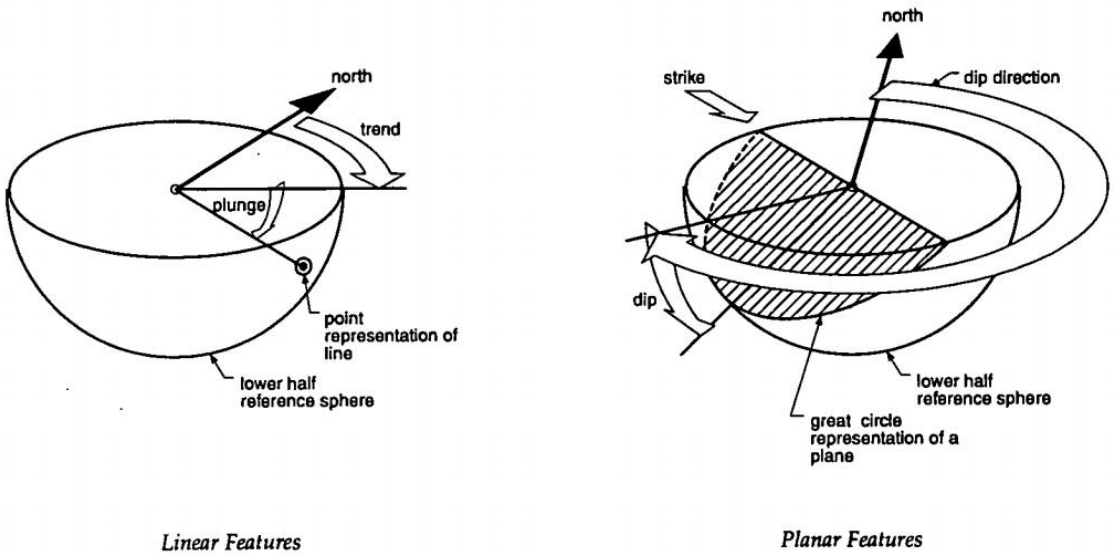

Figure 2.19 Representation on reference sphere (Norrish & Wyllie, 1996).

The dispersion in the poles depicted on the stereo network is caused by the joint orientation's natural variation, and these scatters also expose the slope to the possibility of instability. The mean and

standard deviation of the dip ψ_R and dip direction α_R are calculated to estimate these risks (Equation 2.3).

$$\left.\begin{array}{ll} \psi_R = \cos^{-1}(n_R) & \\ \alpha_R = +\cos^{-1}(I_R/\sin\psi_R) & \text{for } m_R \geq 0 \\ \alpha_R = -\cos^{-1}(I_R/\sin\psi_R) & \text{for } m_R \leq 0 \end{array}\right\} \quad (2.3)$$

where I_R , m_R , and n_R are the direction cosines of the mean orientation of the joint set for a number of poles (Goodman, 1991). Equation 2.4 can be used to determine the mean orientation when the scatter's dispersion is roughly uniform.

$$\theta = cos^{-1}[1 + (1/C_d)\, ln\,(1 - P_0)] \quad (2.4)$$

where P_0 is the probability that the pole angle is not greater than the mean orientation. The dispersion coefficient, C_d , has a value that is inversely proportional to the joint orientation's magnitude of dispersion. According to Equation 2.5, the standard deviation in both directions can be approximated when the scattering of dip is less than that of the dip direction (Morriss, 1984).

$$SD = tan^{-1}\{0.34[tan\,(P_{93}) - tan\,(P_7)]\} \quad (2.5)$$

where P_7 and P_{93} are the angles corresponding to the 7% and 93% levels, respectively.

The slope rock and soil structures program RS2 performs two-dimensional finite element analysis (Rocscience, 2023). The representation and analysis of directional data in three dimensions are made possible by RS2, which employs stereographic projections in two dimensions. Although the actual analysis of the plane strain in RS2 is two-dimensional, the two-dimensional trajectory of the joint planes on the trace plane may be traced using three-dimensional data. This study directly uses the two-dimensional inclination *dip* (angle ψ) in the model analysis to simplify the computation of the two-dimensional mapping of joint spacing, length, and persistence. In a railway embankment rock foundation, the dip ranges from 0° to 180° with a positive horizontal axis.

2.3.5.2 Joint length and persistence

Joint length is the length of each joint in the network. The length of the potential failure surface and the size of the block slipping from the face are determined by the joint length, along with the joint persistence and spacing. The continuity length or range of discontinuity regions is referred to as persistence. In terms of persistence, the joint's length can be represented. The category range for it is typically 1 to 20 m, while it can be outside this range with either very high or very low persistence (Wyllie & Mah, 2004).

Even if the rock is small, a piece of undamaged rock between discontinuities of joints in a low-persistence jointed rock mass can contribute to slope stability. The shear pressures exerted on the slope can be resisted and considerably outweighed by the rock's strength.

Persistence information is challenging to measure. To accurately quantify persistence information, particular sections of bedrock must be exposed using drill cores. Pahl (1981) created a method to estimate the approximate average length of visible trace lines in a specific area (Figure 2.20). The mapping length study focused on the set of joints that has the greatest impact on rock stability, which has a dip angle of ψ. In circumstances when the random length of the joint does not equal the

mapping surface dimensions, the approximate average length ($\bar{l}$) can be determined using Equation 2.6 (Pahl, 1981).

$$\bar{l} = H' \frac{(1+m)}{(1-m)} \tag{2.6}$$

where

$$H' = \frac{L_1 L_2}{L_1 \cos\psi + L_2 \sin\psi} \tag{2.7}$$

and

$$m = \frac{N_t - N_c}{N' + 1} \tag{2.8}$$

The length and height of the mapping area are represented by L_1 and L_2. The total number of discontinuities (N'), the number of joints contained within (N_c), and the transect (N_t) of the mapping region are used to estimate the average length of joints. The assumed form of the statistical distribution of lengths has no bearing on the calculation of the mapping surface exposure traces (Pahl, 1981; Priest & Hudson, 1981; Kulatilake & Wu, 1984).

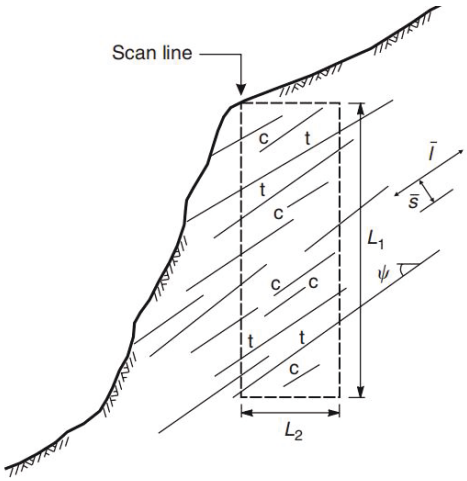

Figure 2.20 Measurement of average spacing and persistence of a set of joints in an outcrop (Pahl, 1981).

In RS2 models, *persistence* is defined as the ratio of a joint length to the whole length that includes the intact material length between adjacent joints, and this joint length is represented as the ratio of the joint length to the total length along the joint plane (L_1/L_2, shown in Figure 2.21). The persistence in the model has a fixed value between 0 and 1. The joint length and total length are equal with a persistence of 1, indicating an infinite joint length.

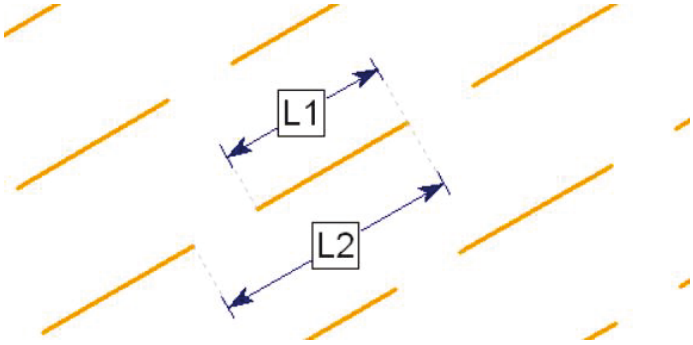

Figure 2.21 Representation of persistence in RS2 (Rocscience, 2023).

2.3.5.3 Joint spacing

The spacing of joints affects rock strength and defines the dimension of the slips. Continuous fractures are more likely to form in dense and compact areas of joints, reducing rock strength. When the spacing is greater than 2 m or less than 6 mm, it is considered to be in the extreme range (Wyllie & Mah, 2004).

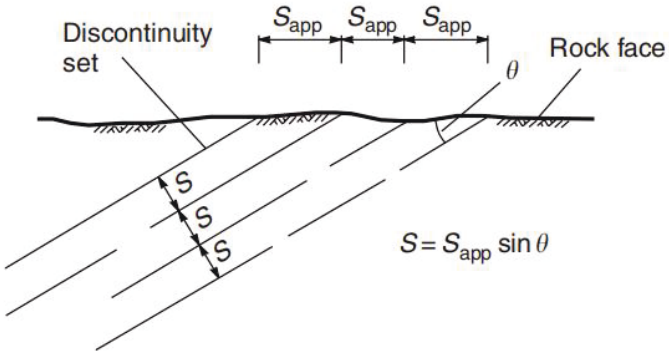

Figure 2.22 Apparent and true spacing for a set of joints (Pahl, 1981).

The relative orientation θ of the joints in relation to the rock face in the set of joints shown in Figure 2.22 defines the size of the discrepancy between the surface-mapped spacing S_{app} and the true spacing S. Despite appearances, the spacing is actually closer together. Equation 2.9 can be used to determine their relationship.

$$S = S_{app} \sin\theta \tag{2.9}$$

The number of discontinuities adjusted in the joints N can also be represented by measuring the number of discontinuities at the joints N_{app} and the orientation θ.

$$N = \frac{N_{app}}{\sin\theta} \tag{2.10}$$

Joint spacing is irregularly distributed and varied in rock outcrops. When the scanline is not at right angles with respect to the joints in Figure 2.20, the average spacing ($\bar{S}$) can be calculated using Equation 2.11, which is based on the relationship between the horizontal scan line of length (L_s) and the number of joints (N'') intersecting the scanline.

$$\bar{S} = \frac{L_s \sin\psi}{N''} \tag{2.11}$$

Setting an ideal scan line at a right angle to each group of joints allows for the measurement of the average spacing when more than one group of joints in the scan zone impacts rock stability (Hudson & Priest, 1979). Equations 2.6 to 2.11 must subsequently be repeated to calculate the corresponding average joint spacing and length separately.

Different joint persistence and spacing can lead to slope stability variations. An example of a potential downward sliding surface is formed by joint J1 in Figure 2.23 (a), which is widely spread and has a higher persistence than the slope height. The slides that are generated in Figure 2.23 (b) are tight and packed, and the slope as a whole is not damaged since both sets of joints have lower persistence and smaller separation. In contrast to Figure 2.23 (a), Figure 2.23 (c) indicates that toppling slabs are prone to forming in the direction of J2, where the joint J2 has higher persistence

than the slope height. Therefore, the joints' persistence and spacing measurements can estimate the size of the rock masses the surface has generated as a guide when building stabilization strategies (Kikuchi et al., 1987; Dershowitz & Einstein, 1988).

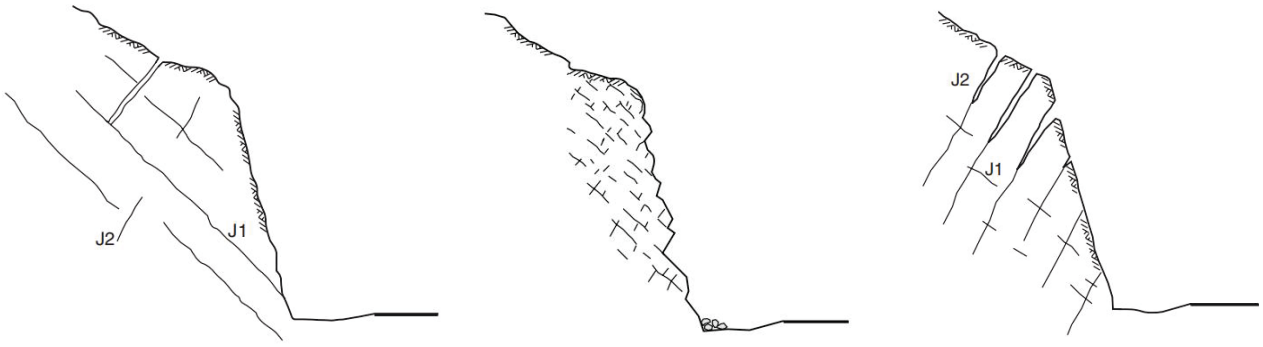

(a) (b) (c)

Figure 2.23 Effects of joint properties on slope stability in three joint networks (Hoek & Bray, 1981).

2.3.5.4 Joint infill

Clay, sand, and other fine fillings produced by weathering are frequently used to fill the joints in rocks (Shrivastava & Rao, 2014). These infill materials turn into the jointed rock mass's weakest planes (Indraratna et al., 2008), diminishing contact between the joint walls. As a result, the rock is more inclined to slide or shear, and the permeability and shear strength of the joint can be affected.

The cohesion between joints improves dramatically when a secondary mineral, like calcite or quartz, is used as filler. However, this cohesiveness will be completely destroyed if these fillings are blasted.

The triaxial apparatus has proven that joint infill thickness affects rock behaviour (Sinha & Singh, 2000). The ratio (b/a_h) of infill thickness (b) to asperity height (a_h) was examined by Phien-Wej et al. (1990). When a_h was adjusted at 5 mm, t was increased to 0, 5, 7, and 10 mm for b/a_h ratios of 0, 1, 1.4, and 2.

According to Shrivastava and Rao (2014), under conditions of constant normal load (CNL) and constant normal stiffness (CNS), the shear strength of the jointed rock mass drops as the b/a_h ratio increases. Based on experimental findings, Equation 2.12 was employed as an empirical equation to calculate the peak shear strength of infilled joints (Phien-Wej et al., 1990).

$$\frac{\tau_p}{\sigma_n} = \frac{\tau_o}{\sigma_n} - \frac{k_1}{\sigma_n}\left(\frac{b}{a_h}\right)e^{k_2\left(\frac{b}{a_h}\right)} \tag{2.12}$$

where τ_p is peak shear strength of the infilled joint, with τ_o for peak shear strength of the clean joint, σ_n represents normal stress under the CNL condition, and k_1 and k_2 are constants related to surface roughness and applied normal stress.

The shear strength of the joints typically decreases with increasing infill thickness. When the infill reaches the critical thickness, the rock wall of the joints is free of friction, and the infill materials determine the rock shear strength.

2.3.6 Properties of foundation rock

The engineering properties of the rock are directly connected to its compressive strength. The compressive strength of different types of rock can be measured by simple field tests, as indicated in Table 2.8 (Brown, 1981). Point load tests are used to estimate core or lump samples.

Table 2.8 Classification of rock strengths (Brown, 1981).

Grade	Description	Field identification	Range of uniaxial compressive strength *UCS* (MPa)
R6	Extremely strong rock	Specimen can only be chipped with geological hammer.	>250
R5	Very strong rock	Specimen requires many blows of geological hammer to fracture it.	100–250
R4	Strong rock	Specimen requires more than one blow of geological hammer to fracture it.	50–100
R3	Medium strong rock	Cannot be scraped or peeled with a pocket knife, specimen can be fractured with single firm blow of geological hammer.	25–50
R2	Weak rock	Can be peeled by a pocket knife with difficulty, shallow indentations made by firm blow with point of geological hammer.	5–25
R1	Very weak rock	Crumbles under firm blows with point of geological hammer and can be peeled by a pocket knife.	1–5
R0	Extremely weak rock	Indented by thumbnail.	0.25–1

To combine geological field data with failure criteria for very weak rocks, Hoek developed the Geological Strength Index (GSI) in 1994 (Hoek, 2007). The GSI values are generated from the level of rock mass fragmentation and the fracture surface conditions, which may estimate the decline in rock mass strength under various geological situations. A jointed rock's strength is influenced by both the characteristics of the intact rock and the state of the jointed surface under various stress conditions. Figure 2.24 depicts the range of GSI values for various grades of jointed rocks.

The intact rock constant m_i stands for the curve-fitting parameter of the Hoek-Brown failure envelope, which is one of the crucial parameters for determining the damage of brittle rock materials (Hoek & Marinos, 2000). It was concluded from many triaxial tests (Hoek & Brown 1980) that the range of m values is significantly influenced by the value of the confining pressure (σ_3). Davarpanah et al. (2021) summarized the statistical analyses measuring m_i values for various rock types (Table 2.9). Hoek (2007) reported an updated value for the collection of m_i and the potential range of variation of the corresponding data as shown in Figure 2.25.

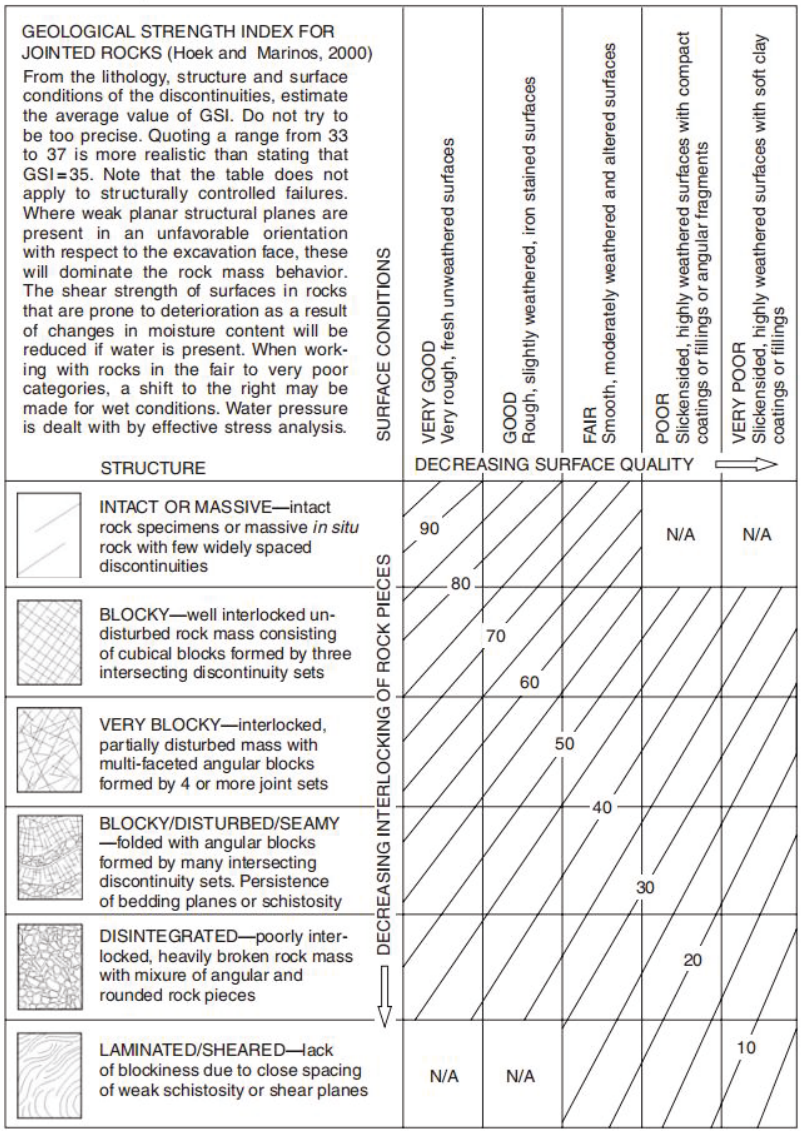

Figure 2.24 GSI values characterizing jointed rocks (Hoek & Marinos, 2000).

Table 2.9 Summary of m_i for different group of rocks (Davarpanah et al., 2021).

Rock type	Number of data sets	Measured m_i			
		Min.	Max.	Ave.	Std.
Igneous	32	4.31	34.03	15.42	7.13
Sedimentary	107	3.76	35.11	12.00	6.32
Metamorphic	46	1.43	32.33	13.3.6	10.07

The cohesion of clay, soil, or sand is not greater than approximately 40 kPa, while that of weathered soft rock or joints in hard rock is between 40 and 90 kPa and that of soft rock masses or overloaded jointed rock has a cohesiveness of between 90 and 190 kPa. Undisturbed jointed soft rock masses with few structures dipping out of the face have a cohesion of no more than 290 kPa, according to Hoek and Bray's (1981) back analysis of slope failure under various geological conditions. Based on the results of the back analysis investigation, almost all jointed rocks have friction angles between 35° and 45°.

Rock type	Class	Group	Texture			
			Coarse	Medium	Fine	Very fine
Sedimentary	Clastic		Congolomerate[a] (22 ± 3) Breccias (19 ± 5)	Sandstone (17 ± 4)	Siltstone (7 ± 2) Greywacke (18 ± 3)	Claystone (4 ± 2) Shales (6 ± 2) Marls (7 ± 2)
	Non-clastic	Organic Carbonates	Chalks (7 ± 2) Crystalline Limestone (12 ± 3)	Sparitic Limestone (10 ± 2)	Micritic Limestone (9 ± 2)	Dolomites (9 ± 3)
		Evaporites		Gypsum (8 ± 2)	Anhydrite (12 ± 2)	
Metamorphic	Non-foliated		Marble (9 ± 3)	Homfels (19 ± 4) Metasandstone (26 ± 6)	Quartzites (20 ± 3)	
	Slightly foliated		Migmatite (29 ± 3)	Amphibolites (26 ± 6)		
	Foliated[b]		Gneiss (28 ± 5)	Schists (12 ± 3)	Phyllites (7 ± 3)	Slates (7 ± 4)
Igneous	Plutonic	Light	Granite (32 ± 2) Granodiorite (29 ± 3)	Diorite (25 ± 5)		
		Dark	Gabbro (27 ± 3) Norite (20 ± 5)	Dolerite (16 ± 5)		
	Hypabyssal		Porphyries (20 ± 5)		Diabase (15 ± 5)	Peridotite (25 ± 5)
	Volcanic	Lava		Rhyolite (25 ± 5) Andesite (25 ± 5)	Dacite (25 ± 3) Basalt (25 ± 5)	Obsidian (19 ± 3)
		Pyroclastic	Agglomerate (19 ± 3)	Breccia (19 ± 5)	Tuff (13 ± 5)	

Figure 2.25 The Hoek–Brown constant m_i for various intact rocks (Cai, 2010).

The cohesion of clay, soil, or sand is not greater than approximately 40 kPa, while that of weathered soft rock or joints in hard rock is between 40 and 90 kPa and that of soft rock masses or overloaded jointed rock has a cohesiveness of between 90 and 190 kPa. Undisturbed jointed soft rock masses with few structures dipping out of the face have a cohesion of no more than 290 kPa, according to Hoek and Bray's (1981) back analysis of slope failure under various geological conditions. Based on the results of the back analysis investigation, almost all jointed rocks have friction angles between 35° and 45°.

2.4 Slope Stability Analysis Methods

To design slope safety and equilibrium, stability analysis is a critical calculation (Abramson et al., 2001). Slope stability can be assessed using a variety of approaches. The limit equilibrium method (LEM) is the most commonly used numerical technique for simple slope stability analysis (Eberhardt, 2003). When deformation, brittle fracture, or creep occurs within the slope, numerical modeling is more appropriate for assessing slope failure. The principles of slope stability analysis in two dimensions (2D) are briefly described in this section.

2.4.1 Limit equilibrium method

The limit equilibrium approach investigates the force balance at the time of rock slope failure (Lin et al., 2014). The rock slope's stability is determined by the shear strength generated along a certain potential sliding surface. Rocks are thought to have characteristics similar to those of Mohr-Coulomb

materials. When the rock mass's static equilibrium is seriously disturbed, the rock reaches its limit equilibrium condition (Wyllie & Mah, 2004). The safety factor is determined by dividing the shear strength force (resisting force) against the sliding surface by the shear stress (driving force) required to equilibrate the rock mass (Cheng & Lau, 2014). The shear strength of the rock mass is calculated according to Terzaghi's theory, which states that

$$\tau = c + \sigma' \tan\phi \tag{2.13}$$

where σ' is the effective stress acting on the sliding surface, and c and ϕ represent the cohesion and friction angle, respectively.

2.4.2 Finite element method

According to the LEM, each slice of the rock mass has the same factor of safety (FS). When the slope regime is complicated and variable, the FEM is better equipped to analyze the slope's failure deformation, particularly for modeling the materials' nonlinear stress-strain behaviour (Chowdhury et al., 2009). The shape and location of the failure surface do not need to be predicted in the FEM. The FEM may track the progression of the damage with consideration of the FS, which fluctuates with the sliding surface's slip.

FEM is a typical numerical technique for tackling two or three spatially variable edge-valued problems. The problem is discretized into smaller and simpler finite element subdomains, and these complete elements are then integrated into a mesh using this method (Nikishkov, 2009). On each domain, the unknown function is approximated. These equations are eventually combined into a global system of equations representing the entire problem and approximating the solutions (Logan, 2011). The procedure for finite element analysis can be composed of the following fundamental steps:

a. Subdivide the structural region into smaller finite elements, determining the number of elements and nodes at the intersection of the mesh.

b. Determine the interpolation or displacement model that applies to the principal variable. Assume that a suitable solution exists inside the element that approximates the displacement solution at any point inside the element (Bhavikatti, 2005), expressed as Equations 2.14 and 2.15:

$$u = \sum N_i u_i \tag{2.14}$$

$$v = \sum N_i v_i \tag{2.15}$$

where the approximating function N_i is the interpolation model, which often has a polynomial form.

c. Discover each element's stiffness characteristics and load vectors. The correlation between the nodal displacements and the nodal forces, or element stiffness matrix ($[k]_e$), follows Equation 2.16:

$$[k]_e\{\delta\}_e = \{F\}_e \tag{2.16}$$

The suitable variational principle, the weighted residual approach, or equilibrium conditions can be used to derive the nodal displacement vector $\{\delta\}_e$ and nodal load vector $\{F\}_e$ of element (Rao, 2017).

d. The overall equilibrium equation is established by properly combining all of the element stiffness equations. Equation 2.17 represents the global stiffness matrix $[k]$ equation (Bhavikatti, 2005).

$$[k]\{\delta\} = \{F\} \tag{2.17}$$

where $\{\delta\}$ and $\{F\}$ respectively represent the vector of all incremental element nodal displacements and the vector of nodal forces for the entire structure.

e. The global stiffness equation should be changed to account for the problem's boundary conditions to find a solution for the unidentified nodal displacements. When a problem is nonlinear, it is important to consider each step's correction of the force vector and the stiffness matrix (Rao, 2017).

f. Based on a precise relationship between displacements and stresses in solid mechanics, element strains and stresses are computed from known nodal displacements. Calculations frequently involve interpolation functions.

The FEM, a more effective technical technique for assessing heterogeneous soils or rocks with structured and irregular meshes, is selected in this study. The FEM can not only represent the behaviour of elastic-plastic materials but can also be applied to materials that are not linear and elastic, making it an excellent analytical method for fluid-structure interactions (Nikolić et al., 2016). Currently, the FEM has been proven to be a capable and reliable approach to estimating the FS of slopes, overcoming several limitations of the traditional LEM.

2.4.3 Shear strength reduction method – Based on the finite element method

Using the SSR method, Zienkiewicz et al. (1975) examined the stability of soil slopes. After more than three decades, Zheng and Zhao (2004) and Hammah et al. (2007) showed that the SSR method may also be used to analyze the stability of rock slopes. The SSR method, often known as the FE-SSR method, is currently one of the most widely used slope analysis approaches in FEM (Griffiths & Lane, 1999). The stress reduction factor (SRF) in the FE-SSR approach has the potential to overcome the slope to fail. As the friction angle (ϕ') and cohesion (c') of the rock slope change, the shear strength decreases due to the variable FS. The corresponding FS is the factor of safety for the slope when the rate of change of displacement in the FEM model of the rock slope suddenly increases or when the solution of the nonlinear equation does not converge (Cheng & Lau, 2014).

Typically, the nonlinear element makes use of the Mohr-Coulomb (MC) strength of rock slope materials. The following is an expression for the shear strength reduction process (Equation 2.18). The shear strength τ reduced by FS is derived from reduced Mohr-Coulomb shear strength parameters.

$$\frac{\tau}{F} = c^* + tan\,\phi^* \tag{2.18}$$

The reduced cohesion c^* and reduced internal friction angle ϕ^* can be defined by

$$c^* = \frac{c}{FS} \tag{2.19}$$

$$\phi^* = arc\,tan\left(\frac{tan\,\phi}{FS}\right) \tag{2.20}$$

where c and ϕ are the cohesion and inner friction angle of rock mass, respectively.

The generalized Hoek-Brown (GHB) criterion is the strength model that is most frequently used to examine nonlinear expressions of stress levels in rock masses (Hammah et al., 2005). Since the SSR technique cannot be used to directly reduce the strength parameters of a linear failure criterion (e.g., MC), the shear strength specified by this nonlinear failure criterion is also nonlinear. The slope safety factor can be confirmed using the GHB parameters, rock properties, and slope geometry instead (Sun et al., 2016). Equation 2.21 is used to depict the reduction of the GHB shear strength envelope.

$$\begin{aligned}\frac{\tau}{F} &= (\sigma_1 - \sigma_3)\frac{\sqrt{1 + am_b(m_b\frac{\sigma_3}{\sigma_{ci}} + s)^{a-1}}}{2 + am_b(m_b\frac{\sigma_3}{\sigma_{ci}} + s)^{a-1}} \cdot \frac{1}{F} \\ &= (\sigma_1 - \sigma_3)\frac{\sqrt{1+am_b^{red}(m_b^{red}\frac{\sigma_3}{\sigma_{ci}^{red}}+s^{red})^{a^{red}-1}}}{2+am_b^{red}(m_b^{red}\frac{\sigma_3}{\sigma_{ci}^{red}}+s^{red})^{a^{red}-1}}\end{aligned} \tag{2.21}$$

According to Balmer (1952), Equations 2.22 and 2.23 can be used to determine the shear strength τ and normal stress σ_n that correspond to a certain point on the principal stress envelope.

$$\tau = (\sigma_1 - \sigma_3)\frac{\sqrt{1+am_b(m_b\frac{\sigma_3}{\sigma_{ci}}+s)^{a-1}}}{2+am_b(m_b\frac{\sigma_3}{\sigma_{ci}}+s)^{a-1}} \tag{2.22}$$

$$\sigma_n = \frac{1}{2}(\sigma_1 + \sigma_3) - \frac{1}{2}(\sigma_1 - \sigma_3)\frac{am_b(m_b\frac{\sigma_3}{\sigma_{ci}}+s)^{a-1}}{2+am_b(m_b\frac{\sigma_3}{\sigma_{ci}}+s)^{a-1}} \tag{2.23}$$

where σ_{ci} is uniaxial compressive strength of intact rock, $m_b = m_i\exp(\frac{GSI-100}{28-14D})$, $s = \exp(\frac{GSI-100}{9-3D})$, and $a = \frac{1}{2} + \frac{1}{6}(e^{-GSI/15} - e^{-20/3})$. m_i, *GSI*, and *D* represent a property of intact rock, the geological strength index, and the disturbance factor, respectively.

The SSR technique's analytical process for determining the safety value of a stable slope to the brink of failure is as follows (Hammah et al., 2005).

Step 1: Determine an finite element (FE) model of the slope using the strength and deformation characteristics of the geotechnical materials, and note the maximum total deformation.

Step 2: To minimize the shear strength envelope, increase the value of FS. The new strength model parameters, after decreasing the envelope as the input values for the new strength properties of the slope model, are computed to determine the maximum total deformation.

Step 3: Repeat Step 2 while methodically increasing the FS-value until the FE model fails to converge to a solution. At that point, the slope fails. This process continues to lose material strength.

The crucial FS value at the moment of slope collapse is employed as the safety factor for the entire slope.

2.4.4 Convergence criteria

Tu et al. (2016) distinguished three categories of slope failure criteria, including:

a. The formation of continuous plastic regions, which is more ambiguous and challenging to quantify.

b. Abrupt changes in nodal displacements, where large displacements occur when the sliding zone of the slope becomes unstable.

c. Failure to reach the preset tolerance within the permitted number of iterations when solved using finite element or finite difference methods.

The non-convergence result obtained from solvers is taken into consideration as the sign of slope destruction.

The convergence criterion is used to determine slope stability in the FE-SSR method. The behaviour of exerting a single force on a nonlinear spring can be used to represent its solution process. The displacement U and the applied load P exhibit a nonlinear positive connection in this situation (Figure 2.26), and the relationship is as follows (Equation 2.24):

$$KU = P \tag{2.24}$$

where the spring stiffness $K = K(U)$ is a nonlinear variable dependent on displacement.

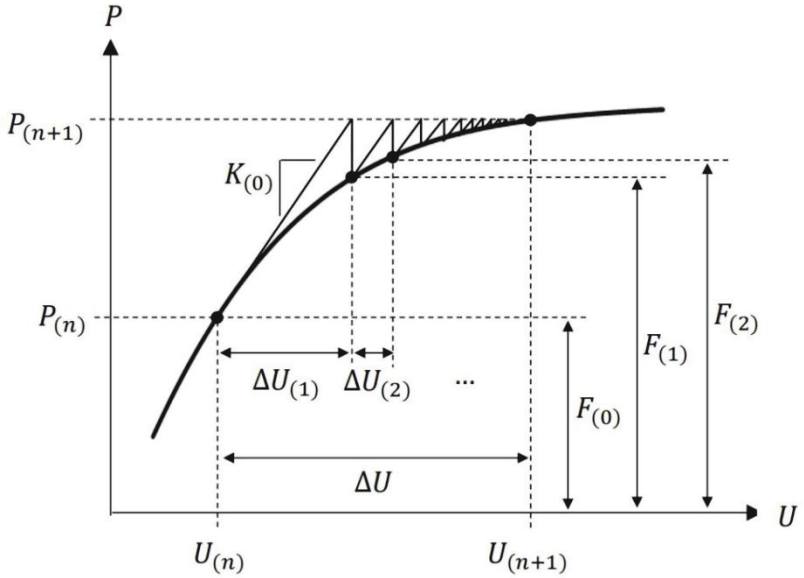

Figure 2.26 The response of a spring to applied loads (Rocscience, 2021).

The displacement increment ΔU can be used to designate the corresponding spring at the time the load step $P_{(n+1)}$ is applied (Figure 2.26). After the application of the load step $P_{(n)}$, the spring's displacement $U_{(n)}$ is assumed to be known. The displacement-load curve lies at the origin when no additional load steps are applied, and the spring's resisting (internal) force $F_{(0)}$ is sufficient to balance the applied (external) load $P_{(n)}$.

Equations 2.25, 2.26, and 2.27 can be used to update the displacement increments and solutions, and the tangent stiffness $K_{(0)}$ at this point will be used as the initial stiffness input in all iterations of the new load step.

$$K_{(0)}\Delta U_{(1)} = P_{(n+1)} - F_{(0)} \tag{2.25}$$

$$\Delta U_{(1)} = K_{(0)}^{-1}(P_{(n+1)} - F_{(0)}) \tag{2.26}$$

$$U_{(n+1)} = U_{(n)} + \Delta U_{(1)} \tag{2.27}$$

The displacement state can be used to calculate the present internal force $F_{(1)}$ in the spring. The load imbalance is extremely large at this point, $P_{(n+1)}$-$F_{(1)}$. The increment of displacement $\Delta U_{(2)}$ is less than that in the prior iteration $\Delta U_{(2)}$ while applying the same load step $P_{(n+1)}$ at displacement $U_{(n+1)}$ for the subsequent iteration. The magnitude of the calculated new internal force $F_{(2)}$ will be more comparable to that of the applied load. The displacement $U_{(n+1)}$ is considered the acceptable solution when the iteration brings the load imbalance $P_{(n+1)}$-$F_{(i)}$ near to or even to zero. The continuous iteration is terminated when the result is sufficiently close, with the stopping criteria that the procedure satisfies the absolute force and absolute energy criteria at the same time.

- Absolute force criteria:

$$\frac{\|P_{(n+1)} - F_{(i)}\|}{\|P_{(n+1)} - F_{(0)}\|} < (specified\ tolerance) \tag{2.28}$$

- Absolute energy criteria:

$$\frac{\sum_{j=1}^{N} |(p_{(n+1),j} - f_{(i),j})\Delta u_{(i),j}|}{\sum_{j=1}^{N} |(p_{(n+1),j} - f_{(0),j})\Delta u_{(1),j}|} < (specified\ tolerance) \tag{2.29}$$

Equations 2.28 and 2.29 are expressed in vector notation. $p_{(n+1)}$, $f_{(i)j}$, $f_{(0)j}$, $\Delta u_{(i)j}$, and $u_{(1)j}$ are the components of $P_{(n+1)}$, $F_{(i)}$, $F_{(0)}$, $\Delta U_{(i)}$, and $U_{(1)}$ respectively, where n is the total number.

2.4.5 Determination of factor of safety

The ratio of the shear stress to the driving force along the probable failure surface is known as the FS, which is a metric for measuring whether the resistance can withstand the assumed load. Slope failure occurs when the FS is less than 1.0 due to insufficient resistance to failure to balance the driving force (Assefa et al., 2016). Although slopes with FS greater than 1.0 are theoretically stable, it can be difficult to identify this critical failure in practice. Railways are currently subject to strict track settlement requirements. It is deemed adequate to apply a minimum FS of 1.5 on slopes for long-term loading conditions (Kramer, 1996). When the slope is erected temporarily or sufficient design information is available to analyze slope stability, the minimal FS for overall embankment stability can range from 1.3 (Indraratna et al., 2015).

2.5 Constitutive models for rocks

To characterize the behaviour of rocks, several constitutive models are suggested and implemented in FE modeling. The principles of the Mohr-Coulomb elastic-plastic model and the generalized

Hoek-Brown model, which are two of the most frequently used rock analysis models in RS2, are presented in this section.

2.5.1 Mohr-Coulomb model

In geotechnical modelling and design, the Mohr-Coulomb model is frequently implemented. It proposes that the analysis of the behavior of rock materials consists of a frictional coefficient and a continuous cohesion. As Coulomb proposed in 1773 (Davis & Selvadurai, 2002), the shear stress on the plane and the normal stress σ_n exerted on it have a linear relationship (Equation 2.30).

$$\tau = c' + \sigma_n \tan\phi \tag{2.30}$$

where τ is shear strength, ϕ is the frictional angle, and c' is effective cohesion.

The shear strength and the normal stress on the failure plane can be stated as follows by fusing the Coulomb criterion with the Mohr stress circle:

$$\tau = \frac{1}{2}(\sigma_1 - \sigma_3)\, cos\, \phi \tag{2.31}$$

$$\sigma_n = \frac{1}{2}(\sigma_1 + \sigma_3) - \frac{1}{2}(\sigma_1 - \sigma_3)\sin\phi \tag{2.32}$$

where σ_1, σ_2, and σ_3 represent the principal stresses in the three-dimensional space, and $\sigma_1 \geq \sigma_2 \geq \sigma_3$.

The yield function can be qualified by the Mohr-Coulomb failure criterion as follows when expressed in terms of principal stresses:

$$F_s = \frac{1}{2}(\sigma_1 - \sigma_3) + \frac{1}{2}(\sigma_1 + \sigma_3)\, sin\, \phi - c\, cos\, \phi = 0 \tag{2.33}$$

The yielding criterion and the plastic potential function have the same contour. The material strength decreases from its peak to a lower residual stress right after initial yielding. When the residual value equals the peak value, the elasto-brittle plastic material model is typically elasto-perfect-plastic.

The Mohr-Coulomb model yield surface can be represented in Equation 2.34 when tension is cut off:

$$F_T = \sigma_1 - T = 0 \tag{2.34}$$

where T is the material's tensile strength.

2.5.2 Generalized Hoek-Brown model

The generalized Hoek-Brown failure criterion, developed from Hoek's findings (Stagg & Zienkiewicz, 1968) for the brittle failure of intact rocks and Brown's conclusions (Brown, 1970) for the behaviour of jointed rock masses, is the most widely used strength model for rock masses. The generalized Hoek-Brown model examines the characteristics of intact rock first and then adds reduction factors to account for the behaviour of the rock mass when it is joined. The generalized Hoek-Brown model's failure criterion, stated in terms of primary stresses, is

$$F_s = \sigma_1 - \sigma_3 - \sigma_{ci}(m_b \frac{-\sigma_1}{\sigma_{ci}} + s_m)^{0.5} = 0 \tag{2.35}$$

In the above, m_b is the reduced value of the intact rock parameter m_i, and s_m is a material constant, reaching 1.0 when the rock is intact.

In Equation 2.35, 0.5 is changed to an additional parameter a when the generalized Hoek-Brown model reaches the yield surface, and the plastic potential function takes on the same form. Furthermore, GSI is implemented to assess the rock mass strength (equations presented in Section 2.4.3).

The material is typically treated as an elasto-brittle plastic material in the generalized Hoek-Brown model. When the residual stress value is equal to the peak value, the rock is regarded as elastic and perfectly plastic, similar to the Mohr-Coulomb model.

Equation 2.34 states that the generalized Hoek-Brown model's yield surface expression at tension cutoff is equivalent to that of the Mohr-Coulomb model. Equation 2.35 can be used to find the material's maximum tensile strength, denoted as T_{max} (Equation 2.36). The program actively employs T_{max} when the tensile strength is set higher than the maximum value of T. Hoek and Martin (2014) defined this alternative connection for tensile strength in Equation 2.37.

$$T_{max} = \frac{s_m \sigma_{ci}}{m} \tag{2.36}$$

$$T = \frac{\sigma_{ci}}{8.62+0.7m_i} \tag{2.37}$$

Chapter 3 Development of numerical model for rock slope stability analysis

3.0 Introduction

To verify the feasibility of using RS2 for the numerical simulation of this study, the numerical models of RS2 are generated in this chapter using the data from the literature, and the results are compared with the cases from the references. This study does not consider the behaviour of rails and sleepers, and all train loads on the contact surface of rail sleepers and ballast in the input model are calculated manually, with the study focusing on the track bed and subgrade layer. The model construction for external train loads, track structure, and natural slope is illustrated in Section 3.1. To showcase that the RS2 can accurately examine slope stability in these circumstances, a case comparable to this study is simulated in Section 3.2

3.1 Process of building the simulation model

The creation process of one of the leading models is outlined in this section. On the basis of the chosen track superstructure parameters, the external train loads produced on the sleeper-ballast contact surface are first computed. The dimensions of the track substructure and its components' properties are decided in the following stage. The model's fundamental construction is completed by entering all the data and assigning them boundary conditions for the upcoming production of the mesh elements.

3.1.1 Geometry of track and load condition

The design of the track to support the external train weight depends on the configuration of a heavy-haul freight train. With a load capacity of 36,000 lbs (160 kN) per axle (AREMA, 2012) and wagon wheel diameters following the International Union of Railways' standard size of 36 in (914 mm; Technical Specialist Rolling Stock Performance Standards, 2013), heavy-haul freight trains with four rolling stock axles are widely used in Canada. The sleeper's dimensions were determined as laid out in Section 2.3.2 and are presented in Table 3.1 below.

Table 3.1 Geometric parameters of sleeper (Starns, 2012; RTA, 2016).

Parameter	Value
Gauge (mm)	1,435
Spacing (mm)	495
Length (mm)	2,591
Width (mm)	229
Cross-sectional area (mm^2)	40,645

A freight vehicle is supported by two dual-axle trucks. The side and plan views of the railway vehicle dynamic model are shown in Figures 3.1 (a) and (b; Zhang et al., 2021). The separation between the axles of each truck is substantially smaller than that between the two trucks. Therefore,

while examining the longitudinal direction of the track, it is possible to simplify the two-wheel loads on each truck by computing the combined force of the two adjacent axles.

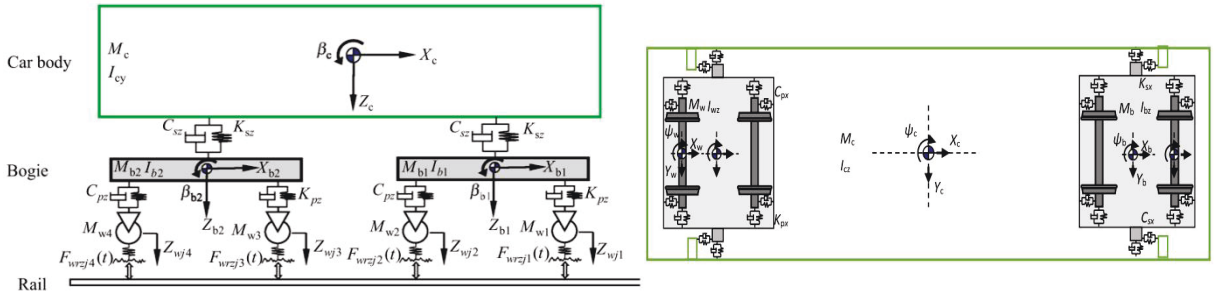

(a) (b)

Figure 3.1 Railway vehicle dynamic model (a) Side view; (b)Plan view (Zhang et al., 2021).

This study makes the following assumptions for the specified loading circumstances in order to determine external train loads:

a. Regardless of the varying lateral and vertical pressures it generates on the curved track, the train always travels along the tangential track.

b. The train speed is constant, with a impact load factor.

c. Every component of the system is in ideal condition: the track is level, the sleepers are flat and without corrosion, and the wheels are smooth.

d. The impact of environmental factors like wind and temperature is not taken into account.

The major calculation stages can be inferred from the mechanism of load transmission in wheel-rail-sleeper-ballast presented in Section 2.2.3 (see Figure 3.2). Equation 2.2 states that varied impact factors are produced by various train speeds.

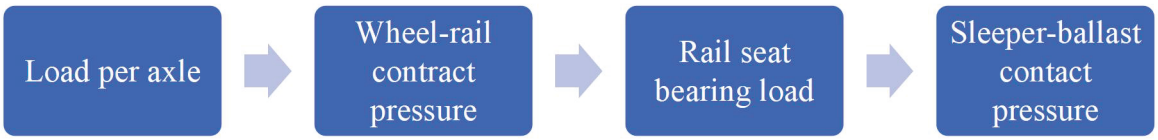

Figure 3.2 Flow chart for calculation of load conduction.

Table 3.2 Average bearing pressure at the sleeper-ballast surface for different train speeds.

Train speed	mph	0	25	50	75
	km/h	0	40	80	120
Impact factor (*IF*)	%	0	22.92	45.83	68.75
Load distribution factor (*DF*)	%	39			
Bearing area of the sleeper (*A*)	mm^2	593,339			
Average bearing pressure at the sleeper-ballast surface (P_{avg})	kPa	210.34	258.54	306.74	354.94

Accordingly, Table 3.2 displays the average contact pressure between the sleeper and ballast surface

for different train speeds. In this case, IF is computed by 33V/100D, where V (mph) is the known velocity and D (in) is the nominal wheel diameter (36 in). Figure 2.12 illustrates that a wooden sleeper with a spacing of 495 mm corresponds to a DF value of around 39%. A is derived by multiplying the length and width of the sleeper.

3.1.2 Geometry of the entire numerical model

The embankment beneath the train loads in this study is modeled in the following stage using the range of dimensions from Section 2.3.2. The dimensions of the portions of the embankment comprising ballast, subballast, and jointed rock subgrade layers are shown in Figure 3.3. The track's position in the model is set to 2.6 m long and 0.18 m thick since the length and thickness of the timber sleeper are 2.591 m and 0.178 m, respectively. The BDD and BSW are both set to 0.31 m in the model since AREMA (2010) specifies that they must both be greater than 0.3048 m. The SBD must be at least 0.3048 m and reach 1.2192 m or more from the edge of the ballast. As a result, the SBD and RBW are set to 0.31 m and 1.22 m, respectively, and each RBW is greater than the minimal restriction of 0.6096 m. Ballast, subballast, and jointed rock subgrade side slopes are all adjusted to 2H:1V. In this case, a uniform load transferred to the ballast surface of the model takes the place of the rail sleeper and the train.

Rock subgrade layers are constructed from rock fill. The rock fills are cut from the project's available materials to meet budgetary criteria. Rock fill, including hard and soft rock fill, is currently used effectively in railroad construction. Soft rock material includes quickly weathering exposed rock as well as rock that can be directly extracted through mechanical excavation without blasting; however, these materials tend to make the embankment impermeable (AREMA, 2018). Typically, the steepest slope for soft rock as fill material is set at 2H:1V. Conversely, hard rock fill can retain its strength even after extended exposure to the elements of nature and has a degree of weather resilience. The high proportion of voids in hard rock, however, causes long-term embankment settlement. Blasting is necessary to acquire the hard rock that is chosen for filling. The slope for embankments packed with hard rocks is typically 1.5H:1V or flatter. In a rock subgrade, a mixture of soft rock and hard rock is used as compacted fill, which is harder, stronger, and more permeable (AREMA, 2018). This provides reinforcement, slip resistance, and drainage, lowering the internal water ponding rate and reducing slope erosion. The void ratio of the rock fill decreases, thereby decreasing its propensity to settle. The slope of the rock subgrade is typically selected to be 2H:1V or less since the slope of the soft rock determines the slope of the hard rock.

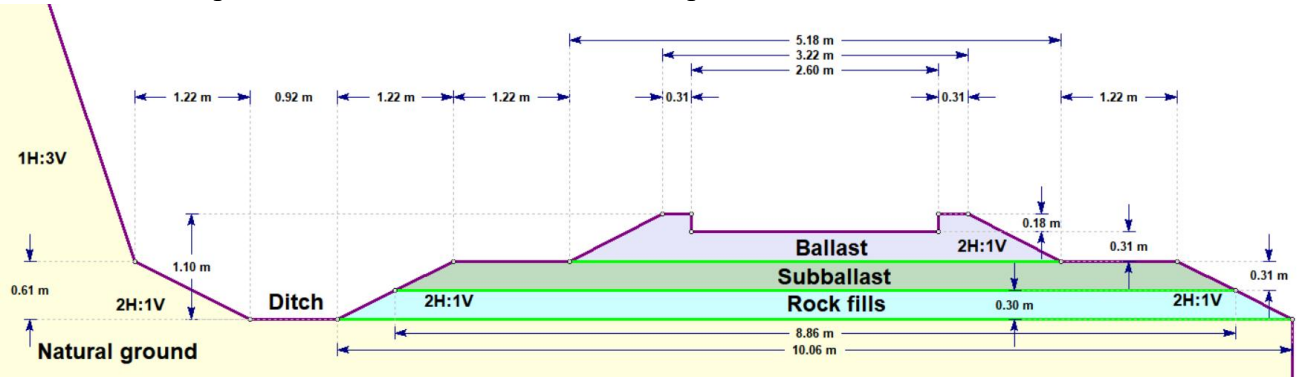

Figure 3.3 Typical cross-section of a railway embankment structure with dimensions.

The superstructure and ballast-subballast layer are supported by a 0.3 m layer of subgrade (Connolly et al., 2014). For this study, the embankment height is set to 1.1 m. One of the variables is the slope height of the natural ground, which is increased every 3 m from 3 m to 9 m. In both scenarios, the slope of the subballast and rock subgrade is assumed to be 2H:1V. The varying speeds of the freight trains are represented by the various uniform loads on the ballast surface.

Section 2.3.3 states that the bottom of the trapezoidal ditch is positioned at ground level and is 0.61 m away from the roadbed's shoulder, greater than the crucial value of 0.6096 m. The ditch's bottom is slated to be 0.92 m wide, which is wider than the required minimum of 0.9144 m, with a slope of 2H:1V on both sides (CN, 2019). As stated in Section 2.3.4, the jointed rock side slope ratios used in this study are 1H:3V and 1H:2V since the natural ground slope composed of jointed rock in the cut section has a steady dip angle of 70°.

To prevent stress from building up at the boundary, areas affected by stress reflections should be included in the model (Li et al., 2018). The letters in Figure 3.4 stand in for the natural ground, ditch, and embankment measurements of the natural slope with a slope ratio of 1H:3V and a slope height of 3 m. Equations 3.1 and 3.2 show that the length of the exposed natural ground on the left side is at least equal to the bottom width of the embankment and that the height of the natural ground on the right side is around three times the height of the railway embankment.

$$a \leq b + c + d \tag{3.1}$$

$$f \approx 3e \tag{3.2}$$

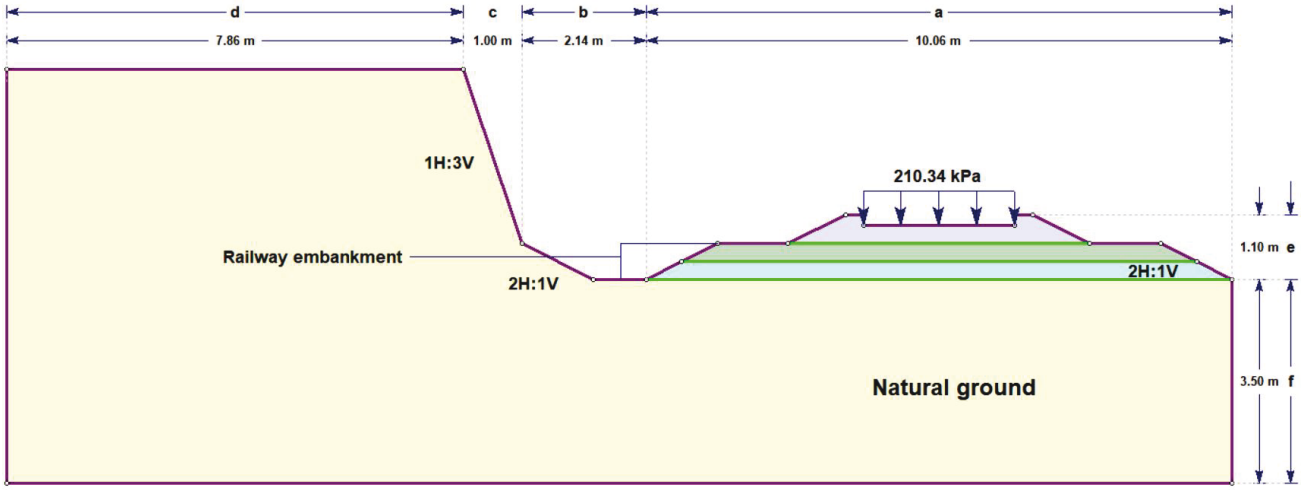

Figure 3.4 Typical cross-section of the numerical model with dimensions.

Due to the distinct joint features of the joined rock, nature ground has a particular type of joint network. This study examines the effects of joint orientation, spacing, length, and persistence on embankment stability using a set of parallel deterministic joints. Joint orientations exist in three dimensions. However, since the model chosen for this research is both a cross-section of natural ground and a rail embankment, The angles of joints in the two-dimensional plane can be completely represented in the range of 0°–180°, so all joints are mapped in the two-dimensional plane without using “Trace Plane” to simplify the calculation. Since topping failure is not considered in this mountainous terrain study, joints with 120° and 150° dips in the positive direction with the x-axis are employed.

Joint spacing and length are regarded as parallel and deterministic in accordance with Section 2.3.3. To ensure that the critical values are within the range of 0.006 m to 2 m (Wyllie & Mah, 2004), the spacing value is preserved at a 0.5 m gap from 0.5 m to 1.5 m, respectively, illustrating the range of joint spacing densities. Joint lengths of a 5 m interval are set from 5 to 15 m, respectively, due to the restriction of 1 to 20 m in typical size (Wyllie & Mah, 2004). The qualifying requirement is then presented as the ratio of joint length to the total joint length and rock bridge length (designated as length persistence). The joint persistence values used in this study, 0.3 and 0.7, are average persistence parameters chosen according to Hammah et al.'s research (Hammah et al., 2009), which reflect the situation of joints ranging from less discontinuous to fairly continuous.

Table 3.3 Values for joint length, spacing, and persistence.

Parameter	Value
Joint spacing (m)	0.5
	1.0
	1.5
Joint length (m)	1
	3
	5
Persistence	0.5
	0.7

The figures for joint length, spacing, and persistence are combined with a number of 18 (3*3*2) in Table 3.3. A model of the joint with a 30° inclination, a length of 5 m, and a persistence of 0.7 is depicted in Figure 3.5.

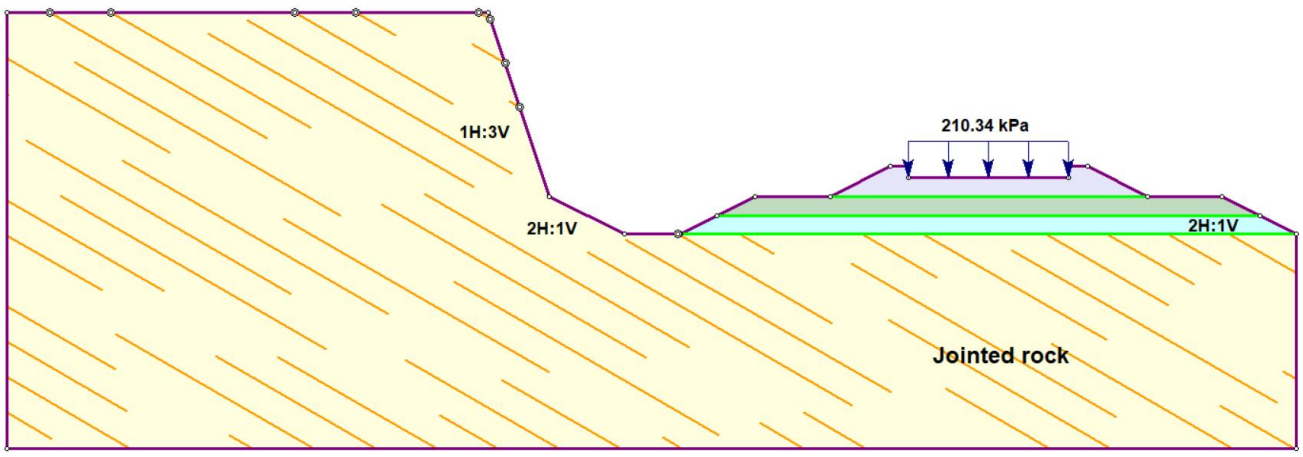

Figure 3.5 Typical cross-section of the numerical model with joint network.

3.1.3 Material properties

The model's upper layer is a ballast layer consisting of uniformly graded crushed stone that ensures the railroad's drainage. To prevent the ballast from filling the subgrade, the roadbed and ballast are separated by a coarse aggregate composed of gravel and sand.

The jointed rock masses for natural ground are soft, weathered rock, which is weak for failure. The

joints filled with recognizable filling material are thin. Weakly cohesive material with low friction exists in the joints of weathered rocks. Clay is the most typical joint infill for weathered rocks. A clay sample was chosen for this study that was gathered in a 2009 mountain rock landslide and selected as the joint fill for the necessary research. In the RS2 model, the joint element's thickness was set to zero to preserve numerical stability and the accuracy of the joint rock's behavior (Rocscience, 2023). As a result, the joint's interaction cohesion, friction angle, and tensile strength will be influenced by the material characteristics of the joint infills. Joint failure criteria adhere to the Mohr-Coulomb criterion. Young's modulus of the joint infills is used to determine the normal and shear joint stiffness (Equations 3.3 and 3.4).

$$K_s = C_s E_s \tag{3.3}$$

$$K_n = 10 K_s \tag{3.4}$$

where C_s is rock infills' stiffness coefficient, E_s is Young's modulus of the joint infills, K_s is shear joint stiffness, and K_n is normal joint stiffness.

The material properties of each structure employed in the study model are listed in Tables 3.4 (a) and (b). According to the Mohr-Coulomb failure criterion, ballast, subballast, and subgrade are elastoplastic materials. The natural ground taken from the sample of jointed quartz mica schist is defined according to the generalized Hoek-Brown criterion described by Jalote et al. (1996), whose values are calculated as described in Section 2.3.4.

Table 3.4 (a) Material properties with Mohr-Coulomb parameters (Profillidis, 2014; Allan, 2012; Karakus et al., 2016).

Material	Elasticity modulus (GPa)	Poisson's ratio	Cohesion c (kPa)	Friction angle ϕ (°)
Ballast	0.128	0.2	96.25	44
Subballast	0.196	0.3	95	40
Rockfills	2.942	0.2	1,471	20
Joints	N/A	N/A	50	35

Table 3.4 (b) Material properties with generalized Hoek-Brown parameters (Hoek, 2007; Jalote et al., 1996).

Material	Elasticity modulus (GPa)	Poisson's ratio	Intact UCS (MPa)	GSI	m_i
Jointed rock	10	0.17	30	65	10

3.1.4 Boundary conditions

The numerical model's boundaries are defined at the bottom, left, and right sides. The model's left side is fixed in the horizontal direction, allowing the sample to be deformed vertically, particularly under the influence of gravity. Furthermore, the bottom of the model (including the corners) is confined in both the horizontal and vertical directions, with no displacement allowed in any direction. The numerical simulation keeps the boundary conditions constant. A typical simulation model available for analysis is presented in Figure 3.6.

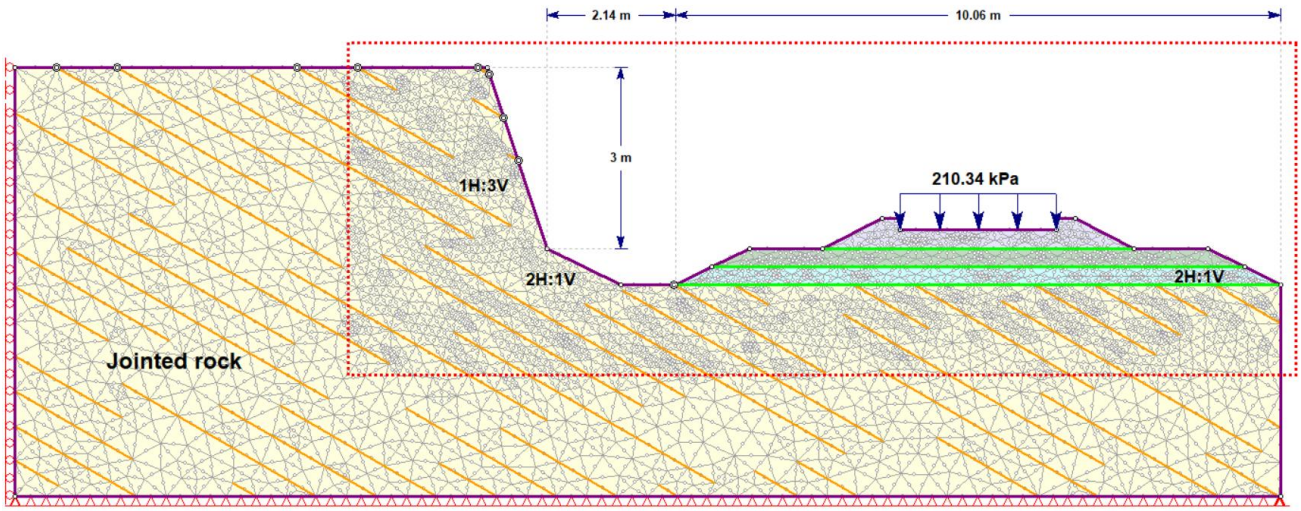

Figure 3.6 Typical cross-section of a complete model.

3.1.5 Mesh convergence study

Mesh convergence is the process of finding the best solution by decreasing the size of the elements in a specific area (discretization). After discretization, the number of elements increases along with the accuracy of the results. When an increase in the number of mesh elements has almost no impact on the simulation results, the finite element simulation produces its best results.

A six-noded (quadratic interpolation order with mid-side nodes) triangle is defined as a finite element mesh type. The meshes in the model are all uniform, with the same type of triangles. The boundaries should be discretized prior to the creation of the domain mesh. The boundary discretization and mesh density are increased in the nearly rectangular area surrounding the embankment and potential sliding surfaces, as shown by the dashed area in Figure 3.7, to ensure that the elements are concentrated in the sample focus area.

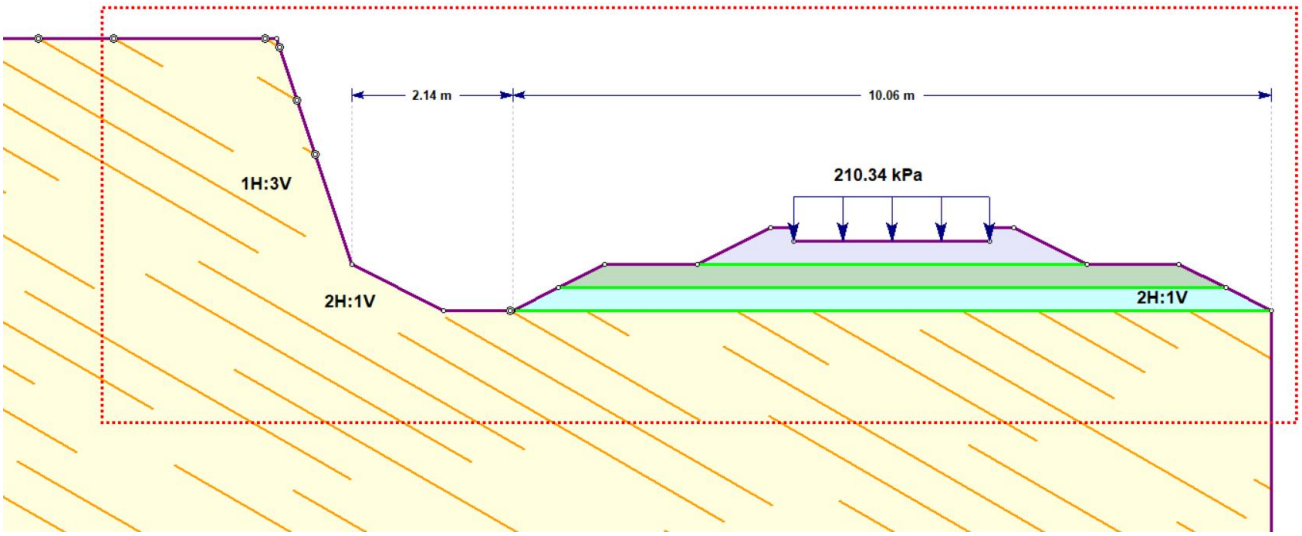

Figure 3.7 Area of the numerical model with higher boundary discretization and element densities.

3.2 Verification

In this section, two examples of jointed rock slopes are chosen and examined using RS2. The results of the RS2 operation are compared to those in the examples to demonstrate that RS2 can be utilized as a tool for FE-SSR analysis of numerical models. The results obtained from UDEC software (another SSR analysis software) given in the literature are used as reference values.

3.2.1 Model description

The model for Case I includes a component for plane failure, which is based on the jointed rock slope with non-daylighting discontinuities from Wyllie and Mah (2004). Figure 3.11 (b) depicts the damage mechanism in Case II, where a breakthrough failure at the slope toe causes joint slip (Alejano et al., 2011). The inclination of the joint set is identical to the slope inclination angle on the partially joint-controlled slope. For the two cases, the geometry setting parameters for the slope and joints in RS2 are shown in Figures 3.8 and 3.9, while the material characteristics are presented in Table 3.5.

Figure 3.8 Geometry of Case I model for verification.

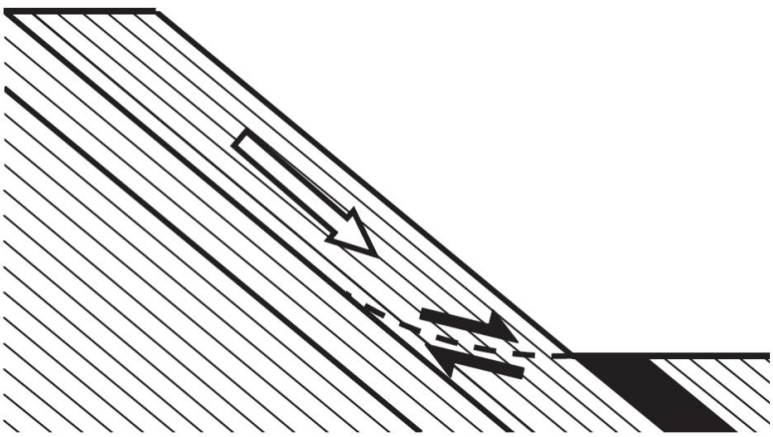

Figure 3. 9 (a) Partially Joint-Controlled Slope Failure (Alejano et al., 2011).

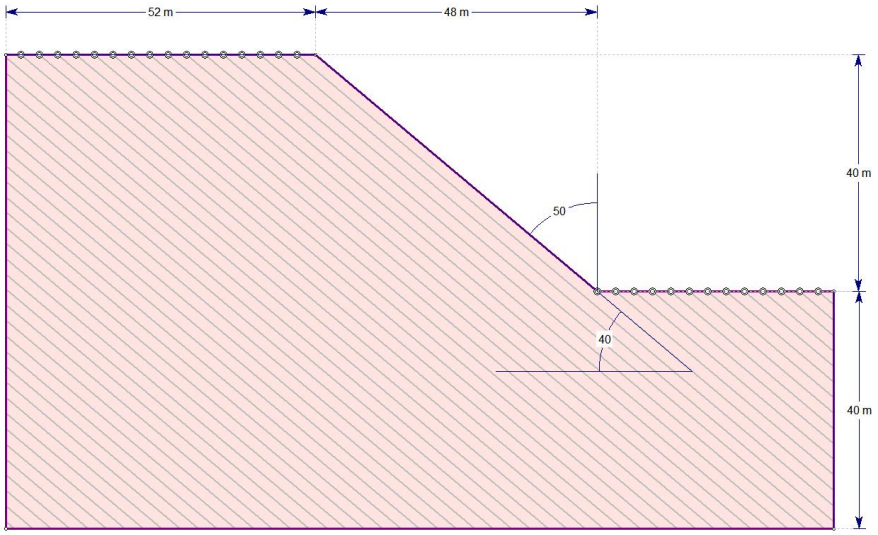

Figure 3.9 (b) Geometry of Case II model for verification.

Table3. 5 (a) Material properties of model in Case I for verification.

Slope angle (°)	Unit weight (kN/m^3)	Possion's ratio	Cohesion (kN/m^2)	Friction angle (°)	Young's modulus (MPa)	Joint angle (°)	Friction angle of joint (°)	Cohesion of joint (kN/m^2)	Joint spacing (m)
55	26.1	0.26	675	43	9072	70	40	100	20

Table 3.5 (b) Material properties of model in Case II for verification.

Slope angle (°)	Unit weight (kN/m^3)	Possion's ratio	Cohesion (kN/m^2)	Friction angle (°)	Young's modulus (MPa)	Joint spacing (m)	Friction angle of joint (°)
40	28	0.3	200	35	1000	2	25

3.2.2 Results and discussion

Figures 3.10 and 3.11 depict the model computations' outcomes as well as the results of the RS2 analysis for the two cases. The analytical works of the SSR method are contrasted with those of RS2 in Table 3.6.

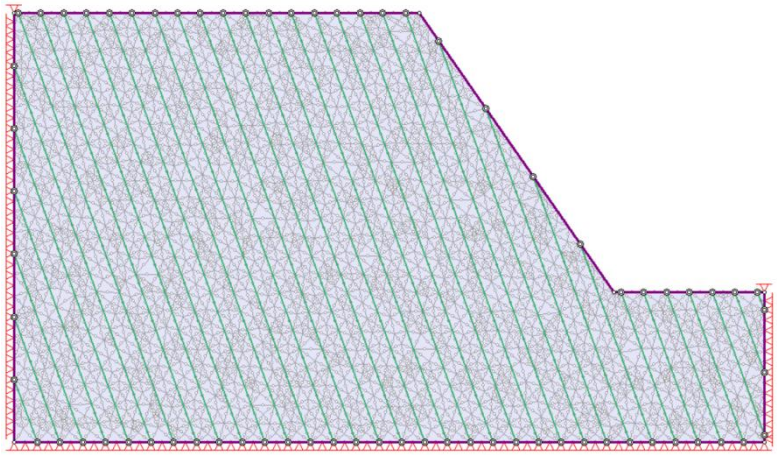

Figure 3.10 (a) RS2's Finite Element Mesh (6-noded triangles) in Case I model.

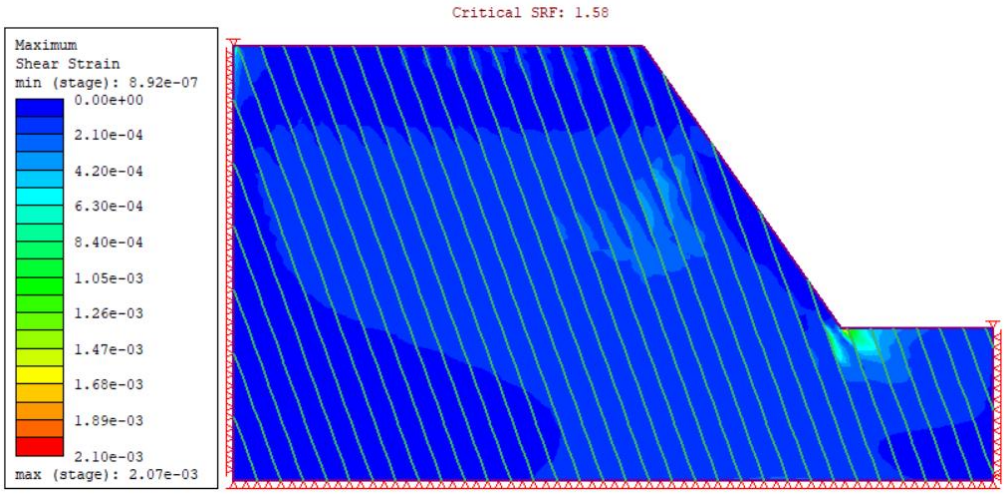

Figure 3.10 (b) Result of Case I model obtained from RS2 with an SRF of 1.58.

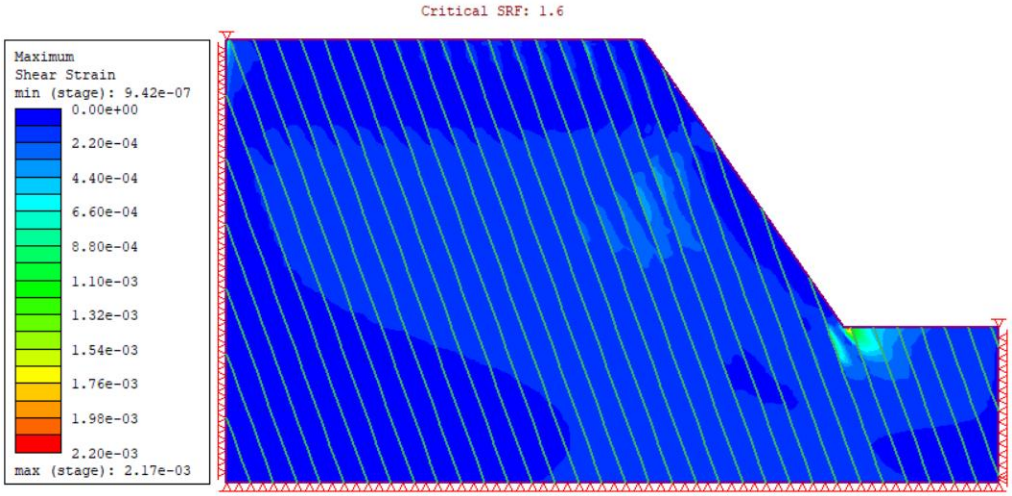

Figure 3.10 (c) RS2 Result of Case I model with improved joint convergence (SRF = 1.6).

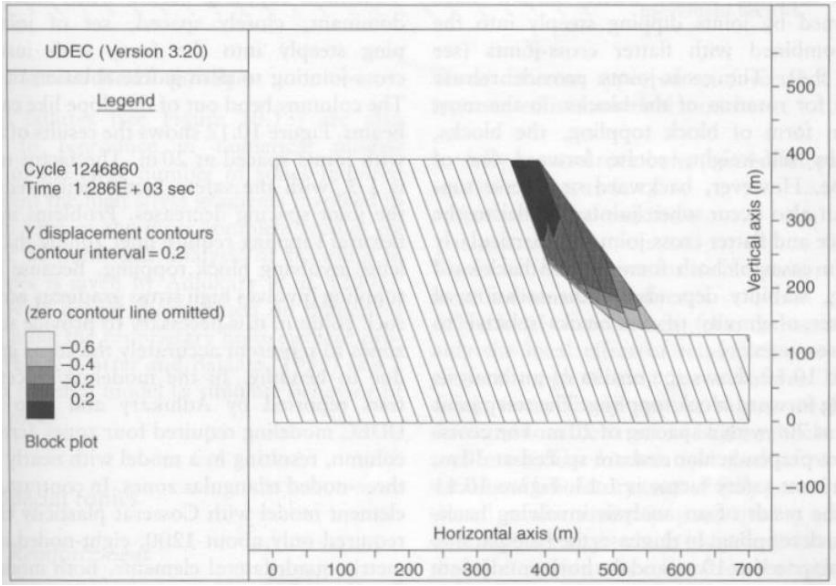

Figure 3.10 (d) Deformation and results in UDEC analysis (Wyllie & Mah, 2004).

By constantly adjusting the convergence criteria in the SSR analysis, as shown in Figures 3.10 (c) and 3.11 (c), the convergence of the joint is improved. The program instantly updates the stiffness of the joint when the joint breaks the strength criterion to create a more accurate solution.

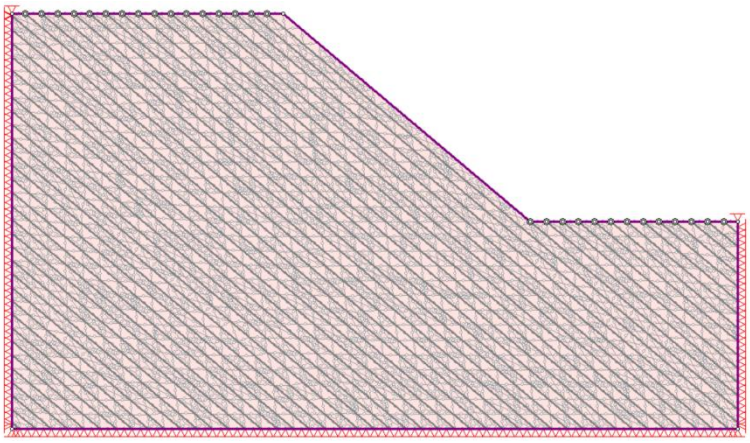

Figure 3.11 (a) RS2’ s Finite Element Mesh (6-noded triangles) in Case II model.

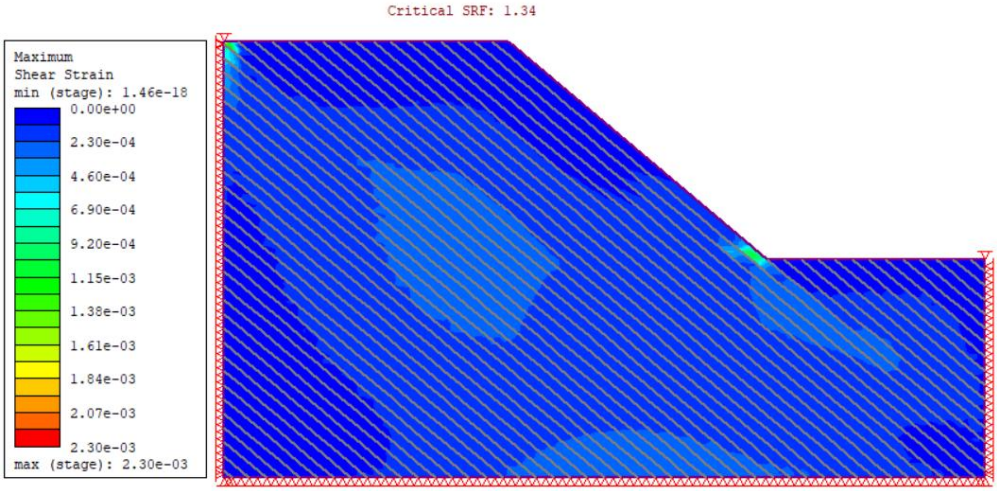

Figure 3.11 (b) Result of Case II model obtained from RS2 with an SRF of 1.34.

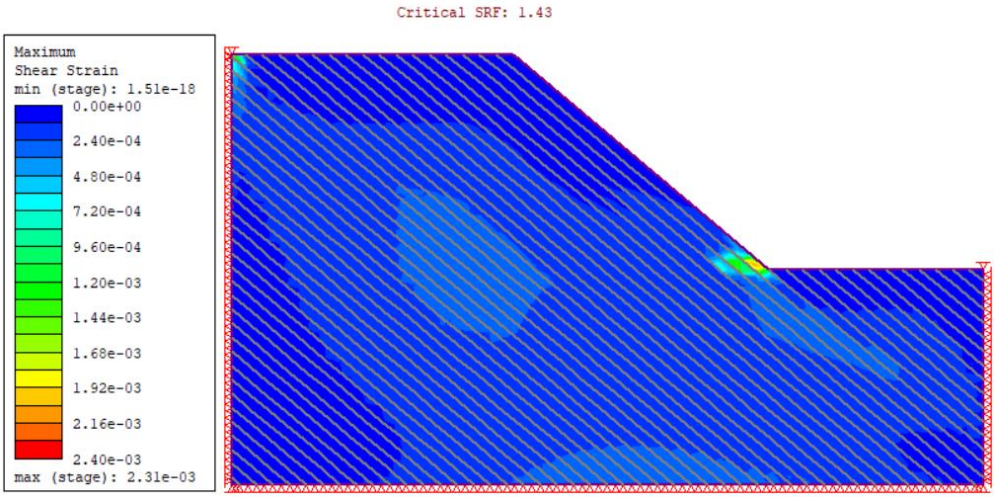

Figure 3.11 (c) RS2 Result of Case II model with improved joint convergence (SRF = 1.43).

Table 3.6 Comparison of safety factor values obtained by different methods in each case.

Cases	Factor of safety		
	RS2		Reference
	Without the improvement of joint convergence	With the improvement of joint convergence	UDEC
Case I	1.58	1.60	1.50
Case II	1.34	1.43	1.60

In light of the findings described above, the failure mechanism of each RS2 model is consistent with the corresponding SSR failure mechanism in the literature, and the critical SRF values are relatively close to the safety factors from UDEC software presented in the literature. In this research, it is clear that the FE-SSR simulation in RS2 is capable of generating reliable analytical results.

Chapter 4 Analysis of jointed rock and discussion of simulation results

4.0 Introduction

Two alternative sets of numerical models are examined using the FEM tool RS2. Each group of models, which acts as a control group for the other one, has a different specified operating condition. Set I consists of simulations of jointed rock slopes beneath the railroad. Set II comprises models of jointed rock slopes under moving train load circumstances. Each set of models in the study is constructed and examined using the control variable method.

This chapter is composed of four sections. Section 4.1 defines the two model groups. Section 4.2 gives a parametric analysis of the Set I model. The Set II model, generally referred to as the Set I model incorporating train loads, is investigated in Section 4.3. The relationship between slope geometry, joint characteristics, and the maximum safe train speed is summarized in Section 4.4, after which conclusions are drawn.

4.1 Two sets of models

The effects of joint characteristics and freight train operation on the stability of rock slopes are investigated through two sets of models. Set I models include a description of the rock slope model of the roadbed and natural ground, including varied joints. The second set of models examines the safety variation of jointed rock slopes in Set I under various train load scenarios. The study does not consider the groundwater level since the model used a rail line carved out of a rock slope. The grouping of parameters to be examined, the model simulation results, and the critical safety factor values are all interpreted for each group of models.

4.1.1 Set I – Jointed rock slope model

The entire rock slope without loading attachments, cracks, and joints is known as the intact rock slope. The roadbed side slope ratio and rail embankment height are the two parameters that are taken into consideration in this circumstance. The values of each parameter are taken from Figure 3.3 and Section 3.1.2.

One of the parameters is the rock slope. There are two situations in which the ratio of horizontal to vertical is 1:3 and 1:2. The railroad embankment's height is fixed at 1.1 m. The natural jointed rock slope height (h) of the cut section is set to 3, 6, or 9 m. The other model dimensions are obtained from Section 3.1 and held constant throughout the investigation.

In addition to the two factors stated above, slope ratio and natural slope height, the study parameters of the joint rock slope model also include the direction, spacing, length, and persistence of the joints. Section 3.1.2 provides a detailed description of these parameters' values. The joint set's orientation is chosen to be either 30° or 60°. The joint spacing is set to 0.5, 1, or 1.5 m, length to 1, 3,

or 5 m, and persistence to 0.5 or 0.7. From top to bottom, Figure 4.1 displays the values of each parameter as well as the combinations of the six factors evaluated in the rock-slope model with different joint sets, with a total of 216 examples investigated and studied. Appendix A contains a list of all the model cases for Set I, which are split into six groups, with 12 subgroups in each group.

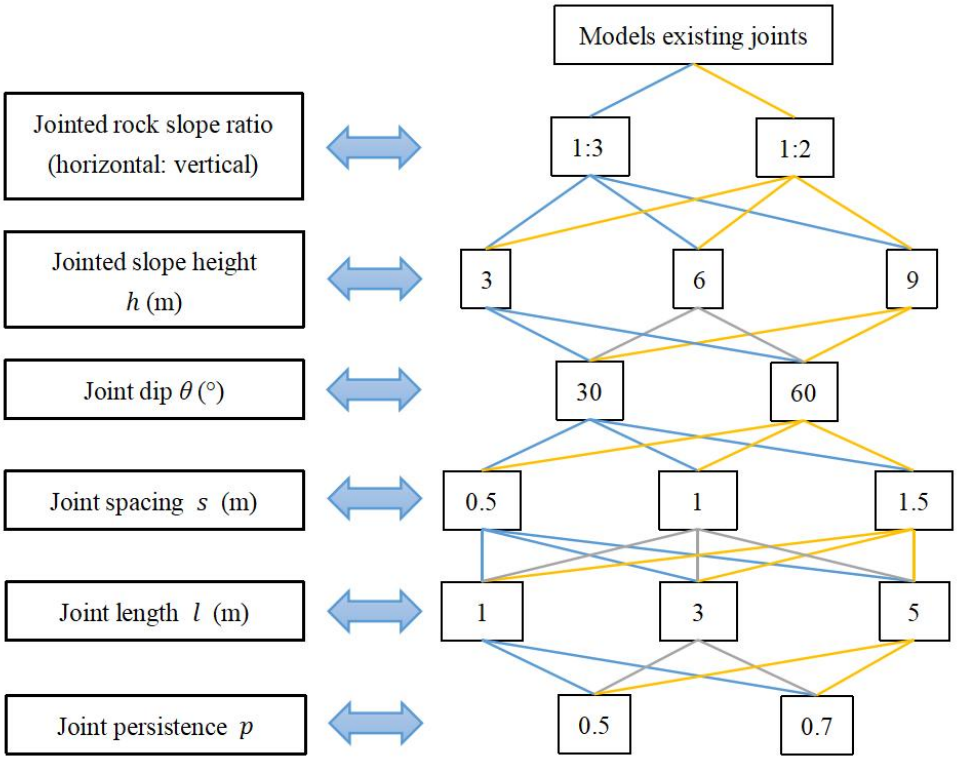

Figure 4.1 Diagram of various cases in Set I – Jointed rock slope model.

Figure 4.2 depicts several representative models, one for each group listed in Table A1 of Appendix A: Subgroups 4, 16, 28, 40, 52, and 64. All subgroups feature parallel deterministic joints with 1 m spacing, 1 m length, and persistence of 0.7, and their joint sets are all oriented at 60°. The model configurations in Figures 4.2 (d), (e), and (f) decrease the slope ratio from 1H:2V to 1H:3V against Figures 4.2 (a), (b), and (c), respectively. The jointed slope height is raised from 3 m to 6 m and 9 m in Figures 4.2 (b) and (c), contrasting with the model in Figure 4.2 (a). Similarly, in Figures 4.2 (e) and (f), the slope height is increased by 3 m and 6 m, respectively, in comparison to the model in Figure 4.2 (d).

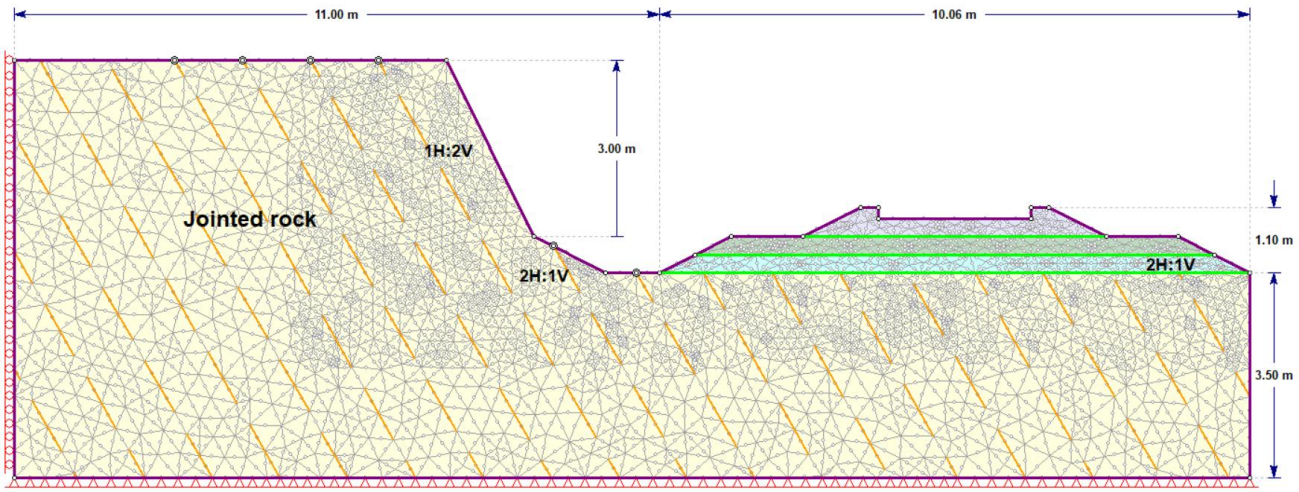

Figure 4.2 (a) Subgroup 4 model geometry: slope ratio = 1H:2V, h = 3 m, θ = 60°, s = 1 m, p = 0.7, l = 1 m.

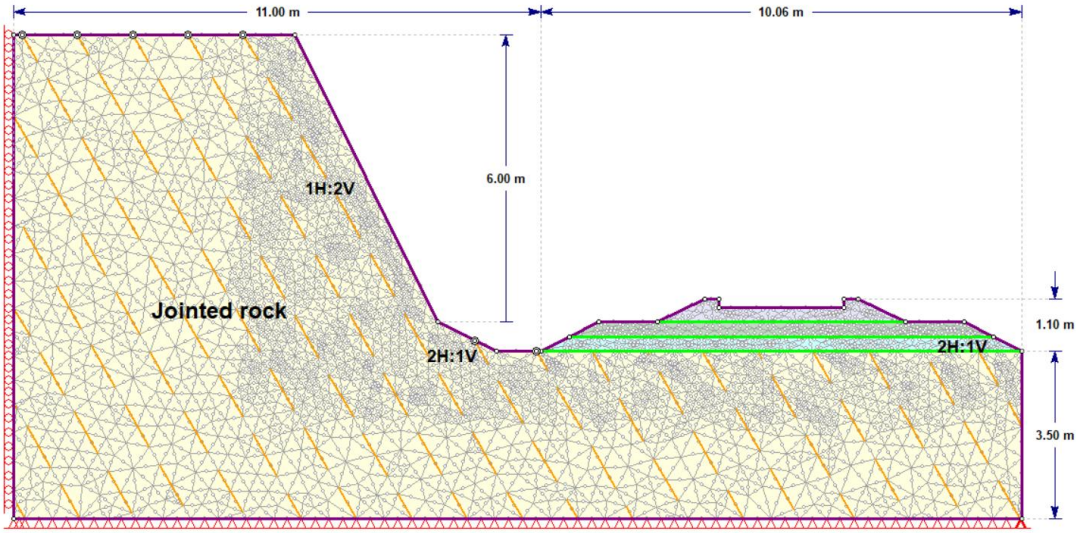

Figure 4.2 (b) Subgroup 16 model geometry: slope ratio = 1H:2V, h = 6 m, θ = 60°, s = 1 m, p = 0.7, l = 1 m.

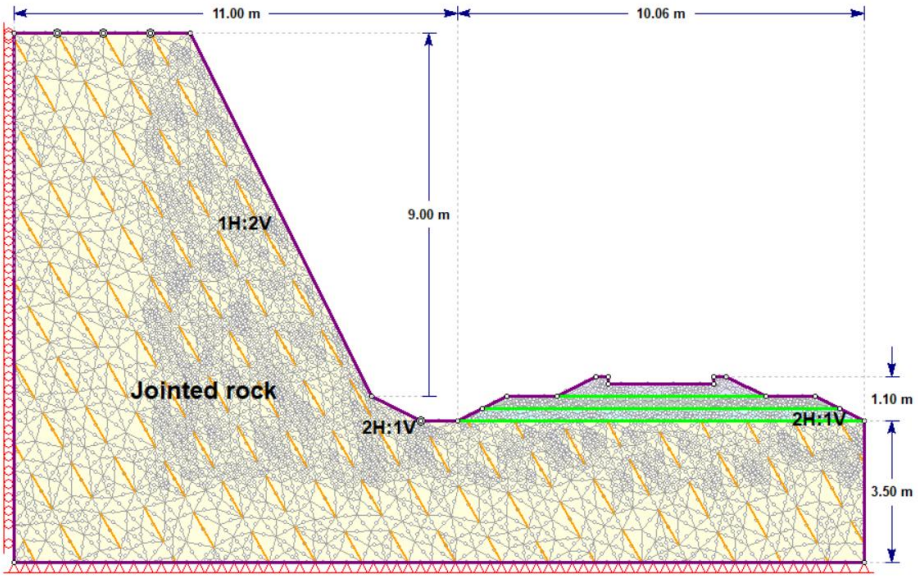

Figure 4.2 (c) Subgroup 28 model geometry: slope ratio = 1H:2V, h = 9 m, θ = 60°, s = 1 m, p = 0.7, l = 1 m.

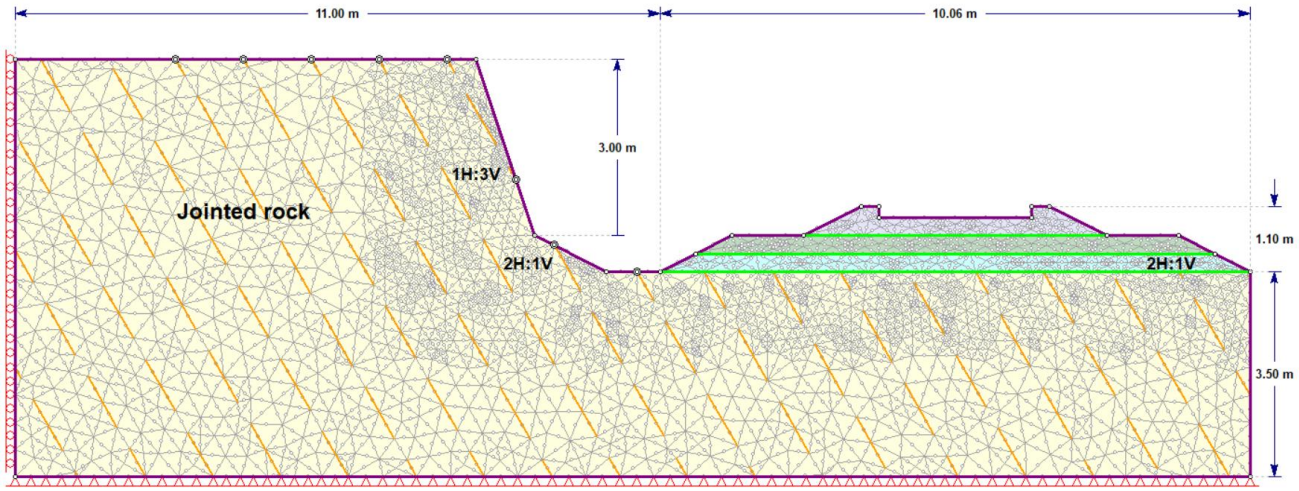

Figure 4.2 (d) Subgroup 40 model geometry: slope ratio = 1H:3V, h = 3 m, θ = 60°, s = 1 m, p = 0.7, l = 1 m.

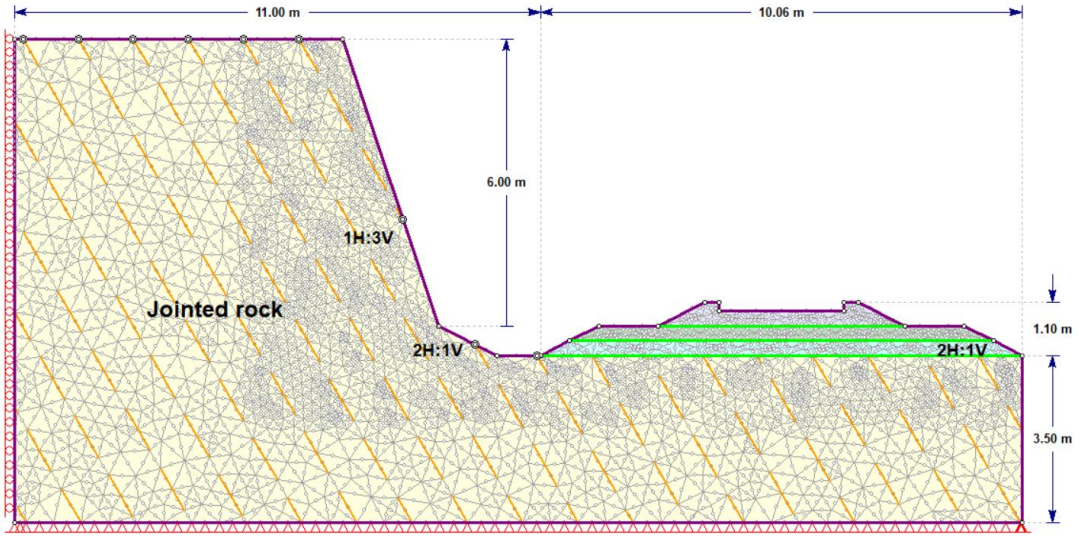

Figure 4.2 (e) Subgroup 52 model geometry: slope ratio = 1H:3V, h = 6 m, θ = 60°, s = 1 m, p = 0.7, l = 1 m.

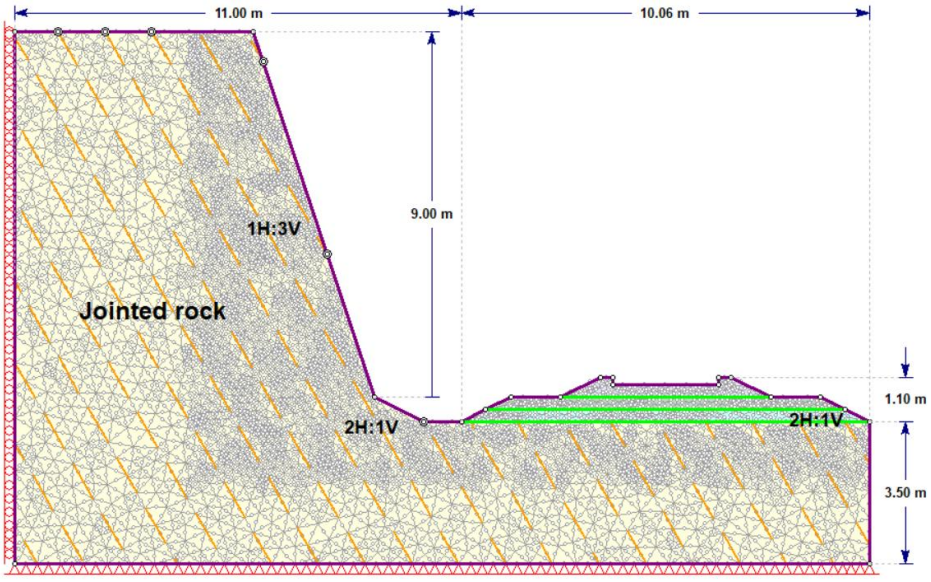

Figure 4.2 (f) Subgroup 64 model geometry: slope ratio = 1H:3V, h = 9 m, θ = 60°, s = 1 m, p = 0.7, l = 1 m.

The critical SRF values and maximum shear strain contours of the models are visible in Figure 4.3, which displays the corresponding simulation results of the models given in Figure 4.2. The models in Figures 4.3 (a), (b), and (c) have critical SRF values of 10.51, 8.31, and 7.73, respectively, which are higher than the results produced by the corresponding models for the same conditions except for the slope increase (10.42, 8.14, and 6.9, respectively) in Figures 4.3 (d), (e), and (f). The simulation results suggest that the relative flatness of the slope increases the model's stability. Furthermore, Figure 4.3 shows that the model damage happens through slip lines due to joint connection and cracking at the joint generation, all contributing to the railroad's instability.

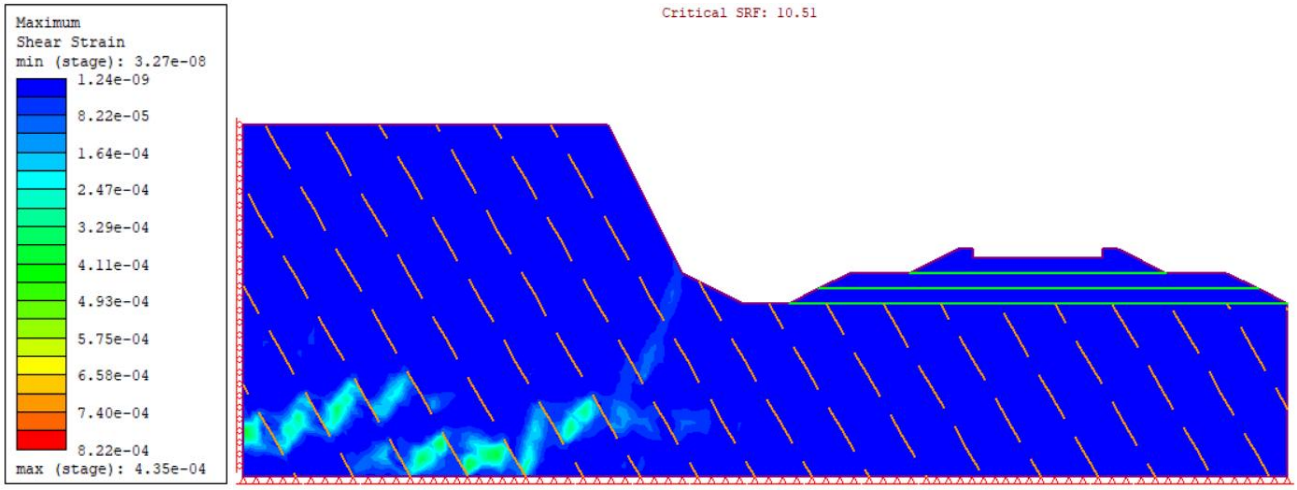

Figure 4.3 (a) Simulation result for Subgroup 4 model: slope ratio = 1H:2V, h = 3 m, θ = 60°, s = 1 m, p = 0.7, l = 1 m.

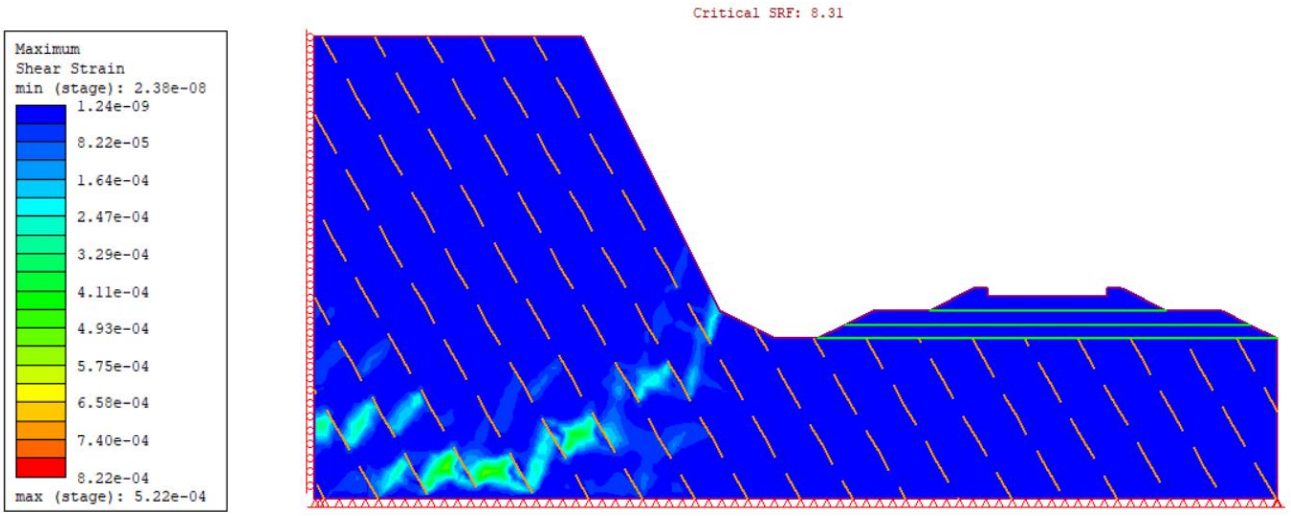

Figure 4.3 (b) Simulation result for Subgroup 16 model: slope ratio = 1H:2V, h = 6 m, θ = 60°, s = 1 m, p = 0.7, l = 1 m.

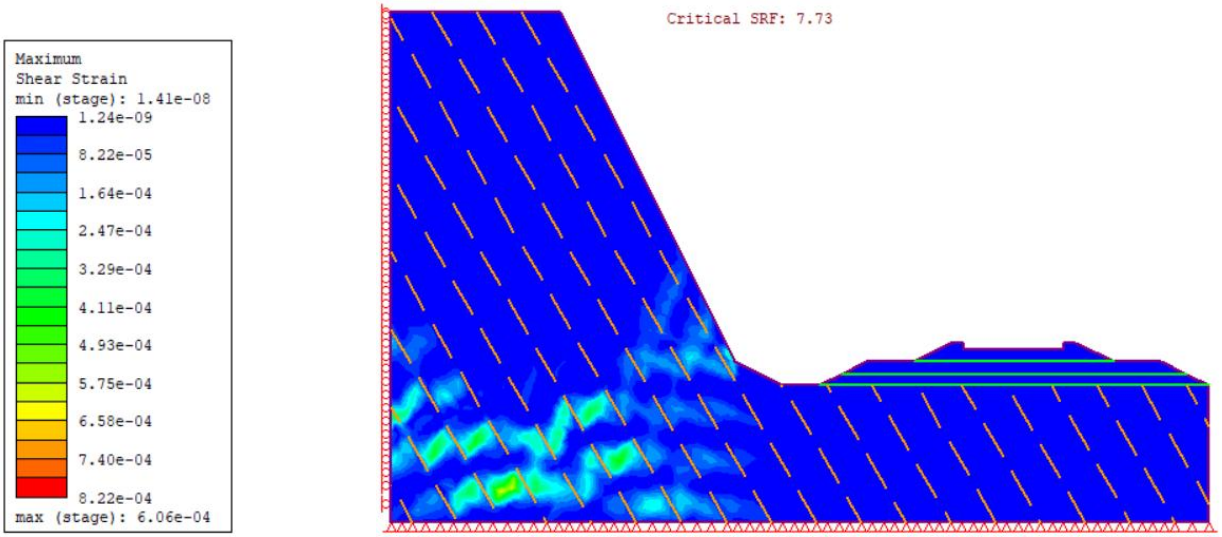

Figure 4.3 (c) Simulation result for Subgroup 28 model: slope ratio = 1H:2V, h = 9 m, θ = 60°, s = 1 m, p = 0.7, l = 1 m.

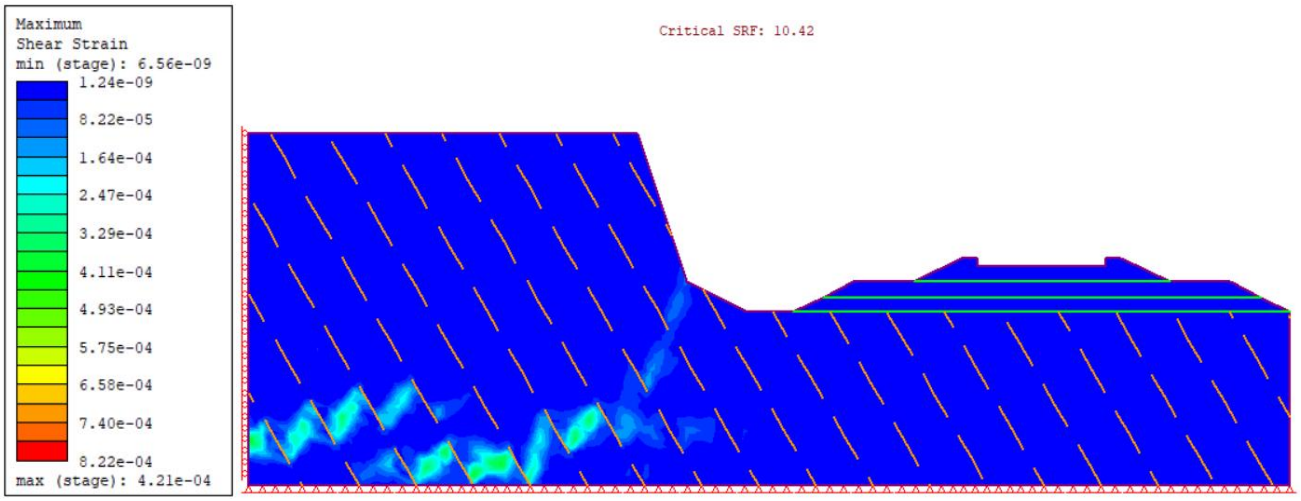

Figure 4.3 (d) Simulation result for Subgroup 40 model: slope ratio = 1H:3V, h = 3 m, θ = 60°, s = 1 m, p = 0.7, l = 1 m.

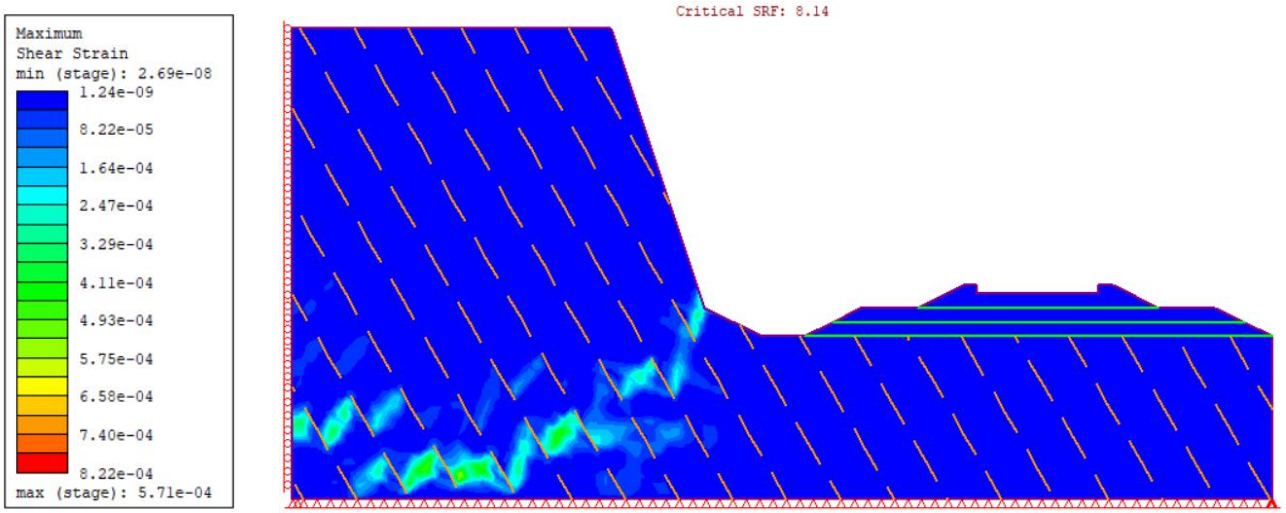

Figure 4.3 (e) Simulation result for Subgroup 52 model: slope ratio = 1H:3V, h = 6 m, θ = 60°, s = 1 m, p = 0.7, l = 1 m.

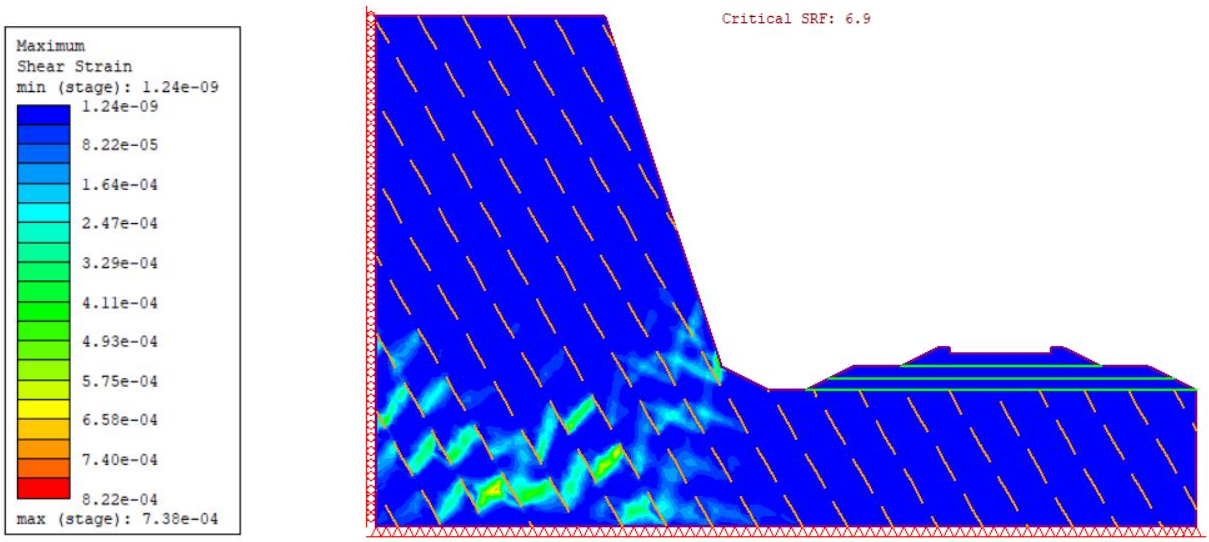

Figure 4.3 (f) Simulation result for Subgroup 64 model: slope ratio = 1H:3V, h = 9 m, θ = 60°, s = 1 m, p = 0.7, l = 1 m.

To identify the slope stability affected by the direction, spacing, length, and persistence of joints, a result from Subgroup 16 is used as a control group for the model in Figure 4.3 (b), and research is conducted on the influence of each joint parameter on slope stability using the control variable method. The models in Figure 4.4 (a)–(d) differ from the model in Figure 4.2 (b) solely in the value of one parameter, while the other parameters remain unchanged. The orientation of the joint set is fixed to 30° by the model (in Subgroup 22) chosen in Figure 4.4 (a). Persistence is increased to 0.5 by the model from Subgroup 15, which is shown in Figure 4.4 (b). In Subgroup 18, the model where Figure 4.4 (c) is placed decreased the joint spacing from 1 m to 0.5 m. The outcomes of numerical modeling with a joint length of 3 m (in Subgroup 16) are displayed in Figure 4.2 (d), which contrasts with the model in Figure 4.2 (b).

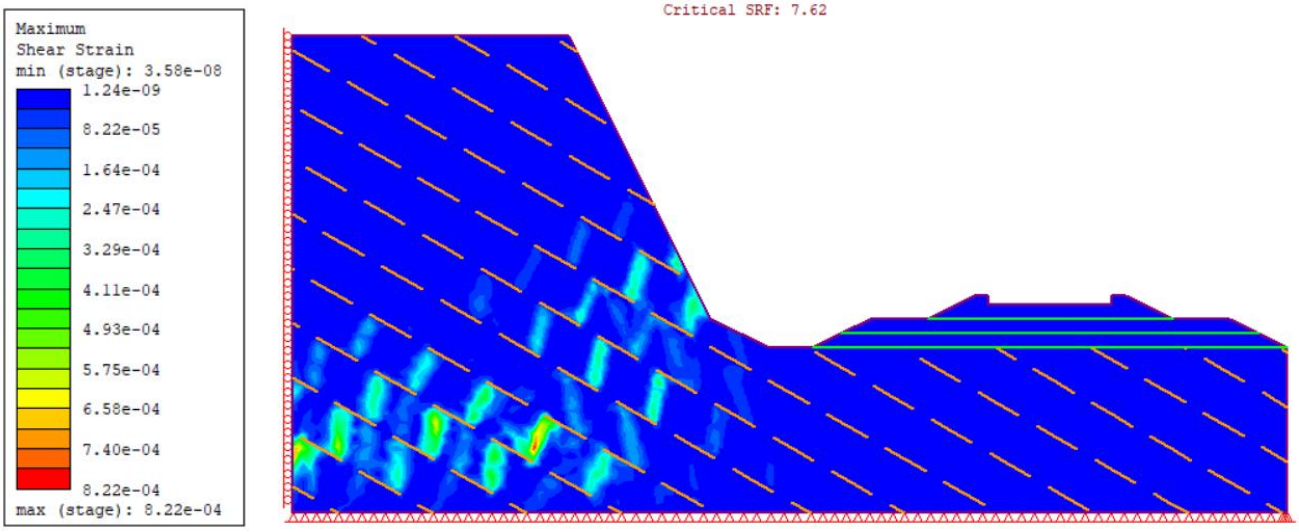

Figure 4.4 (a) Simulation result for Subgroup 22 model: slope ratio = 1H:2V, h = 6 m, θ = 30°, s = 1 m, p = 0.7, l = 1 m.

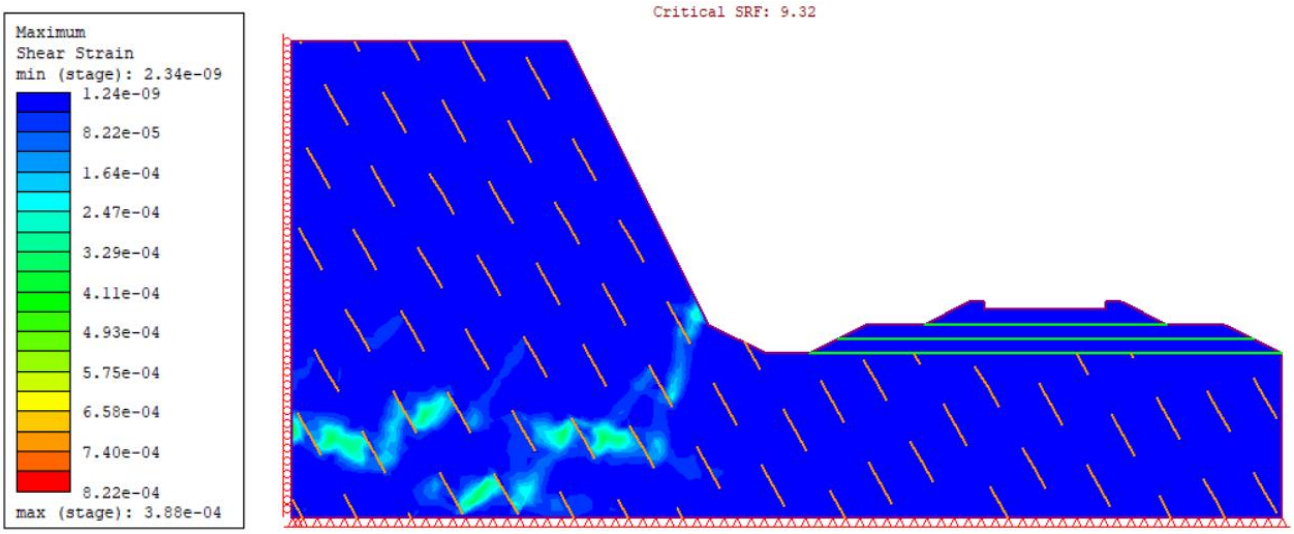

Figure 4.4 (b) Simulation result for Subgroup 15 model: slope ratio = 1H:2V, h = 6 m, θ = 60°, s = 1 m, p = 0.5, l = 1 m.

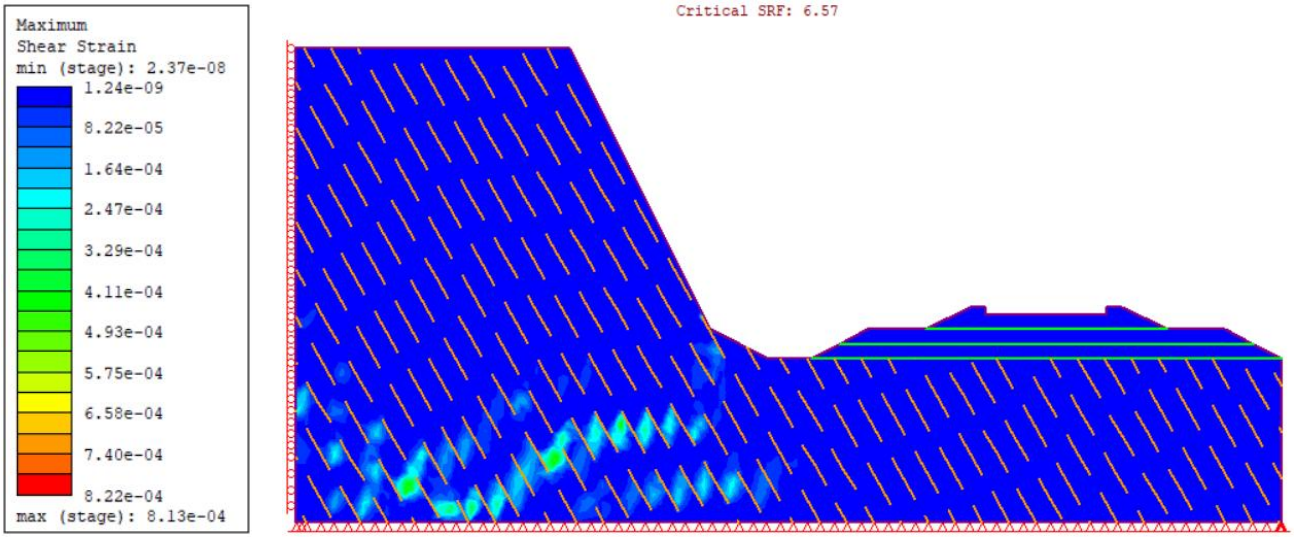

Figure 4.4 (c) Simulation result for Subgroup 18 model: slope ratio = 1H:2V, h = 6 m, θ = 60°, s = 0.5 m, p = 0.7, l = 1 m.

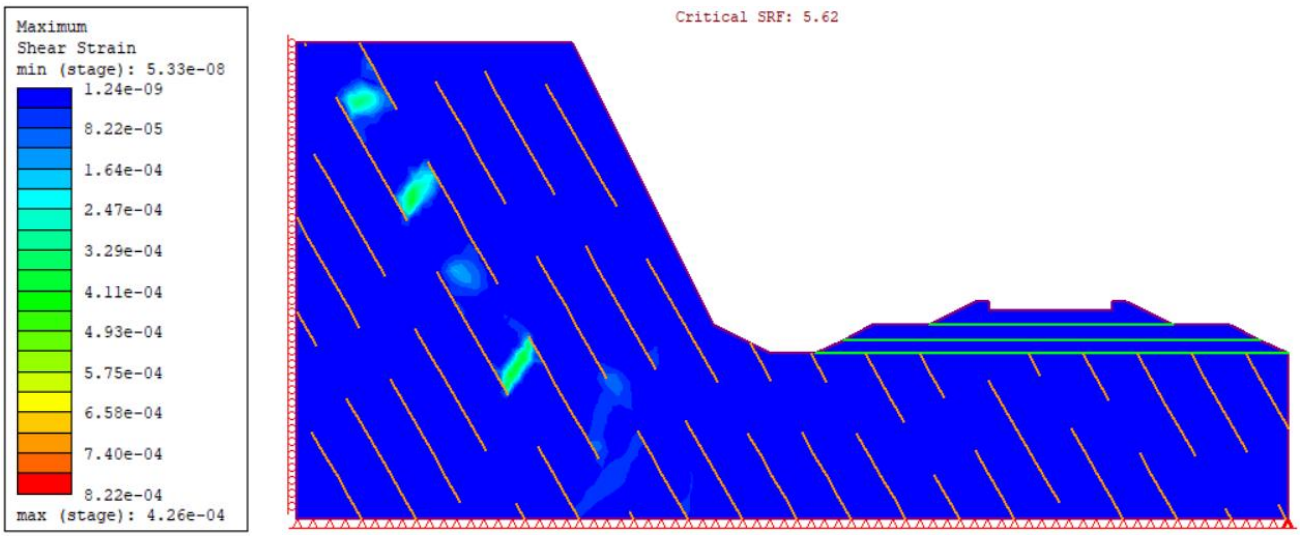

Figure 4.4 (d) Simulation result for Subgroup 16 model: slope ratio = 1H:2V, h = 6 m, θ = 60°, s = 1 m, p = 0.7, l = 3 m.

The maximum shear strain of the model tends to happen at and between joints, as seen in Figures 4.3 and 4.4, which may indicate that the joints compromise the slope's stability. All FS results generated by the models examined with altered joint parameters are obtained by RS2. The slope safety factor changes in conjunction with changes to the joint parameters. Section 4.2 emphasizes the pattern of the influence of joint factors on model safety.

4.1.2 Set II – Jointed rock slope model under freight train load conditions

The Set II models are developed by incorporating freight train loads into the Set I models. All jointed rock and embankment model combinations for the seven research parameters, including loads produced by train operations, are summarized in Figure 4.5 for a total of 3,456 examples. The maximum safe travel speed is determined by accelerating the train from 0 to 120 km/h at an average speed of 8 km/h, where 16 trials are tested for each set of models. All the combined instances are listed in Appendix B, sorted into six groups with 12 subgroups each.

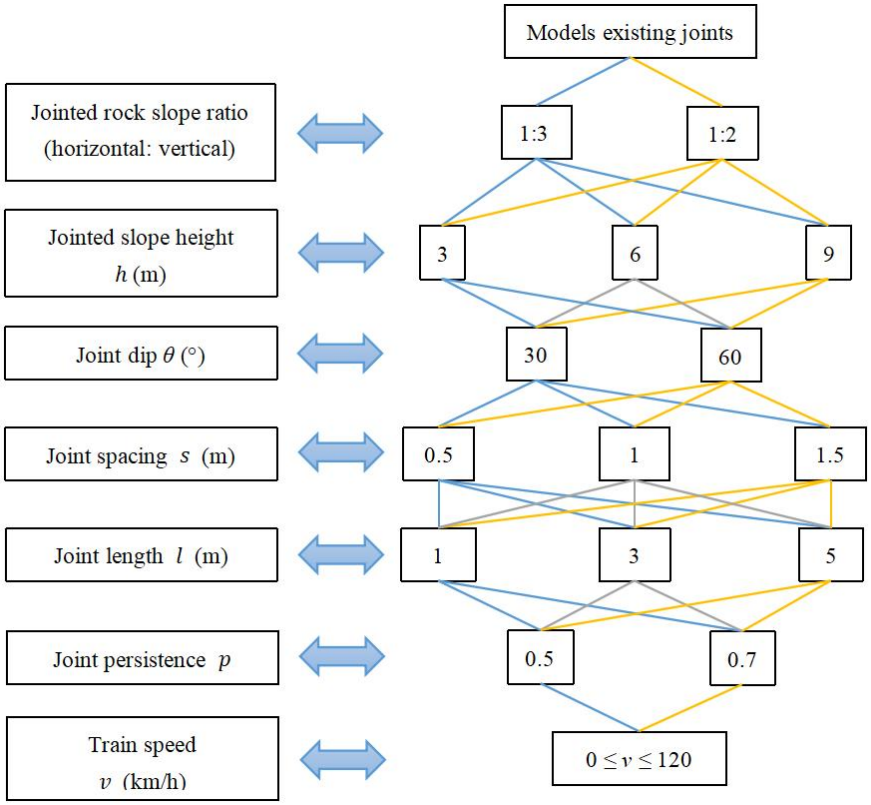

Figure 4.5 Diagram of various cases in Set II – Jointed rock slope model under moving train load conditions.

Figure 4.6 depicts the calculation process for determining the maximum safe train speed. All train speeds necessary for this process are converted into the equivalent forces applied to the embankment surface at the base of the sleeper. The train accelerates from a standstill in 8 km/h steps until a speed that would invalidate the slope is recognized. The speed acceleration can capture the yielding developing trend, resulting in failure extending from the embankment to the bedrock. Section 2.4.5 states that the minimum safety factor required to make a railroad embankment safe and effective is 1.3. When the train speed reaches the point where failure is detectable, the speed is reduced by 8 km/h. If the lowered speed is less than 120 km/h, this is regarded as the highest train operation speed

that this embankment can withstand; otherwise, 120 km/h is considered the maximum safe speed of the railway. Furthermore, in some models, the embankment is unable to resist a stationary train load, meaning that the model's FS is less than 1.3 when the train speed is 0. In this instance, it can be presumed that the model has no maximum operating speed.

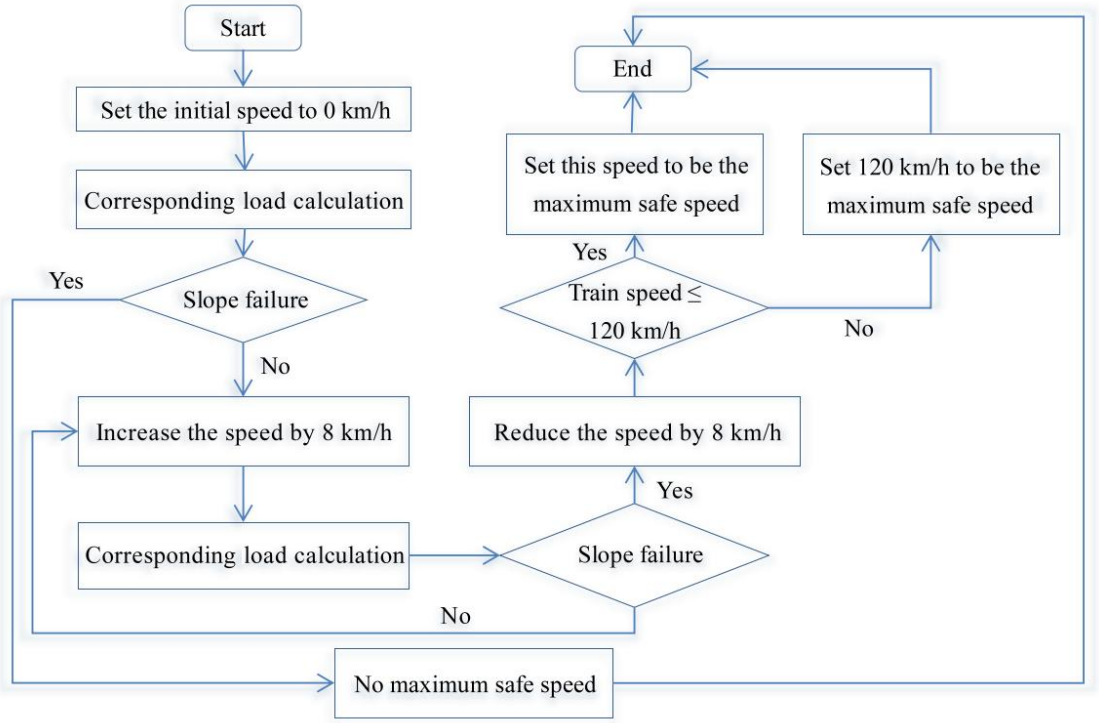

Figure 4.6 Flowchart for calculating the maximum safe freight train speed.

The model with a joint length of 5 m in Subgroup 77 is used as an example to visualize the influence of train loads on the jointed rock slope model. The analytical result is given in Figure 4.7, with an FS of 2.86. At this point, there is no rail speed on the embankment.

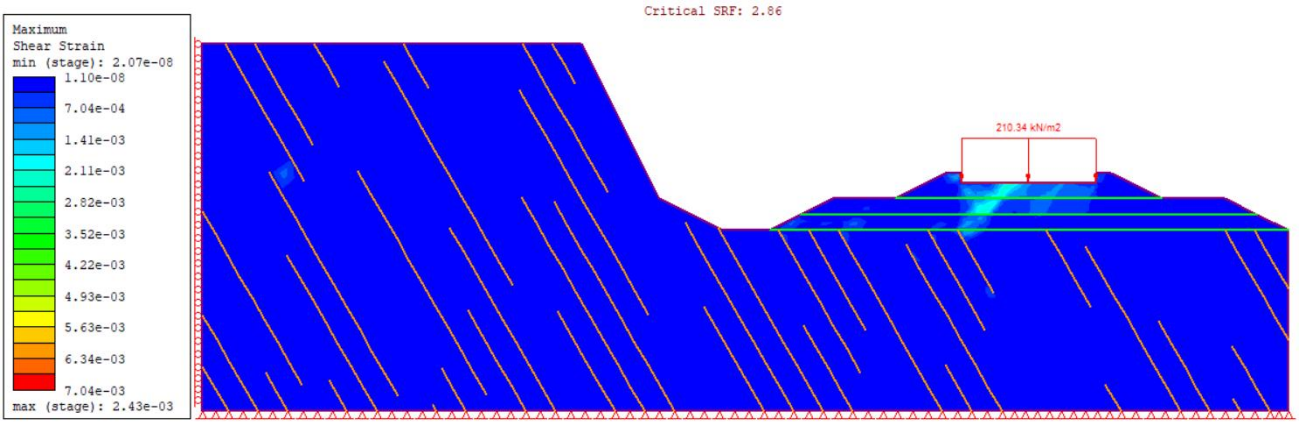

Figure 4.7 Simulation result for Subgroup 77 model: slope ratio = 1H:2V, h = 3 m, θ = 60°, s = 0.5 m, p = 0.5, l = 5 m.

By altering the model's research parameters one at a time in the stationary train scenario, the model depicted in Figure 4.7 is utilized as a control group for monitoring changes in FS. The maximum shear strain contours of the corresponding model following parameter modifications are shown in Figures 4.8 (a)–(f). The side slope of the model in Figure 4.8 (a) from Subgroup 113 is increased

from 1H:2V to 1H:3V. The model where Figure 4.8 (b) is located (in Subgroup 89) raised the slope height by 3 m. The result of the FS is shown in Figure 4.8 (c) for Subgroup 83, where the joint set's direction is modified from 60° to 30°. Figure 4.8 (d) depicts the model results for Subgroup 73 after adjusting the joint spacing from 0.5 m to 1.5 m. The simulation results of reducing the joint length in Subgroup 77 to 3 m are displayed in Figure 4.8 (e). Figure 4.8 (f) depicts the model (in Subgroup78) created by raising the jointed persistence from 0.5 to 0.7 in the model of Figure 4.7 while lowering the FS to 1.79.

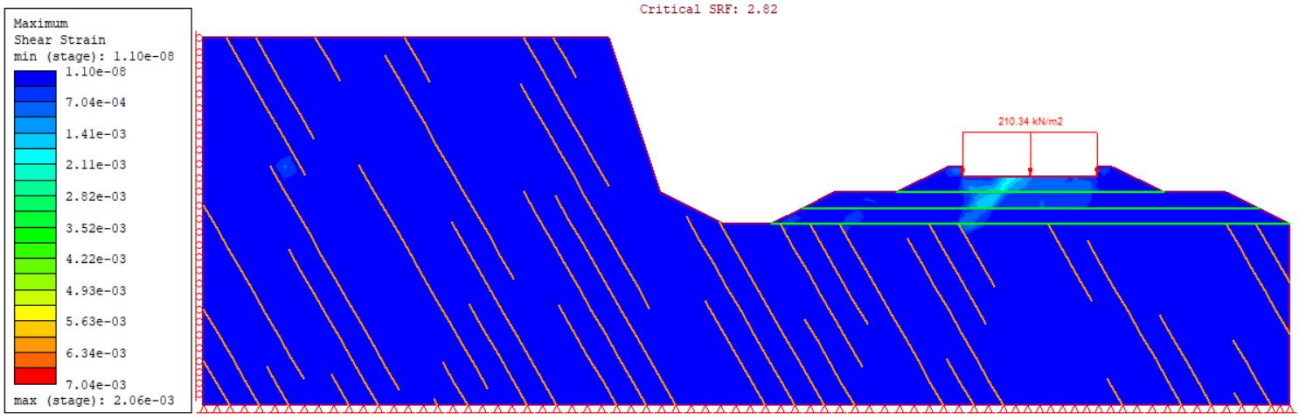

Figure 4.8 (a) Result for Subgroup 113 model: slope ratio = 1H:3V, h = 3 m, θ = 60°, s = 0.5 m, p = 0.5, l = 5 m.

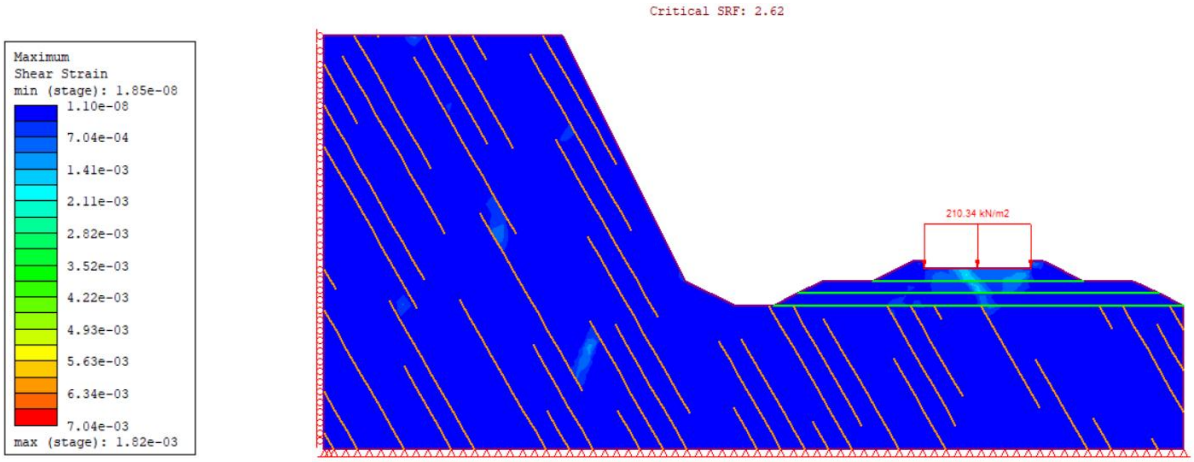

Figure 4.8 (b) Result for Subgroup 89 model: slope ratio = 1H:2V, h = 6 m, θ = 60°, s = 0.5 m, p = 0.5, l = 5 m.

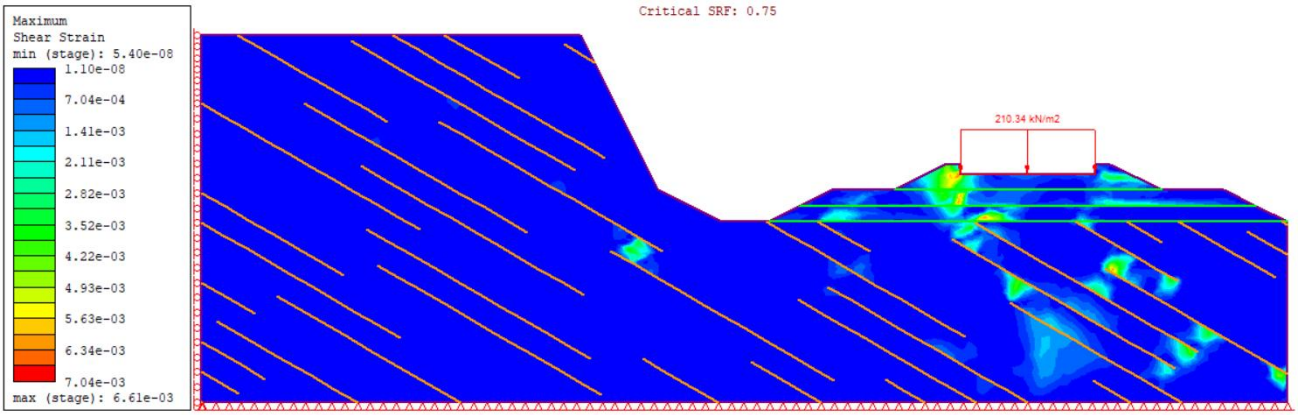

Figure 4.8 (c) Result for Subgroup 83 model: slope ratio = 1H:2V, h = 3 m, θ = 30°, s = 0.5 m, p = 0.5, l = 5 m.

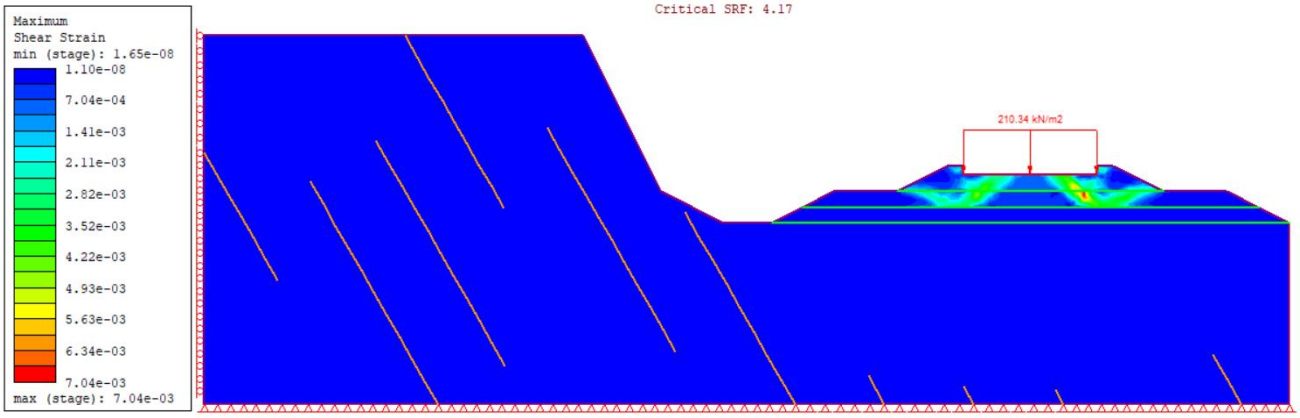

Figure 4.8 (d) Result for Subgroup 73 model: slope ratio = 1H:2V, h = 3 m, θ = 60°, s = 1.5 m, p = 0.5, l = 5 m.

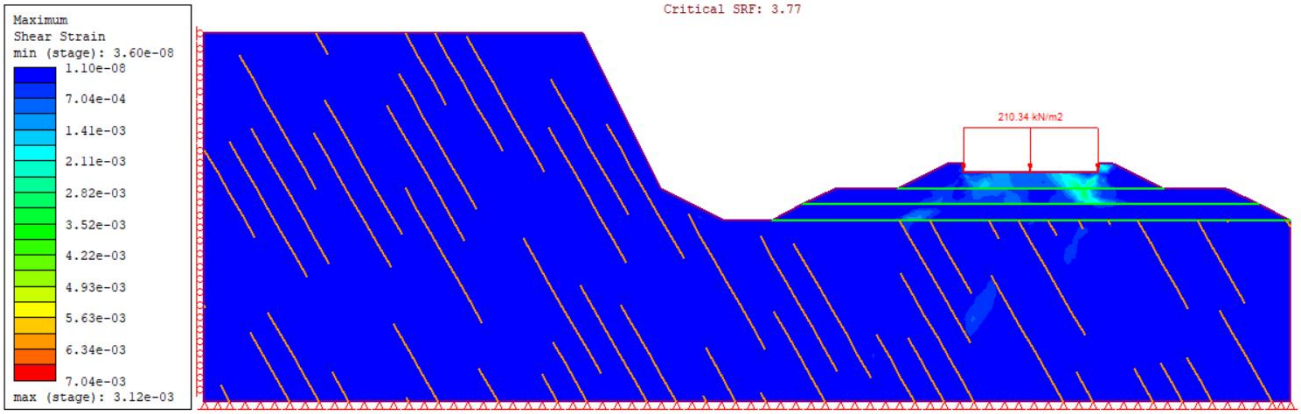

Figure 4.8 (e) Result for Subgroup 77 model: slope ratio = 1H:2V, h = 3 m, θ = 60°, s = 0.5 m, p = 0.5, l = 3 m.

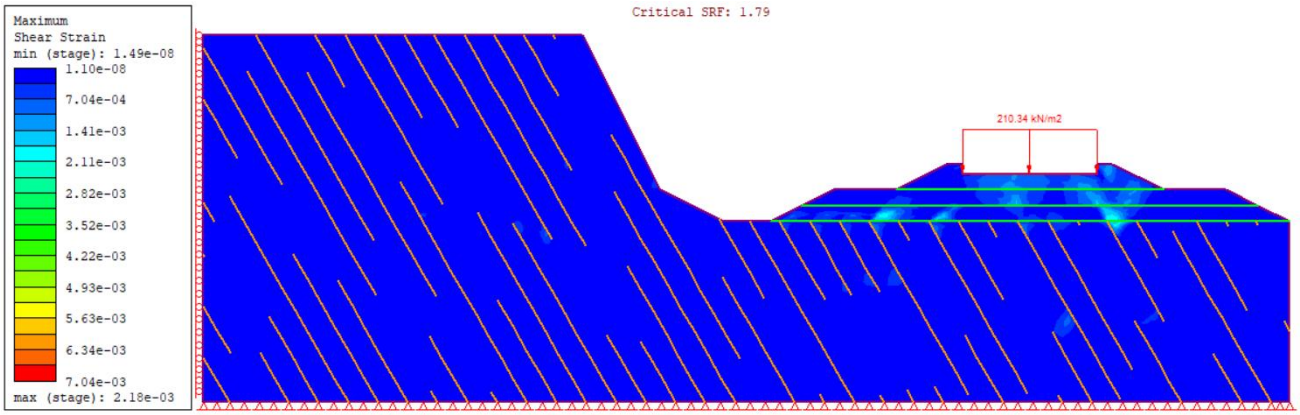

Figure 4.8 (f) Result for Subgroup 78 model: slope ratio = 1H:2V, h = 3 m, θ = 60°, s = 0.5 m, p = 0.7, l = 5 m.

The simulation outcomes from RS2 demonstrate that applying train loads to the outside of the model reduces its FS value. Furthermore, Figure 4.8 demonstrates that, in contrast to the damage mechanism of the model in Set I, the damage mechanism of the model where train loads are included concentrates on the bearing capacity of the embankment being damaged. Comparing Figures 4.7 and 4.8 reveals that the model's stability can be affected by changes in the joint's side slope, direction, spacing, length, or coherence. Notably, failure in Figure 4.8 (d) only affects the

embankment and is unable to reach the jointed rock segment. The increased joint spacing increases the stability of the joint rock slope, and the natural ground is considerably safer than the load-bearing embankment due to this joint set. The model's strength depends on the embankment's characteristics, such as its geometry and material, since the model's FS is not significantly impacted by the joint set. Each model has a FS ranging from 4.12 to 4.27, which is generally higher than the FS for a model with joint damage.

There is no maximum safe operating speed when the simulation results are less than 1.3, and the train is therefore deemed unable to halt or traverse the mountainous area safely. The maximum safe driving speeds that are permitted for each model in Set II are listed in Appendix C. If the maximum safe transportation speed is zero, this indicates that a freight train can safely remain stopped on the track. When the maximum safe speed is between 0 and 120 km/h, the freight train can safely travel on the track without exceeding the maximum safe speed. Section 4.3 details the FS changing trends for Set II models that are compromised by the loads produced are stated when the train moves at its maximum safe speed.

4.2 Parametric study of Set I models

Figure 4.1 depicts the investigated parameters in the Set I model. The impacts of each of the six research parameters on the FS are studied using a graphical approach in this section. The results of FS, coupled with the rate of change, are mentioned in the graphical analysis to illustrate the FS trend. Equation 4.1 can be used to compute R_{FS}, the rate of change in FS. The *Sg* mentioned in the legend of the line graph is an abbreviation for a subgroup. This acronym is used to designate the related subgroups in later analysis.

$$R_{FS} = \frac{FS_m - FS_n}{FS_n} \tag{4.1}$$

where FS_n denotes the safety factor of the model in the control group, and FS_m is the model's safety factor after a parameter modification.

Tables 4.1–4.6 summarize the outcomes of FS in Groups 1–6, where the joint length is 1 m for all Set I models.

Table 4.1 FS results of Set I models in Group 1 with *l* of 1 m.

	Sg 1	**Sg 2**	**Sg 3**	**Sg 4**	**Sg 5**	**Sg 6**	**Sg 7**	**Sg 8**	**Sg 9**	**Sg 10**	**Sg 11**	**Sg 12**
FS	12.98	12.08	11.36	10.51	9.53	7.88	12.82	11.51	10.71	9.38	7.49	6.13

Table 4.2 FS results of Set I models in Group 2 with *l* of 1 m.

	Sg 13	**Sg 14**	**Sg 15**	**Sg 16**	**Sg 17**	**Sg 18**	**Sg 19**	**Sg 20**	**Sg 21**	**Sg 22**	**Sg 23**	**Sg 24**
FS	10.32	9.65	9.32	8.31	7.71	6.57	9.74	8.92	9.06	7.62	5.7	4.89

Table 4.3 FS results of Set I models in Group 3 with *l* of 1 m.

	Sg 25	**Sg 26**	**Sg 27**	**Sg 28**	**Sg 29**	**Sg 30**	**Sg 31**	**Sg 32**	**Sg 33**	**Sg 34**	**Sg 35**	**Sg 36**
FS	8.61	8.57	8.29	7.73	6.69	6.29	7.91	7.5	7.28	6.36	4.61	4.09

Table 4.4 FS results of Set I models in Group 4 with *l* of 1 m.

	Sg 37	**Sg 38**	**Sg 39**	**Sg 40**	**Sg 41**	**Sg 42**	**Sg 43**	**Sg 44**	**Sg 45**	**Sg 46**	**Sg 47**	**Sg 48**
FS	12.96	12.04	11.25	10.42	9.37	7.82	12.77	11.41	10.67	9.3	7.38	5.98

Table 4.5 FS results of Set I models in Group 5 with *l* of 1 m.

	Sg 49	**Sg 50**	**Sg 51**	**Sg 52**	**Sg 53**	**Sg 54**	**Sg 55**	**Sg 56**	**Sg 57**	**Sg 58**	**Sg 59**	**Sg 60**
FS	10.08	9.5	9.23	8.14	7.48	6.47	9.53	8.77	8.81	7.42	5.33	4.67

Table 4.6 FS results of Set I models in Group 6 with *l* of 1 m.

	Sg 61	**Sg 62**	**Sg 63**	**Sg 64**	**Sg 65**	**Sg 66**	**Sg 67**	**Sg 68**	**Sg 69**	**Sg 70**	**Sg 71**	**Sg 72**
FS	8.39	7.87	7.77	6.9	5.81	5.43	7.73	7.07	6.87	5.96	4.45	3.93

(a) Jointed rock slope ratio

Figure 4.9 depicts the link between the rate of change of FS due to increased slope ratios and the length of the joints. It is clear that steep, jointed rock slopes significantly reduce side slope stability.

With a rock slope height of 3 m and a joint direction of 60°, Figure 4.9 (a) visualizes the corresponding FS change trends caused by raising the slope of jointed rock from 1H:2V to 1H:3V for various joint lengths, spacing, and persistence for all models.

For the equivalent model shown in Figure 4.9 (a), the models in trend graphs 4.9 (c) and (e) show the rate of FS change when increasing the height of the rock slope to 6 m and 9 m, respectively. The lowering of the joint orientation for the models found in Figures 4.9 (a), (c), and (e) from 60° to 30° is the trend seen in Figures 4.9 (b), (d), and (f).

The overall trend in Figure 4.9 demonstrates a drop in FS as the jointed rock slope steepens. Regardless of the joint length, when the joint orientation is at 30°, the decline in model security is more visibly reflected by the rock slope. As the joint length increases, the gradient of the side slopes increases, causing a significant loss in FS when the rock slope height is 3 m. The rise in slope rate with the increase in joint length only results in a modest change in FS when the rock slope is extended to 6 or even 9 m as the value of FS has reached around 1.

(b) Jointed rock slope height

For models with the same joint spacing (1.5m) and persistence (0.5), Figures 4.10 (a) and (b) present the changing trend of FS among subgroups under the three jointed rock slope heights when the slope is 1H:2V and 1H:3V.

For parallel comparisons, joint orientations of 30° and 60°, as well as all joint lengths (1, 3, and 5 m), are mentioned in Figure 4.10. It should be emphasized that all FS rates of change in the figures are determined by comparing the same conditions with a slope height of 3 m.

When the rock slope height rises from 3 m to 6 m, there is a considerable reduction in FS. The rate of

FS decline reduces as the rock slope height continues to rise to 9 m. When the slope ratio is 1H:3V and the slope height reaches 9 m, irrespective of the joint direction, the degree of FS reduction tends to zero for the 3 m and 5 m joint models with a spacing of 1.5 m and persistence of 0.5.

Figures 4.10 (c)–(f) show the outcomes of setting the joint spacing for the models in Figures 4.10 (a) and (b) to 1 m and 0.5 m, respectively. As demonstrated, the FS trend for an increase in rock slope height is essentially unchanged when the joint spacing is decreased. The FS drops from approximately 25% to approximately 50%. In particular, the FS changes up to more than 60% when the slope height is extended to 9 m for the model in Figure 4.10 (f) with a slope ratio of 1H:3V, joint orientation of 30°, and spacing of 0.5 m.

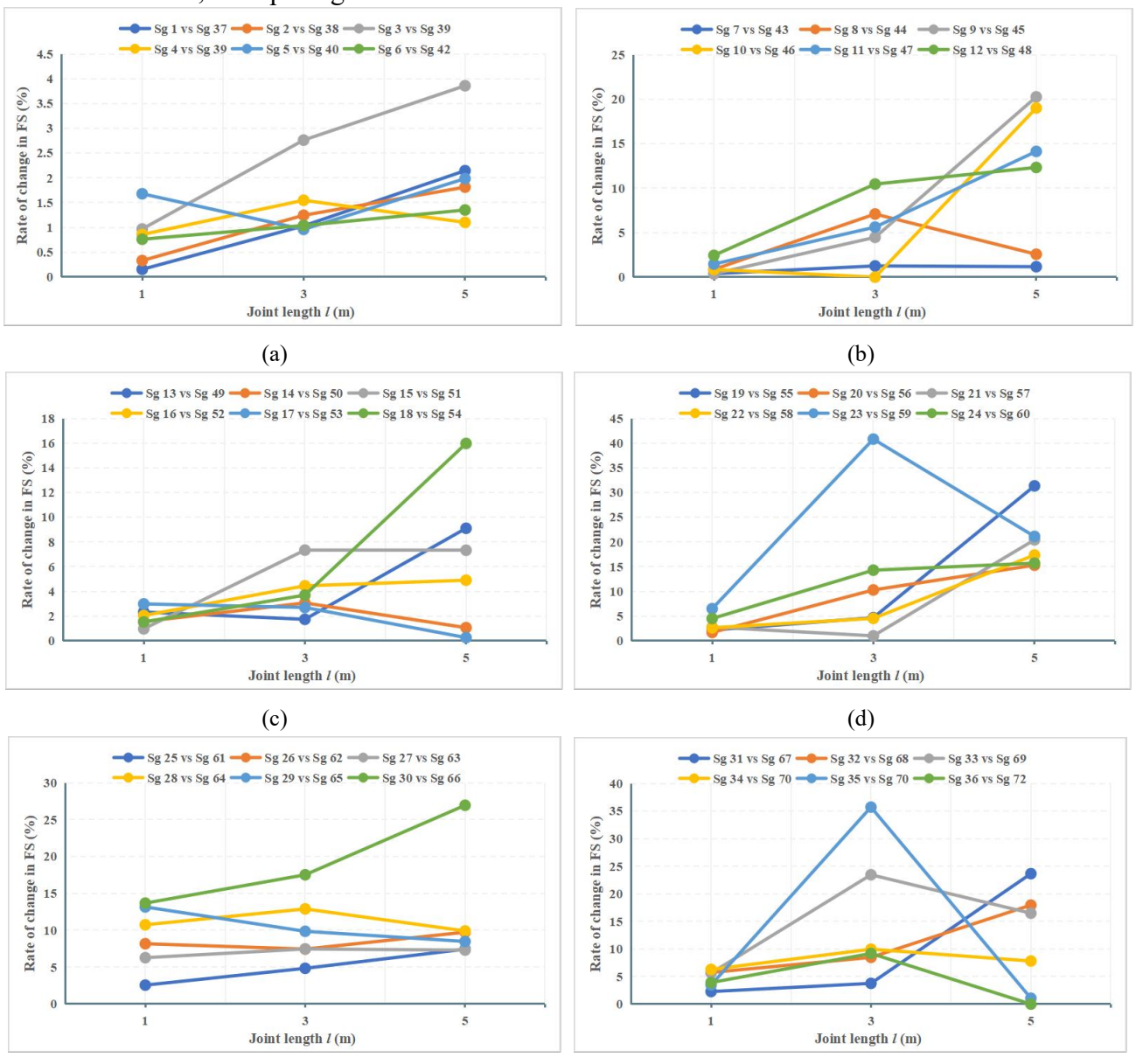

Figure 4.9 Relationship between the rate of FS change due to slope elevation and the joint length:
(a) Set I models with h of 3 m, θ of 60°; (b) Set I models with h of 3 m, θ of 30°; (c) Set I models with h of 6 m, θ of 60°; (d) Set I models with h of 6 m, θ of 30°; (e) Set I models with h of 9 m, θ of 60°; (f) Set I models with h of 9 m, θ of 30°.

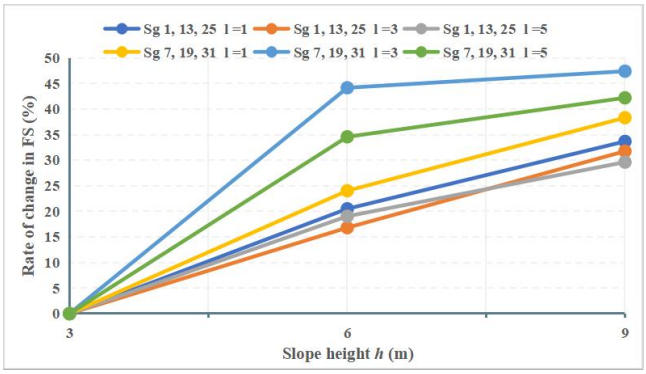

(a)

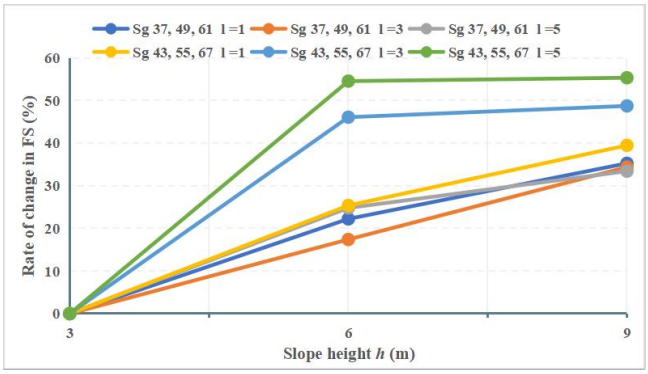

(b)

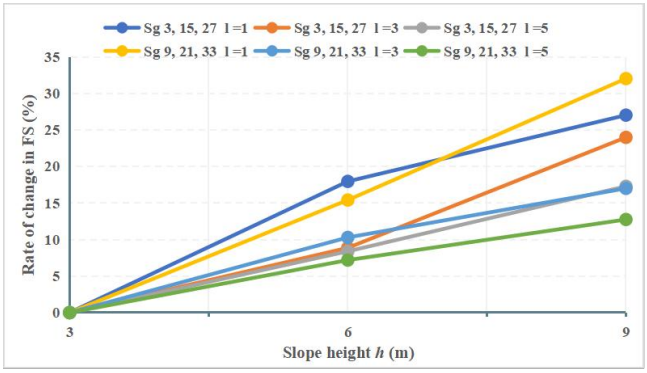

(c)

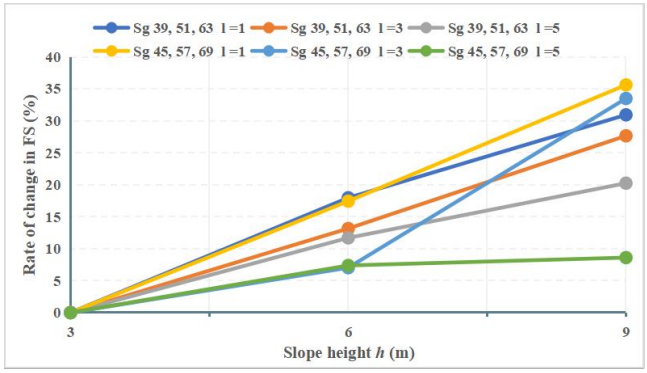

(d)

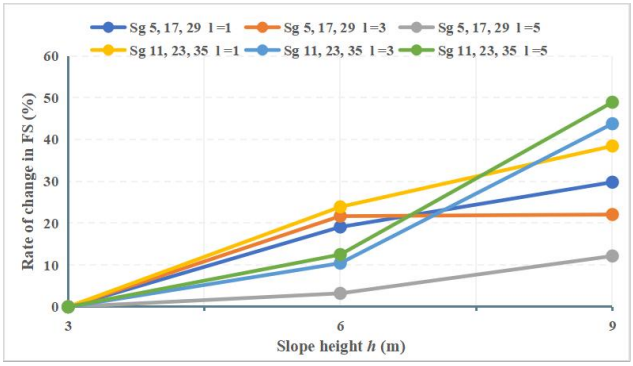

(e)

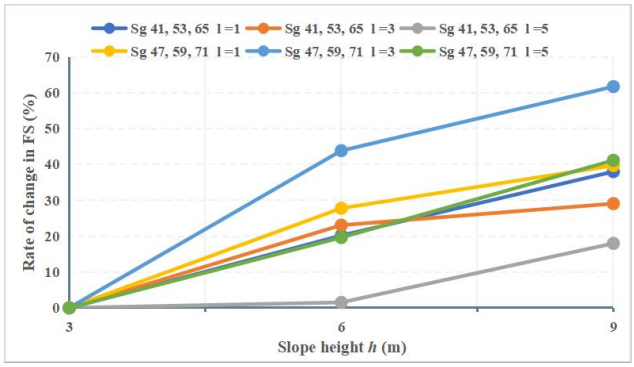

(f)

Figure 4.10 Relationship between the rate of FS change in Set I models and the slope height:
(a) Models with slope ratio of 1H:2V, *s* of 1.5 m, *p* of 0.5; (b) Models with slope ratio of 1H:3V, *s* of 1.5 m, *p* of 0.5;
(c) Models with slope ratio of 1H:2V, *s* of 1 m, *p* of 0.5; (d) Models with slope ratio of 1H:3V, *s* of 1 m, *p* of 0.5;
(e) Models with slope ratio of 1H:2V, *s* of 0.5 m, *p* of 0.5; (f) Models with slope ratio of 1H:3V, *s* of 0.5 m, *p* of 0.5.

The examination of the two factors mentioned above reveals that increasing jointed rock slopes leads to slope instability and that the stability of the entire structure can be improved by flattening the slope.

(c) Joint orientation

Two angles, 30° and 60°, are present in the joint direction in this research. A total of 24 subgroups

are chosen to test the effect of different joint dips on the model's safety performance. In this part, models with joint persistence of 0.7, all side slope ratios (1H:2V and 1H:3V), and jointed rock slope heights (3, 6, and 9 m) are chosen for the investigation. Figures 4.11 (a) and (b) depict the corresponding downward FS change trends with increasing joint length, for joint spacings of 1 m and 0.5 m, respectively.

Figure 4.11 shows that the tendency for FS change brought on by different joint directions is significant. Due to the alteration in joint direction, the FS change rate stays within 20%, while the joint length is 1 m. When the joint length in the model reaches 5 m, the reduction of joint orientation from 60° to 30° lowers the slope's FS by 40%–50% or even more. When the joint length is 3 m, the joint spacing is 1 m, and the slope ratio is 1H:2V, the FS changes by around 25% with a reduction in the joint angle; once the joint spacing and the slope are dropped, the FS reduces by about twice as much as the initial value. In summary, for most models, slope stability will be significantly impacted by the change in joint direction.

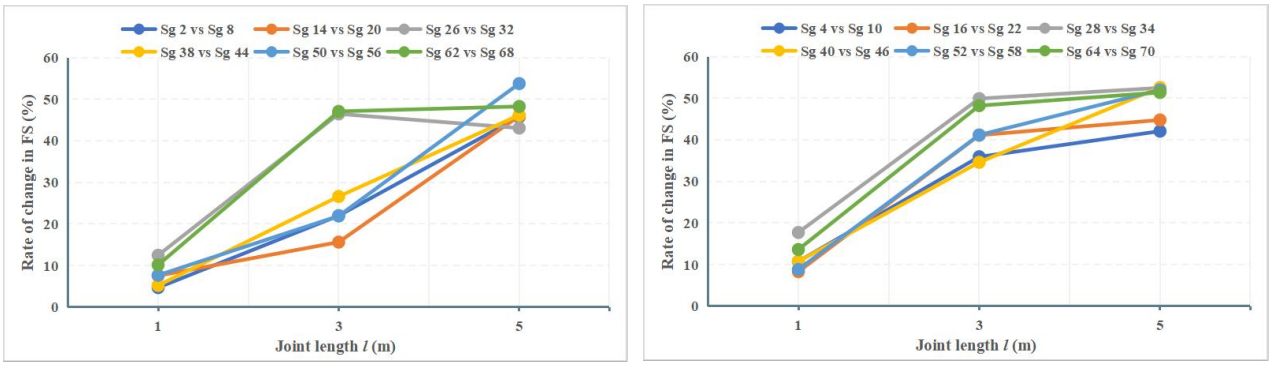

(a) (b)

Figure 4.11 Relationship between the rate of FS change due to joint direction change and the joint length: (a) Set I models with *s* of 1.5 m, *p* of 0.7; (b) Set I models with *s* of 1 m, *p* of 0.7.

(d) Joint spacing

For models in subgroups 14, 16, and 18 of Group 2 and subgroups 50, 52, and 54 of Group 5, Figure 4.12 (a) shows the magnitude of change in FS for various joint spaces. The side slope ratios in the first three subgroups are modeled at 1H:2V, whereas in the last three subgroups, the slopes are increased to 1H:3V. Except for the difference in joint spacing, all models indicated in these six subgroups have the same slope height (6 m), joint angle (60°), and joint persistence (0.7).

Joint spacing starts at 1.5 m in subgroups 14 and 50 and decreases by 0.5 m in subgroups 16 and 52 until it reaches 0.5 m in subgroups 18 and 54. As demonstrated in Figure 4.12 (a), the slope stability reduces as the joint separation is decreased. The rate of change of FS accelerates with a decrease in joint spacing.

All of the analytical models mentioned above have a joint direction of 60°. The corresponding subgroups 20, 22, and 24 as well as subgroups 68, 70, and 72 of the same groups are chosen to confirm the impact of joint spacing on the model FS values when the joint direction is changed. These six subgroups are compared to the models mentioned above by reducing the joint dip to 30°

while keeping all other parameters fixed. Figure 4.12 (b) shows the obtained rate of change of FS concerning joint spacing. The FS change pattern can be found to be roughly consistent with the analytical findings from the previous part. In this case, the model with a 30° joint orientation is affected more significantly by the reduction in joint spacing. When the joint space is 0.5 m, the FS change rate typically exceeds 50%.

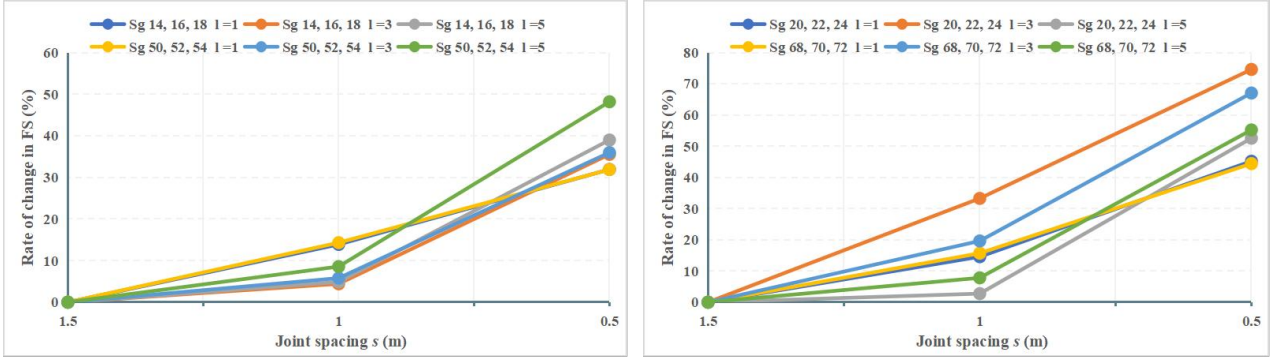

(a) (b)

Figure 4.12 Relationship between the rate of FS change in Set I models and the joint spacing: (a) Models with h of 6 m, θ of 60°, p of 0.7; (b) Models with h of 6 m, θ of 30°, p of 0.7.

(e) Joint persistence

In this study, two types of joints are chosen based on their relative persistence degrees, which are 0.5 and 0.7. When the persistence degree reaches 0.7, it implies that the adjacent joints have become relatively continuous with each other. Theoretically, the slope becomes increasingly unstable as the joint persistence degree grows.

A study of the trend of FS change due to the change in joint persistence is conducted using two subgroups as comparisons in each group. Models from subgroups 1, 13, and 25 correspond to slope heights of 3, 6, and 9 m, respectively, which all feature 1H:2V slope ratios, joints with 1.5 m spacing, 60° orientation, and 0.5 persistence. By increasing the joint persistence of these three groups of models to those in subgroups 2, 14, and 26, the rate of change in FS is visualized in Figure 4.13 (a).

When the slope is increased to 1H:3V, the models corresponding to the six subgroups indicated above are found in Groups 4–6, and the FS results are demonstrated to be less than those obtained from Groups 1–3.

Keeping the remaining parameters of the model above constant with the exception of the joint direction being modified to 30°, Figure 4.13 (b) displays the results of each matching subgroup in Groups 1–6 caused by an increase in joint persistence.

According to Figure 4.13, the joint persistence increases with a joint spacing of 1.5 m and length of 1 m, which has an impact on the model's FS within a 10% range. The FS of the model falls by around 25% as the joint length increases to 5 m. The FS of the model falls by around 25% as the joint length increases to 5 m. Generally, for models with a joint orientation of 30°, the increase in joint persistence leads to a higher reduction in FS, notably in models with a joint length of 3 m, where

most FS reductions reach as high as 50%.

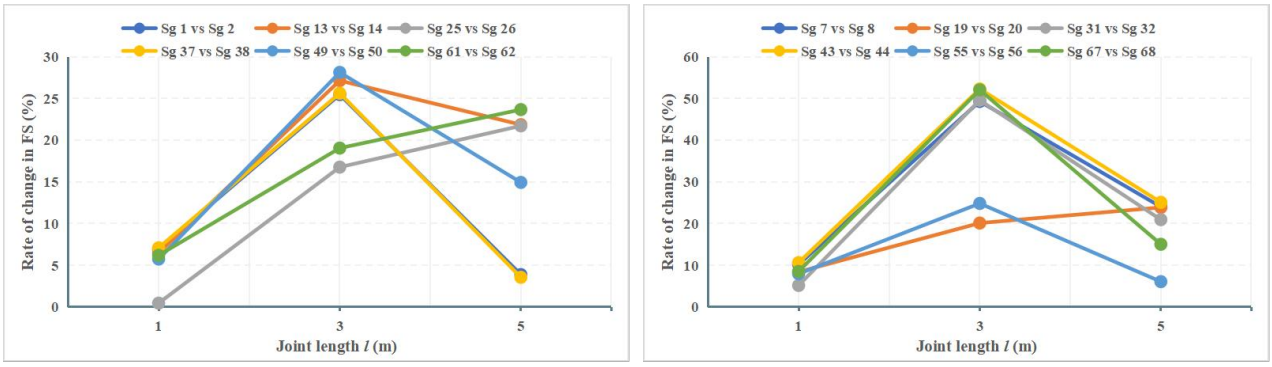

(a) (b)

Figure 4.13 Relationship between the rate of FS change due to increasing the joint persistence and the joint length: (a) Set I models with s of 1.5 m, θ of 60°; (b) Set I models with s of 1.5 m, θ of 30°.

(f) Joint length

The FS values tend to decline as the joint length rises from the RS2 outcomes. Group I is chosen to be representative, where the numerical disparities in the FS results are more significant, making it simpler to spot patterns. Each model in Group I has a slope height of 3 m and a side slope ratio of 1H:2V. The rates of change for subgroups 1–6, which have a 60° joint orientation, are compiled in Figure 4.14 (a).

Figure 4.14 (b) traces the rates of change in FS versus joint length for subgroups 7 through 12, which were modeled for the counterparts with only the joint orientation altered to 30°. The joint spacing varies among the subgroups: 1.5 m in subgroups 1, 2, 7, and 8; 1 m in subgroups 3, 4, 9, and 10; and 0.5 m in the remaining subgroups. Joint persistence is used to identify the models in subgroups with the same joint spacing.

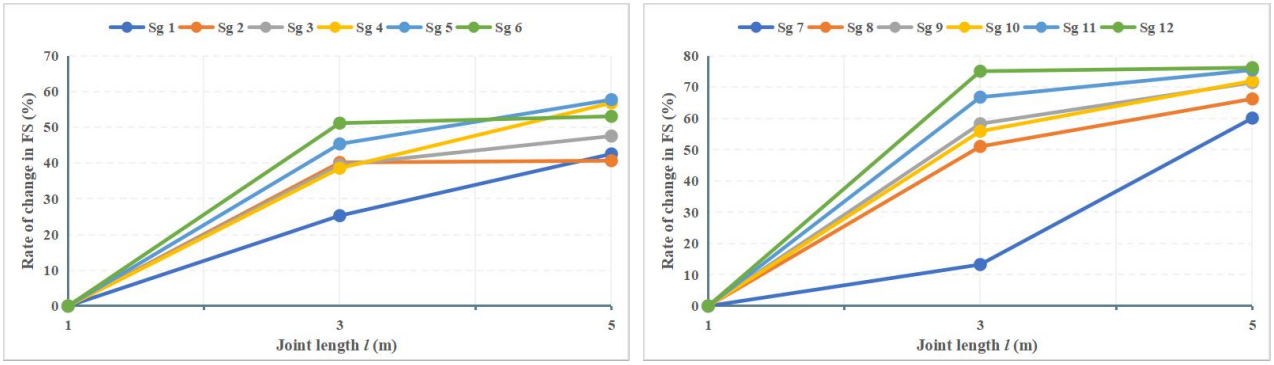

(a) (b)

Figure 4.14 Relationship between the rate of FS change in Set I models and the joint length: (a) Models with slope ratio of 1H:2V, h of 3 m, θ of 60°; (b) Models with slope ratio of 1H:2V, h of 3 m, θ of 30°.

Figure 4.14 (a) depicts that the FS rate of change program has a negative growth state, indicating that a rise in joint length reduces slope stability. When the joints increase from 1 m to 3 m, FS drops by roughly 25%–50%; the smaller the joint spacing, the larger the decrease in FS. The increase in joint length to 3 m can effectively drop the FS by more than 50% when the joint orientation is reduced to

30°, and there is a negative correlation between the FS decrease and the joint spacing. Regardless of the joint direction and spacing, the model's FS changes relatively little when the joint length increases to 5 m compared to the FS of the corresponding 3 m joint length model.

In conclusion, the model's slope stability can be significantly impacted by the rock slope's height and the direction, spacing, length, and persistence of the joints. Changes in the slope ratio result in relatively minor adjustments to the FS of the slope.

4.3 Results discussion of Set II models

Models for Set II are created by modifying each Set I model with various freight train loads. Slope geometry and joint characteristics are examined in Section 4.3.1 concerning the FS of Set II models. Section 4.3.2 outlines the maximum safe transit speed tolerance in the Set II models.

4.3.1 Influence of slope geometry and joints for Set II models under a stationary train

According to the examination of the Set I model, every parameter—aside from the gradient of the rock slope—has a significant impact on the model's stability. The specific consequences of each characteristic are examined separately.

Tables 4.7–4.12 conclude the FS results of Set II models with the joint length of 1 m, where the model failure affected the embankment is inaccessible to the jointed rock part.

Table 4.7 FS results of Set II models in Group 7 with *l* of 1 m.

	Sg 73	**Sg 74**	**Sg 75**	**Sg 76**	**Sg 77**	**Sg 78**	**Sg 79**	**Sg 80**	**Sg 81**	**Sg 82**	**Sg 83**
FS	4.18*	4.17*	4.15*	4.16*	4.19*	4.15*	4.13*	4.13*	4.12*	4.13*	4.17*

Table 4.8 FS results of Set II models in Group 8 with *l* of 1 m.

	Sg 85	**Sg 86**	**Sg 87**	**Sg 88**	**Sg 89**	**Sg 90**	**Sg 91**	**Sg 92**	**Sg 93**	**Sg 94**	**Sg 95**
FS	4.17*	4.21*	4.22*	4.22*	4.23*	4.15*	4.19*	4.18*	4.23*	4.21*	4.21*

Table 4.9 FS results of Set II models in Group 9 with *l* of 1 m.

	Sg 97	**Sg 98**	**Sg 99**	**Sg 100**	**Sg 101**	**Sg 102**	**Sg 103**	**Sg 104**	**Sg 105**	**Sg 106**	**Sg 107**
FS	4.19*	4.21*	4.21*	4.22*	4.23*	4.26*	4.18*	4.21*	4.17*	4.19*	4.19*

Table 4.10 FS results of Set II models in Group 10 with *l* of 1 m.

	Sg 109	**Sg 110**	**Sg 111**	**Sg 112**	**Sg 113**	**Sg 114**	**Sg 115**	**Sg 116**	**Sg 117**	**Sg 118**	**Sg 119**
FS	4.18*	4.17*	4.16*	4.18*	4.19*	4.15*	4.14*	4.13*	4.12*	4.13*	4.17*

Table 4.11 FS results of Set II models in Group 11 with l of 1 m.

	Sg 121	**Sg 122**	**Sg 123**	**Sg 124**	**Sg 125**	**Sg 126**	**Sg 127**	**Sg 128**	**Sg 129**	**Sg 130**	**Sg 131**
FS	4.16*	4.22*	4.22*	4.22*	4.23*	4.20*	4.16*	4.18*	4.20*	4.20*	4.19*

Table 4.12 FS results of Set II models in Group 12 with *l* of 1 m.

	Sg 133	**Sg 134**	**Sg 135**	**Sg 136**	**Sg 137**	**Sg 138**	**Sg 139**	**Sg 140**	**Sg 141**	**Sg 142**	**Sg 143**
FS	4.19*	4.16*	4.19*	4.20*	4.20*	4.18*	4.20*	4.19*	4.19*	4.20*	4.26*

It should be noted that all of the FS values with the * suffix in the tables support that the model damage is contained within the embankment and is unable to penetrate the jointed rock layer. As a result, model damage will occur at the embankment rather than the jointed rock component after the train load is applied to the top of the embankment, where its safety performance is significantly worse than that of the jointed rock. In other words, unless a smaller FS is estimated when the safety of the jointed rock component is reduced to meet the safety of the embankment, the model results where the FS value is placed are determined by the shape and nature of the embankment, as well as the external load size.

(a) Jointed rock slope height

Subgroups 77 and 78 from Group 7 are chosen to investigate the effect of changes in rock side slope height on the safety of models with train loads, representing models with side slope ratios of 1H:2V, 3 m slope heights with 0.5 m joint spacing, 60° joint orientation, existing different persistence of 0.5 and 0.7. Subgroups 89 and 90, as well as subgroups 101 and 102, correspond to models with slope elevations of up to 6 m and 9 m, respectively. The resulting changing trends are depicted in Figure 4.15 (a).

More cases are chosen for study to strengthen the reliability of the findings. The six subgroups listed in Figure 4.15 (b) have the same slope heights (3, 6, and 9 m) and side slope ratio (1H:2V) as the subgroups in Figure 4.15 (a). The joint direction has been changed to 30° and joint spacing to 1 m, with the results presented in Figure 4.15 (b). The models in which all 12 of the aforementioned subgroups have their slope ratios increased from 1H:2V to 1H:3V are the models in which Figures 4.15 (c) and (d) are situated.

When the model's FS is dominated by the safety of the embankment, the FS values for the stationary train model fluctuate between 4.12 and 4.27. The FS values and rate of change for this type are not accounted for in the analysis curves since the drop in model FS is within 4%, which is an overly modest rate of change. Additionally, as the model damage is not attributable to the jointed rock component, the * suffix safety factors are not covered in this study.

Figure 4.15 shows that the stability of the embankment, which regulates model safety, prevents a major change in FS from being caused by a change in slope height at 1 m for the joint length. This suggests that the rocky component of the joints is overstrengthened and that a single set of joints at this value does not present a failure hazard to the model. Given that all of the rates of change of FS in Figure 4.15 are negative, it can be concluded that raising the slope height decreases slope stability.

When the slope height is raised to 6 m, the FS is typically only reduced by less than 10% for models with joints that are oriented at 60°, and the longer the joints, the greater the reduction; for models with joints that are oriented at 30°, the rate of FS reduction can increase to about 25%. Most FS

results for each subgroup drop substantially when the slope height is up to 9 m, with the maximum FS dropping by 50% compared to the 3 m slope model.

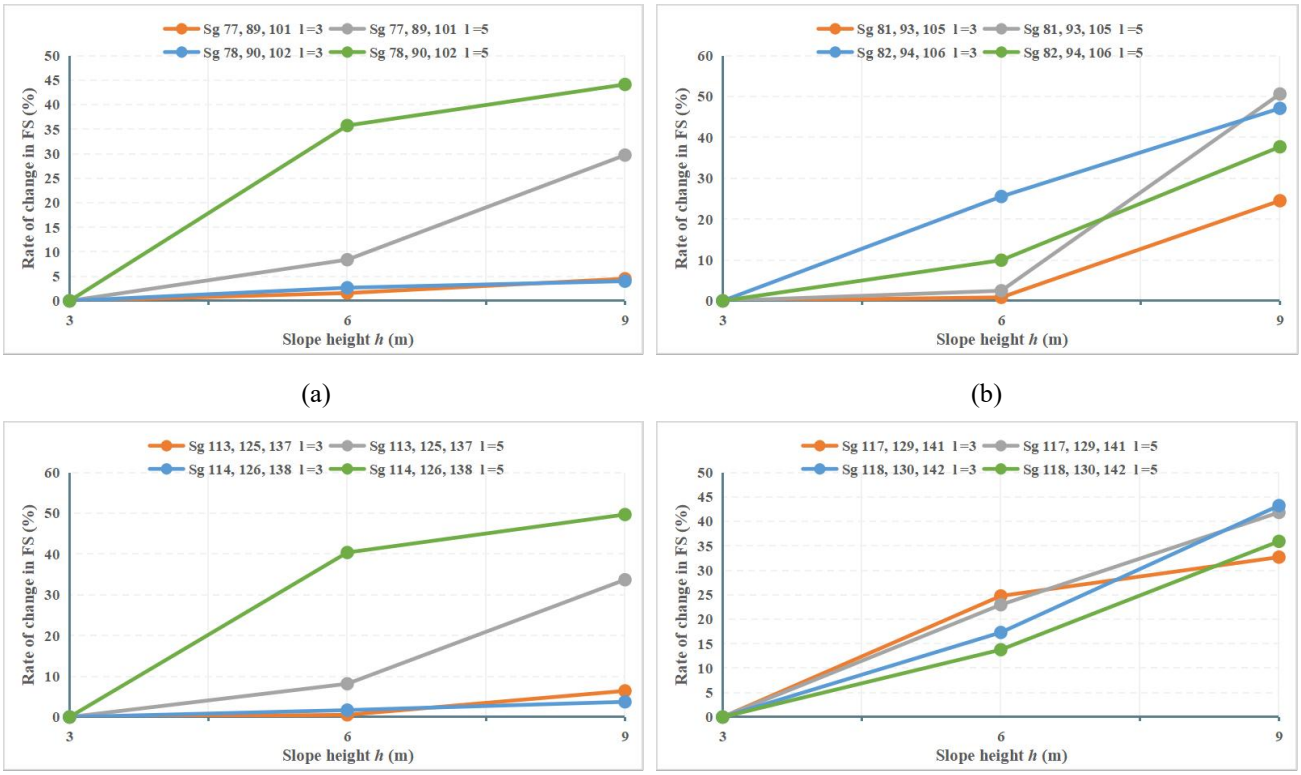

Figure 4.15 Relationship between the rate of FS change in Set II models and the slope height:
(a) Models with slope ratio of 1H:2V, *s* of 0.5 m, θ of 60°; (b) Models with slope ratio of 1H:2V, *s* of 1 m, θ of 30°;
(c) Models with slope ratio of 1H:3V, *s* of 0.5 m, θ of 60°; (d) Models with slope ratio of 1H:3V, *s* of 1 m, θ of 30°.

(b) Joint orientation

The change in joint direction substantially affects the evolution of FS, as stated in Section 4.2. The models developed in this study with train loads included produced polarizing outcomes.

With FS values around 4.2, the embankment section of the model explained in Section 4.3.1 (a) is the only place where one element of the model suffers damage. A portion of the model looks incapable of supporting the train loads, which means the FS value cannot functionally exist. The model lacks the strength to take on a halted train, and the track at that location is less competent to ensure a train's passage. Changing damage containing the train load could only be shown in a tiny fraction of the model results. The rate of change of FS following the lowering of the joint angle was compared using Group 7 (rock slope height of 3 m and slope ratio of 1H:2V), as reported in Table 4.13.

According to Table 4.13, the FS is decreased by around 20% when the joint length is 3 m and the joint orientation is changed from 60° to 30°; the predicted damage for a model with 1 m joint spacing extends from the embankment to the rocky area of the joint. When the joint length is between 3 and 5 m for the dense joint set model with a 0.5 m spacing, the FS values drop sharply and by as much as

60%–70%, reducing the joint dip to 30°.

Table 4.13 Rate of FS change due to joint direction change in Group 7.

Rate of change in FS	**FS**		
	Joint length l (m)		
	1	**3**	**5**
R_{FS} (%): Sg 75 vs Sg 81	-0.72	-16.43	-24.06
R_{FS} (%): Sg 76 vs Sg 82	-0.72	-21.29	-37.99
R_{FS} (%): Sg 77 vs Sg 83	-0.48	-62.86	-73.78
R_{FS} (%): Sg 78 vs Sg 84	-4.58	-66.72	-62.01

(c) Joint spacing

The 30° joint model was chosen for research since approximately half of the 60° joint model's slope safety is represented by embankment properties. Subgroups 79, 81, and 83 in Group 7 are models with joint persistence of 0.5 and spacing of 1.5 m, 1 m, and 0.5 m, respectively. Models for subgroups 80, 82, and 84 are produced when joint persistence is increased to 0.7. Figure 4.16 illustrates the FS reduction trends attained with decreasing joint spacing for joint lengths of 3 m and 9 m. For a joint length of 1 m, a change in joint spacing cannot significantly alter the model's FS, which is still mainly influenced by the characteristics of the embankment.

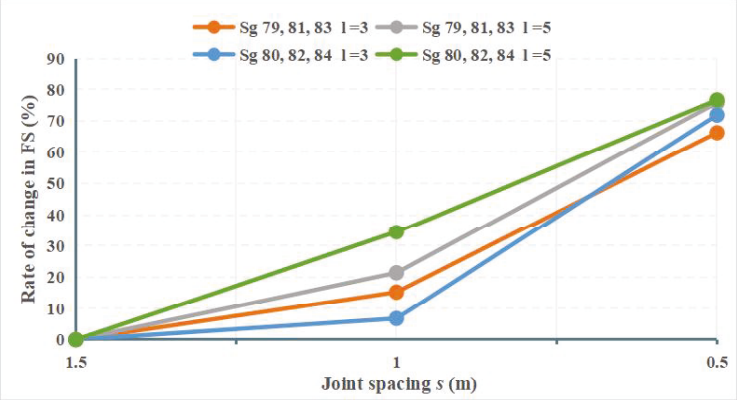

Figure 4.16 Relationship between the rate of FS change in Set II models and the joint spacing.

In the Group 7 model, the FS reduces to a lesser extent by approximately one third, when the joint spacing is reduced from 1.5 m to 1 m. When the distance is further decreased to 0.5 m, the FS drastically alters the value, with the decline rate reaching 70% or more. This trend is consistent with the outcomes from the Set I model. The joint spacing is a primary parameter that can influence slope stability.

(d) Joint persistence

The influence of joint persistence on the model's factor of safety is minimal at a joint length of 1 m, according to the RS2 outcomes. The change in FS reduction with increased joint persistence is investigated using models with joint lengths of 3 and 5 m. In each group of the Set II models, two pairs of subgroups are chosen for analysis.

Subgroups listed in Figure 4.17 (a) have joints spaced at 0.5 m, oriented at 60°, with a model slope shift from 1H:2V to 1H:3V and a slope height increase from 3 m to 9 m. The corresponding subgroups in Figure 4.17 (b) differ from those in Figure 4.17 (a) in that the joint spacing is increased to 1 m and the joint orientation is modified to 30°.

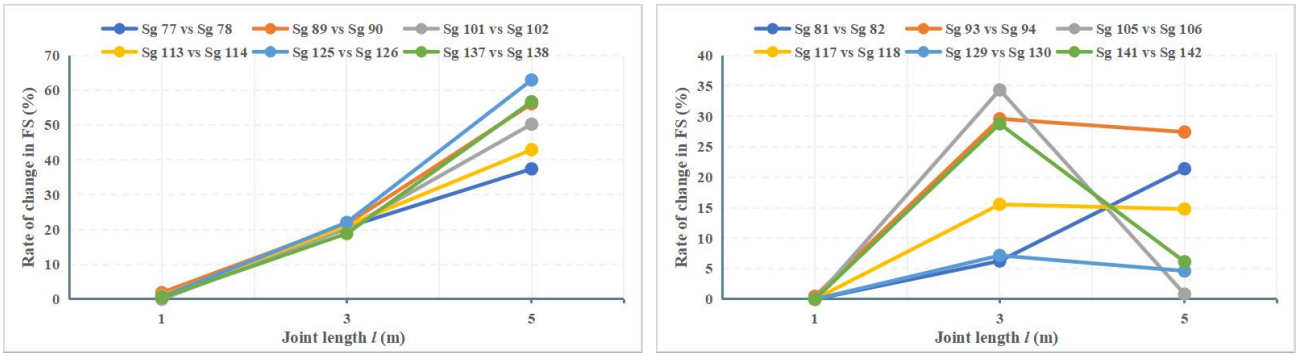

(a) (b)

Figure 4.17 Relationship between the rate of FS change due to increasing the joint persistence and the joint length: (a) Set II models with s of 0.5 m, θ of 60°; (b) Set II models with s of 1 m, θ of 30°.

Figures 4.17 (a) and (b) show the patterns associated with the length of the identified joints, which led to a reduction in FS as a result of an increase in persistence. It is clear that when the joint length is 3 m and the persistence varies from 0.5–0.7, the rate of FS decline typically stays within 30%. Furthermore, for the model with a 60° joint orientation and 0.5 m broad spacing, the most remarkable rise in joint persistence can result in a 60% drop rate in FS when the joint length is increased to 5 m.

In general, while other parameters remain constant, FS tends to decline as joint persistence rises. According to the results from selected subgroups in Figure 4.17, no value of FS is more than 3 when the joint length is 5 m, and FS tends to converge to 0 as the joint persistence rises.

(e) Joint length

The joint lengths of 3 and 5 m are employed for analysis since, in this study, the nature of the embankment substantially influences the FS of the model with a 1 m joint length.

When the joint length is increased from 1 m to 3 m, the regularity of the decreasing rate of FS is weak, with initial values all oscillating around 4.2. The comparison with the model with a 3 m joint length in the same subgroup is used to determine the rate of change of FS when it is raised to 5 m.

Figure 4.18 (a) obtains the results from the models in Group 7 with 30° joint direction, all of which have a 1H:2V side slope ratio and 3 m slope height. The change in FS with the joint length when the slope ratio of the model is elevated to 1H:3V are given in Figure 4.18 (b).

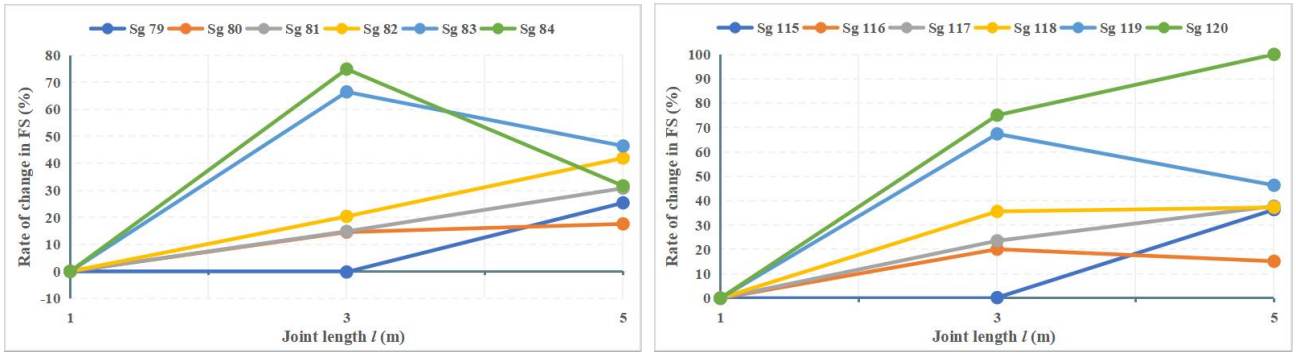

(a) (b)

Figure 4.18 Relationship between the rate of FS change in Set II models and the joint length:
(a) Models with slope ratio of 1H:2V, h of 3 m, θ of 30°; (b) Models with slope ratio of 1H:3V, h of 3 m, θ of 30°.

Figure 4.18 depicts the tendency of FS to decline as joint length increases. In the model where the joined rock layer is degraded, the value of FS decreases with increasing joint length. Most slopes are able to lower the FS by 50% with the joint length increasing from 3 m to 5 m. Only a few slopes are not modeled due to changes in other parameters, resulting in no FS being produced.

In summary, as the embankment directly bears the train weight, there is a part of the model where the damage is based on the embankment's structure when the strength of the jointed rock is relatively high. The joint parameter modification almost has no impact on the FS values, which range from 4.12 to 4.27. The stability of the model carrying stationary trains is represented by the jointed rock side slopes as the strength of the jointed rock declines. The rock slope height, joint orientation, spacing, length, and persistence greatly influence the stability of embankment models with train loads.

4.3.2 Influence of train speed for Set II models under a freight train with different speeds

Based on the preceding section's analysis, the slope heights and the related joint coefficients are two variables that significantly affect slope stability. Two subgroups are chosen in this section to investigate the influence of train loads on slope stability. A slope in subgroup 77 has a height of 3 m, a joint dip of 60°, a spacing of 0.5 m, and a persistence of 0.5. Subgroup 92 features a 3 m slope height, a 30° joint direction, a 1.5 m spacing, and a 0.7 persistence. A slope ratio of 1H:2V exists for both subgroups.

The freight train accelerates from a complete stop to a top speed of 120 km/h in progressive stages of 8 km/h. Table 4.14 (a) and (b) provide a summary of the FS results for joint lengths of 1, 3, and 5 m derived using the models in subgroups 77 and 92.

All six model findings in Table 4.14 demonstrate that FS reduces as train movement speed increases. When the train speed increases to its maximum for the model with a joint length of 1 m, the model's safety is governed by the nature of the embankment; if the embankment is unstable, the portion of the jointed rock is unaffected. Furthermore, subgroup 77 has slightly higher overall FS values than subgroup 92.

Table 4.14 (a) FS results of models in Subgroups 77 under various train speeds.

Group	Subgroup	Train speed v (km/h)	Loads P_{avg} (kPa)	FS		
				Joint length l (m)		
				1	3	5
Group 7	Subgroup 77	0	210.34	4.19*	3.77	2.86
		8	219.98	4.07*	3.68	2.72
		16	229.62	3.97*	3.58	2.64
		24	239.26	3.87*	3.50	2.57
		32	248.90	3.77*	3.39	2.49
		40	258.54	3.69*	3.31	2.41
		48	268.18	3.61*	3.23	2.34
		56	277.82	3.53*	2.94	2.28
		64	287.46	3.46*	2.87	2.23
		72	297.10	3.41*	2.81	2.16
		80	306.74	3.35*	2.76	2.09
		88	316.38	3.29*	2.71	2.00
		96	326.02	3.24*	2.68	1.87
		104	335.66	3.18*	2.63	1.86
		112	345.30	3.13*	2.62	1.56
		120	354.94	3.09*	2.27	1.41

Table 4.14 (b) FS results of models in Subgroups 92 under various train speeds.

Group	Subgroup	Train speed v (km/h)	Loads P_{avg} (kPa)	FS		
				Joint length l (m)		
				1	3	5
Group 8	Subgroup 92	0	210.34	4.18*	3.28	2.02
		8	219.98	4.06*	3.14	1.97
		16	229.62	3.95*	3.01	1.91
		24	239.26	3.85*	2.89	1.86
		32	248.90	3.77*	2.79	1.85
		40	258.54	3.68*	2.71	1.79
		48	268.18	3.60*	2.63	1.78
		56	277.82	3.52*	2.50	1.75
		64	287.46	3.46*	2.41	1.65
		72	297.10	3.39*	2.34	1.60
		80	306.74	3.33*	2.24	1.49
		88	316.38	3.27*	2.16	1.41
		96	326.02	3.22*	2.10	1.36
		104	335.66	3.17*	2.02	1.32
		112	345.30	3.11*	1.95	1.30
		120	354.94	3.07*	1.89	1.27

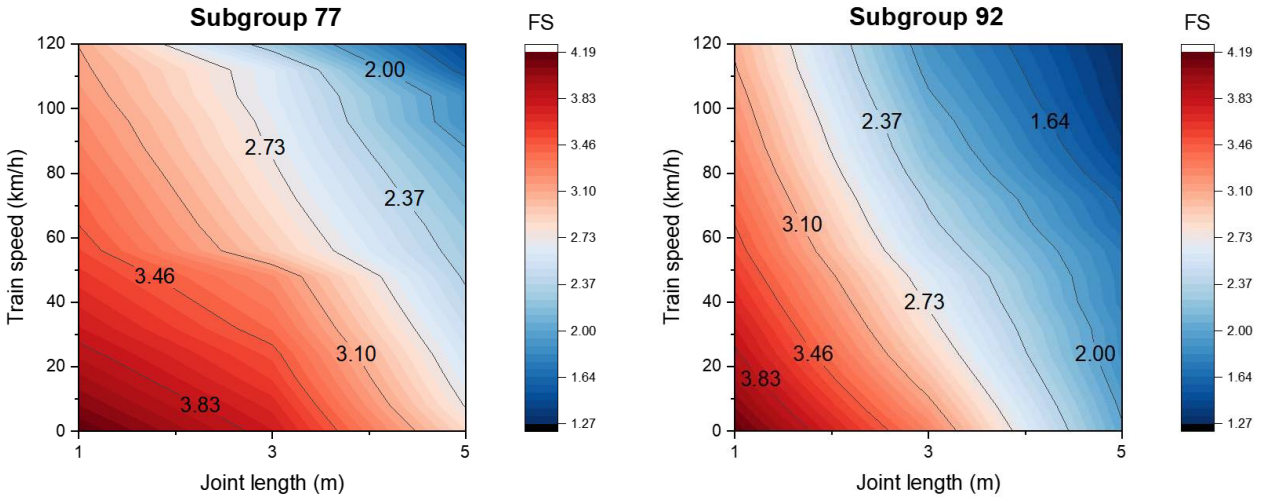

(a) (b)

Figure 4.19 Contour plots for FS results with increasing joint length:
(a) Models in Subgroup 77 under various train speeds; (b) Models in Subgroup 92 under various train speeds.

The FS contours generated from Table 4.14 are displayed in Figure 4.19, where the relationship between FS and joint length and train speed can be visualized. In the FS contour plots that contain subgroups 77 and 92, the legends remain identical and range from 1.27 to 4.19. Noticeably, in both plots, lower train speeds with shorter joint lengths are indicated to provide the model with more stability. On the contrary, rock slopes with longer joints are modeled to become less resilient when subjected to high-speed train operations.

4.4 General tendency under stationary train load condition

This section thoroughly compares the FS and its variations between Sets I and II. The rock mass with a single set of joints in the Set I model is laid out as natural ground beneath the embankment. The application of train loads to the model in Set I results in the model in Set II. The models utilized for comparison had a joint spacing of 0.5 m, a persistence of 0.5 m, an orientation of 60°, and a side slope ratio of 1H:2V. In Set I, subgroups 5, 17, and 29 correspond to the models with slope heights of 3, 6, and 9 m, whereas subgroups 77, 89, and 101 correspond to their counterparts in Set II with train loads. In particular, the stationary train load (P_{avg} of 210.34 kPa) is the external load utilized in the models included in the comparison of Set II.

The three sets of models are compared in Figure 4.20 for the same slope heights, with the left vertical axis representing corresponding FS values and the right vertical axis illustrating the degree of FS decrease when train loads are applied to the embankment. Scenarios I and II are specified as the Set I and Set II models for comparison, which are abbreviated to S.I and S.II in the legend of Figure 4.20.

Figure 4.20 shows that adding external loads to the model can reduce the FS value, which means the application of train loads may significantly decrease slope stability. The train parking on the embankment for the model with a 1 m joint length reduces the FS to around 4.2, which does not change noticeably as the slope height rises. When the joint length varies from 3 to 5 m,

joint lengthening causes an increase in the rate of FS change resulting from the application of train load. The FS drops roughly 30% or more when the joint length reaches 5 m.

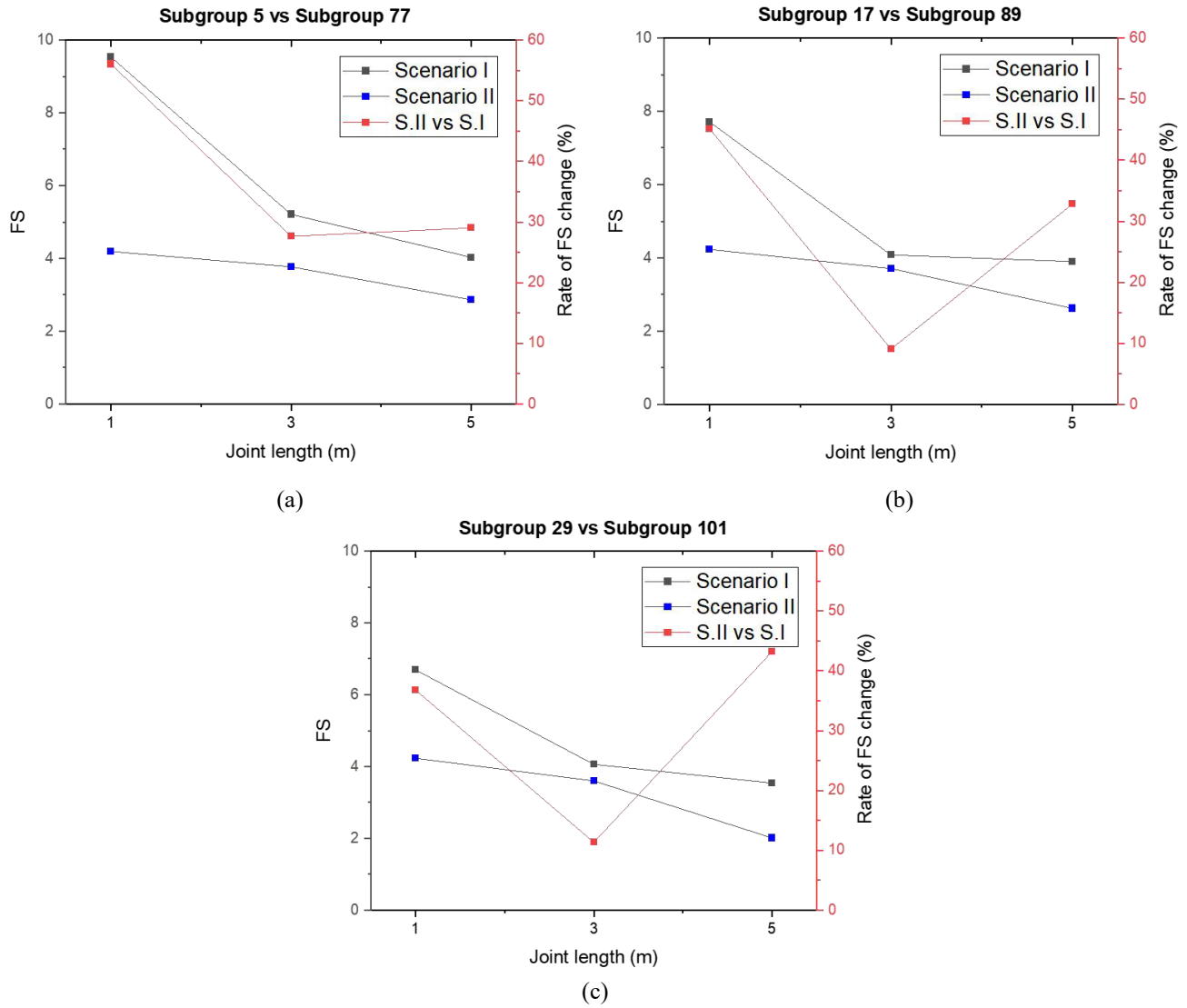

Figure 4.20 Relationships between the FS or rate of FS change under different scenarios and the joint length: (a) Models in Subgroup 5 and 77; (b) Models in Subgroup 17 and 89; (c) Models in Subgroup 29 and 101.

4.5 Recommendation of maximum safe train speed based on the study

Recommendations for the maximum safe train speed are given in this section based on the study models. Scenarios 1 and 2 are defined as models with a 1.5 m joint spacing and joint persistence of 0.5 and 0.7, respectively. The model scenarios are specified as Scenario 3 and Scenario 4 when the joint separation approaches 1 m and Scenario 5 and Scenario 6 when the joint spacing continues to fall 0.5 m. The top safe travel speeds for high-axle heavy-haul freight trains for all models in this investigation are shown in Figures 4.21 and 4.22. Some models cannot tolerate the freight train remaining stationary on the track, implying no maximum safe train speed, as illustrated in the area in black. The same legend is used in all models to indicate the increase in rate from 0 to 120 km/h.

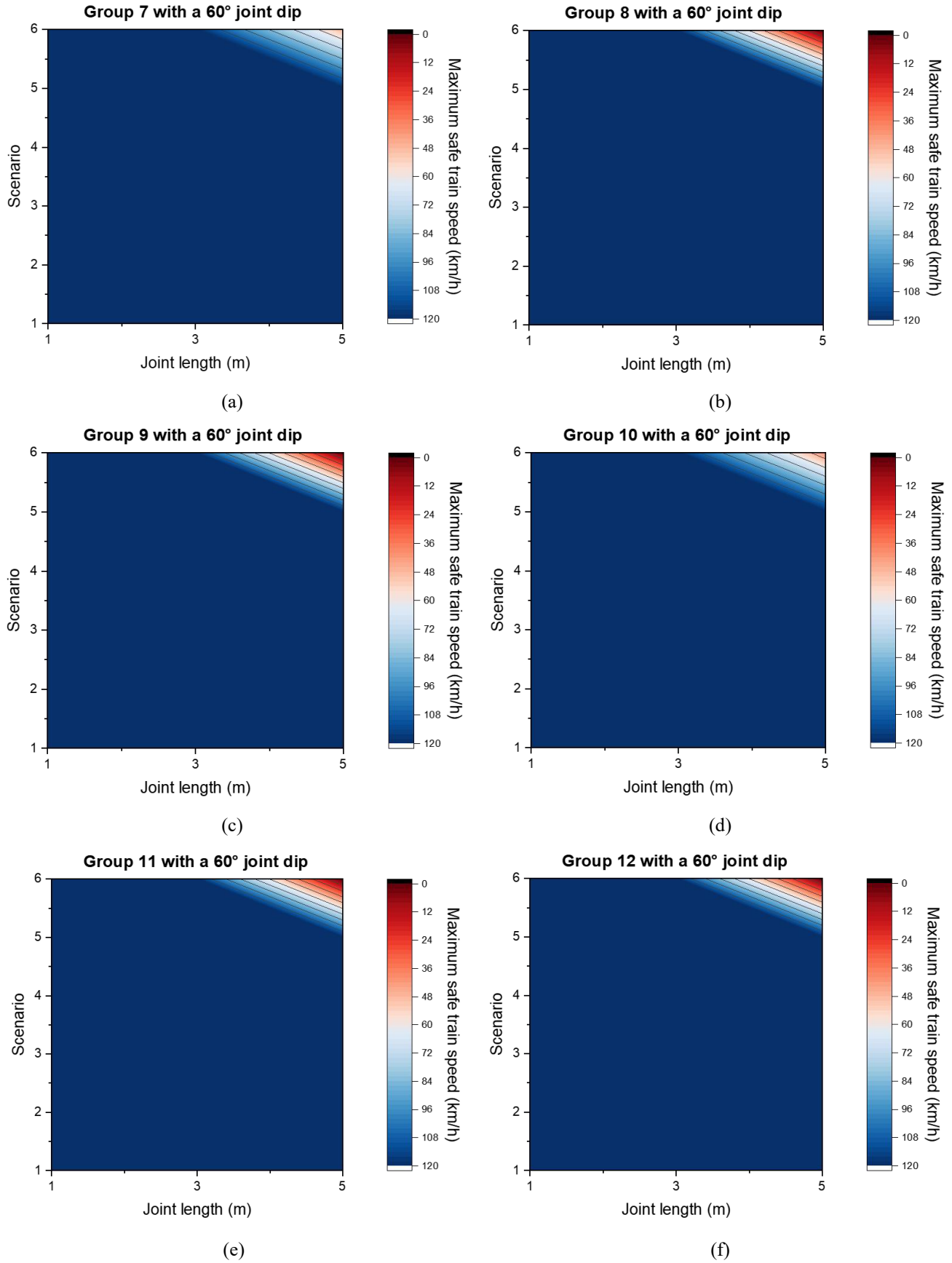

Figure 4.21 Contour plots for FS results (models with θ of 60°) with increasing joint length: (a) Models in Group 7; (b) Models in Group 8; (c) Models in Group 9; (d) Models in Group 10; (e) Models in Group 11; (f) Models in Group 12.

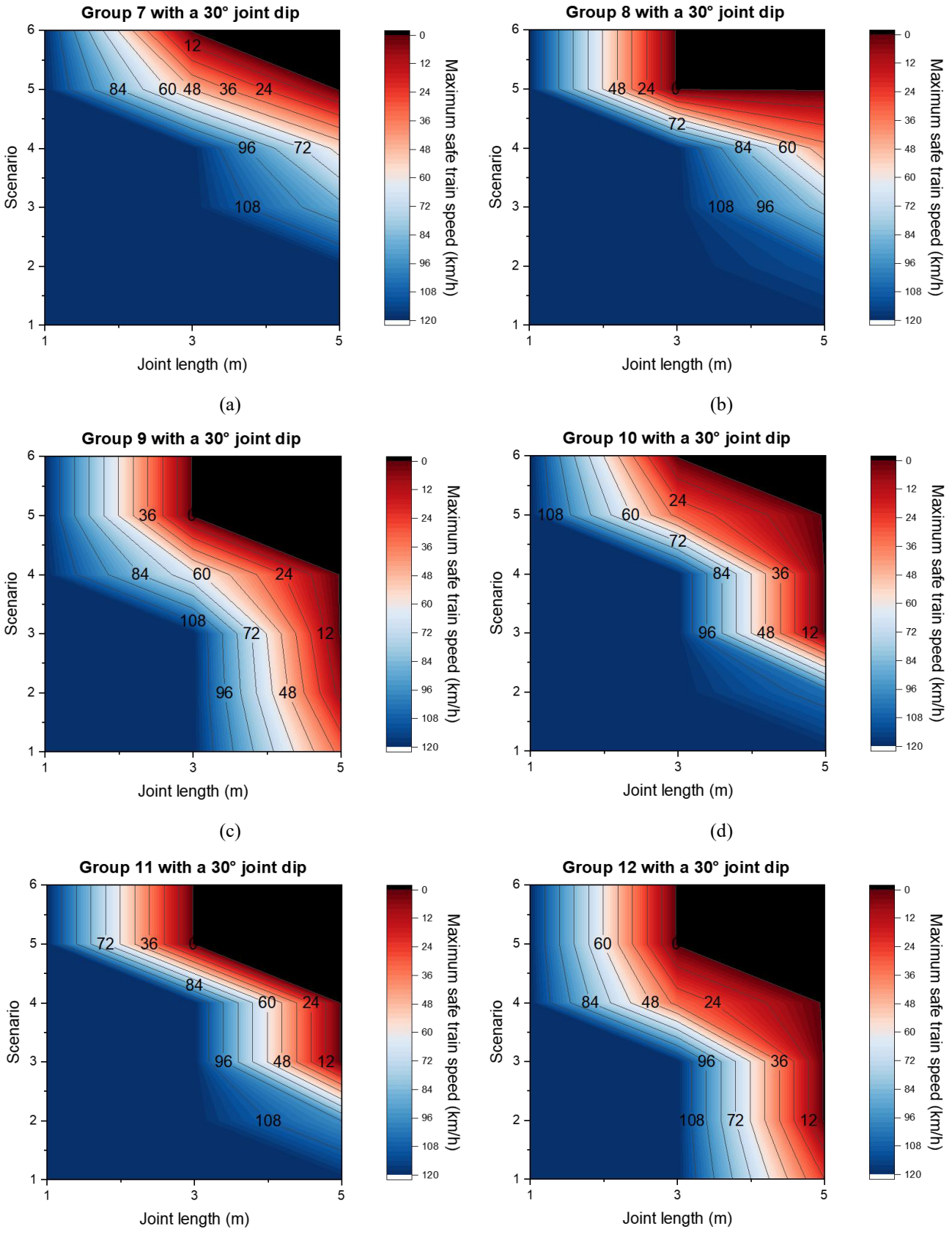

Figure 4.22 Contour plots for FS results (models with θ of 30°) with increasing joint length: (a) Models in Group 7; (b) Models in Group 8; (c) Models in Group 9; (d) Models in Group 10; (e) Models in Group 11; (f) Models in Group 12.

In general, all models with a 60° joint orientation can sustain trains moving on the track at a maximum speed of 120 km/h, as shown in Figure 4.21. The only model that could not resist the passage of a fast freight train is that with the smallest joint spacing (0.5 m), most considerable persistence (0.7 m), and largest length (5 m). In particular, Figure 4.21 (a) illustrates that the maximum train travel speed is 48 km/h when the slope height is 3 m and the slope ratio is 1H:2V. In all other circumstances, the train is unable to move on the track when the slope steepens or the slope height rises.

Figure 4.22 indicates that the maximum safe train speed tends to decline as the joint length grows. This tendency is particularly evident when the joint length increases from 3 to 5 m. Regardless of the other factors, a freight train can pass the track safely at the highest speed the specification allows (120 km/h) when the joint length is 1 m. Furthermore, gentler slopes and lower slope heights can support safer speeds. When the joint spacing is decreased to 0.5 m and the persistence is set to 0.5 for the model with a 3 m joint length and slope height, the model with a slope ratio of 1H:2V can withstand a reduction in maximum train speed from 120 km/h to 48 km/h. It can withstand a reduction in speed to 32 km/h when the slope ratio is raised to 1H:3V.

When the persistence or slope height increases, neither of the two models mentioned can accommodate trains on the track. The model with a slope height of 1H:3V is unable to accept a joint set with a maximum 1 m joint spacing together with a train on the track when the joint length is increased to 5 m. The maximum safe train speed can be reduced by decreasing the joint spacing or increasing the persistence until it no longer exists. Only the model with the broadest joint spacing (1.5 m) and the smallest persistence (0.5) has a maximum safe train speed of 24 km/h when the model slope ratio is 1H:3V, the slope height is 9 m, the joint orientation is 30°, and the joint length is 5 m.

Through this work, the maximum safe train speed can be linked to the slope, height of the rock mass, and joint-relevant dimensions. It is possible to build a cut slope with a maximum slope of 1H:2V and a maximum slope height of 9 m for rock mass with a single joint set oriented at 60°. Given that the spacing is not less than 1 m or the length is not greater than 3 m in a 60° single set of joint-oriented rock, it is advised to build an embankment that can sustain a heavy-haul freight train moving on the track at a maximum speed limit of 120 km/h.

Chapter 5 Conclusions and future work

5.1 Thesis summary

This research is targeted at developing a guideline reference for maximum safe train speeds for embankments constructed on different jointed rocks. The control variable method is applied to quantify the impact of specific parameters on the stability of railway slopes. The steps are as follows:

a. Determine the factors affecting the stability of embankments on the jointed rock.

b. Estimate the sensitivity of each influencing factor to slope stability using the FE-SSR method.

c. Explore the influence of different train speeds on the stability of railway embankments laid on jointed rock masses.

d. Implement parametric studies of the obtained numerical results to derive adequate guidelines for freight train traffic over jointed rock masses.

Chapter 2, which is a review of related literature, discusses the range of parameters, the methodology of the study, as well as mechanisms of joint damage and load transfer in the railroad bed for train traverse. Chapter 3 establishes the numerical modeling and supports the reliability of RS2 to assist this study by simulating examples. Chapter 4 gives a parametric analysis of the model's performance, followed by recommendations. In this study, specific slope geometry and joint features are used to establish the maximum safe speed for the passage of freight trains.

5.2 Conclusion

The parametric analysis in this research is based on two sets of models. Given the slope geometry and joint characteristics in the models with train loads, it is also possible to ascertain the maximum safe speed permitted for freight trains. For each model, the slope stability can be represented by the factor of safety. More stable slopes are indicated by larger FS values. The train travels on an embankment with a particular geometry, and both the embankment and the jointed rock slope beneath it have specific materials, as stated in Section 3.1. Typical freight trains operating on main straight lines in the simulated cases ought to adhere to the subsequent guidelines:

a. The train can maintain a maximum speed restriction of 120 km/h when moving from a slope height of 3 m to 9 m in the rock slope with a single set of joints of 1 m length.

b. When the joints with persistence of 0.7 in the bedrock are 5 m long and 0.5 m spacing, rains are not permitted to travel through this portion of the railroad.

c. On rock slopes with joint orientation of 60°, most trains can pass the tracks at the upper limit speed. It is crucial that the joint length should not be less than 3 m, and joint spacing should remain within 1 m until the train reaches a point where the joint orientation changes to 30°. Otherwise, the train is mostly forbidden from passing, and the safe travel speed is limited to a relatively low speed.

d. At a maximum speed of 48 km/h, the train can constantly traverse the railroad section with a

slope ratio of 1H:2V, when the bedrock has a joint length and slope height of 3 m, joint spacing of 0.5 m, and persistence of 0.5. When the slope height increases to 6 m or above, trains are not allowed to travel on that section of the railroad or even stop.

e. Most of the railroad segment in bedrock with joints aligned at 30° and a length of 5 m is closed to freight trains when the cut slope is steep (1H:3V) and high (9 m). Trains can travel through this area at a low speed of 24 km/h, except for the joint spacing when it expands to 1.5 m and persistence approaches the upper limit of 0.5.

Elevated slope height, lower value of joint direction, and more compact joint spacing along with greater persistence and lengthened joint all favorably impact slope stability for both the train load model and the no external load model. In conclusion, train speeds can reach a maximum upper limit of 120 km/h for rocks with a single joint set of 60° dip with spacing not less than 1 m or length not larger than 3 m.

Furthermore, one of the most notable findings is that, in the case of the bedrock model with a joint length of 1 m, the freight train's transition from stationary to high speed mainly impairs the bearing capacity of the model in the embankment section. The yielding point occurs in the embankment under a high-speed operation train when the joint length is increased to 3 m for bedrock with joint orientation of 60° and joint spacing of at least 1 m; when the joint spacing narrows to 0.5 m, the jointed rock layer may be affected by bearing capacity failure. For the bedrock containing joints with a length of 5 m, the yielding point is in the joints near the bottom of the embankment when the train passes by. The embankment collapses as a result of bedrock deterioration.

5.3 Limitations

There are many prerequisites that need to be followed for the advancement of this study, which represent a limitation of this research and need to be further improved in the subsequent studies.

a. Temperature, precipitation, and wind speed fluctuations occurring naturally in the environment are not considered.

b. The train is configured to run on a straight main track in all of the models used in this investigation, which are tangential track portions.

c. When there is a relative displacement between the track and the train wheels, the track is thought of as a smooth surface producing no friction.

d. The train is programmed to travel across the track at a constant speed. Dynamically changing loads are not examined by the SSR approach. Transferring train loads to the embankment is regarded as an additional static force.

e. In this work, a single set of parallel deterministic joints was employed for the parametric investigation to more intuitively grasp the impact of each joint feature on embankment stability. The condition of the rock mass's joints is considered idealized and standardized.

f. In this study, the direction of the joints is considered to be between 0°–90°, with a single mechanism of joint damage.

5.4 Future work

Future studies on this subject can be improved in some ways to make the research more practical. Future topics include but are not limited to the following.

a. The impacts of weather and environmental variations on material properties should be considered, such as temperature, humidity, and so on.

b. Curving tracks should be added to models to incorporate the centrifugal forces produced by train turns.

c. For further research, uneven tracks are advised to be investigated thoroughly.

d. Various joint damage mechanisms are advised to analyze caused by different joint directions, such as toppling failure on side slopes.

e. Different configurations for the joint networking are recommended to add into models, which are more indicative of the jointing condition of the mountain after extensive weathering.

This research and future work might contribute to reducing train accidents and the cost of railway projects. Guidelines for the maximum allowable train speed might be derived with a function of settlement and slope deformation, providing a reference for future construction and rehabilitation of rock-based embankments.

References

1. Abramson, L. W., Lee, T. S., Sharma, S., & Boyce, G. M. (2001). *Slope stability and stabilization methods*. John Wiley & Sons.
2. Alejano, L. R., Ferrero, A. M., Ramírez-Oyanguren, P., & Álvarez-Fernández, M. (2011). Comparison of limit-equilibrium, numerical and physical models of wall slope stability. *International Journal of Rock Mechanics and Mining Sciences*, *48*(1), 16–26. https://doi.org/10.1016/j.ijrmms.2010.06.013
3. American Railway Engineering and Maintenance-of-Way Association [AREMA]. (2010). *2010 manual for railway engineering*. American Railway Engineering and Maintenance-of-Way Association.
4. American Railway Engineering and Maintenance-of-Way Association [AREMA]. (2012). *2012 manual for railway engineering*. American Railway Engineering and Maintenance-of-Way Association.
5. American Railway Engineering and Maintenance-of-Way Association [AREMA]. (2018). *2018 manual for railway engineering*. American Railway Engineering and Maintenance-of-Way Association.
6. Andrade, A. R. (2008). *Renewal decisions from a Life-cycle Cost (LCC) perspective in railway infrastructure: An integrative approach using separate LCC models for rail and ballast components* [M.S. thesis]. Technical University of Lisbon.
7. Assefa, E., Lin, L. J., Sachpazis, D. C. I., Feng, D. H., Shu, S. X., & Anastasiadis, D. A. S. (2016). Probabilistic slope stability evaluation for the new railway embankment in Ethiopia. *Electronic Journal of Geotechnical Engineering*, *21*, 4247–4272.
8. Baecher, G. B., Lanney, N. A., & Einstein, H. H. (1977). Statistical description of rock properties and sampling. *Proceedings of the 18th U.S. Symposium on Rock Mechanics*, *5C*, 1–8.
9. Balmer, G. (1952). A general analytical solution for Mohr's envelope. *Proceedings of American Society of Test Materials*, *52*, 1260–1271.
10. Bhavikatti, S. S. (2005). *Finite element analysis*. New Age International.
11. Bobet, A., & Einstein, H. H. (1998). Fracture coalescence in rock-type materials under uniaxial and biaxial compression. *International Journal of Rock Mechanics and Mining Sciences*, *35*(7), 863–888. https://doi.org/10.1016/s0148-9062(98)00005-9
12. Bourdeau, P., & Harr, M. E. (1989). Stochastic theory of settlement of loose cohesionless soils. *Geotechnique*, *39*(4), 641–654. https://doi.org/10.1680/geot.1989.39.4.641
13. Brown, E. T. (1970). Strength of models of rock with intermittent joints. *Journal of the Soil Mechanics and Foundations Division*, *96*(6), 1935–1949. https://doi.org/10.1061/jsfeaq.0001479
14. Brown, E. T. (1981). *Rock characterization, testing & monitoring: ISRM suggested methods*. http://ci.nii.ac.jp/ncid/BA30333389
15. Burg, J.-P. (2020). *Faults and joints*. https://www.files.ethz.ch/structuralgeology/jpb/files/english/4joints.pdf
16. Cai, M. (2010). Practical estimates of tensile strength and Hoek–Brown strength parameter m_i of brittle rocks. *Rock Mechanics and Rock Engineering*, *43*(2), 167–184. https://doi.org/10.1007/s00603-009-0053-1
17. Canadian National Railway Company [CN]. (2019). *Engineering specifications for industrial tracks*.
18. Cheng, Y. M., & Lau, C. K. (2014). *Slope stability analysis and stabilization: New methods and insight*

(2nd ed.). CRC Press.
19. Chowdhury, R., Flentje, P., & Bhattacharya, G. (2009). *Geotechnical slope analysis*. Taylor & Francis Group.
20. Connolly, D. P., Kouroussis, G., Giannopoulos, A., Verlinden, O., Woodward, P. K., & Forde, M. C. (2014). Assessment of railway vibrations using an efficient scoping model. *Soil Dynamics and Earthquake Engineering*, *58*, 37–47. https://doi.org/10.1016/j.soildyn.2013.12.003
21. Davarpanah, S. M., Sharghi, M., Vásárhelyi, B., & Török, Á. (2021). Characterization of Hoek–Brown constant m_i of quasi-isotropic intact rock using rigidity index approach. *Acta Geotechnica*, *17*(3), 877–902. https://doi.org/10.1007/s11440-021-01229-2
22. Davis, R. O., & Selvadurai, A. P. S. (2002). *Plasticity and geomechanics*. Cambridge University Press. https://doi.org/10.1017/cbo9780511614958
23. Dershowitz, W. (1984). *Rock joint systems* [Ph.D. Thesis]. Massachusetts Institute of Technology. https://dspace.mit.edu/handle/1721.1/27939
24. Dershowitz, W., & Einstein, H. H. (1988). Characterizing rock joint geometry with joint system models. *Rock Mechanics and Rock Engineering*, *21*(1), 21–51. https://doi.org/10.1007/bf01019674
25. Eberhardt, E. (2003). *Rock slope stability analysis—utilization of advanced numerical techniques*. Earth and Ocean Sciences at UBC.
26. Egeli, İ., & Uşun, H. (2012). Designing high-speed train railway embankments using finite element analysis. *Arabian Journal for Science and Engineering*, *37*(8), 2127–2136. https://doi.org/10.1007/s13369-012-0302-6
27. Esveld, C. (2001). *Modern railway track* (2nd ed.). MRT-Productions.
28. Ge, X. (1987). Study on deformation and strength behaviour of the large-sized triaxial rock samples under cyclic loading. *Rock Soil Mech*, *8*(2), 11–19.
29. Goodman, R. E. (1991). *Introduction to rock mechanics*. John Wiley & Sons.
30. Griffiths, D. V., & Lane, P. A. (1999). Slope stability analysis by finite elements. *Geotechnique*, *49*(3), 387–403. https://doi.org/10.1680/geot.1999.49.3.387
31. Guo, L., Chen, J., Wang, J., Cai, Y., & Deng, P. (2016). Influences of stress magnitude and loading frequency on cyclic behavior of K0-consolidated marine clay involving principal stress rotation. *Soil Dynamics and Earthquake Engineering*, *84*, 94–107. https://doi.org/10.1016/j.soildyn.2016.01.024
32. Haimson, B. C., Heins, R. W., & WISCONSIN UNIV-MADISON ENGINEERING EXPERIMENT STATION. (1972). *Aspects of mechanical behavior of rock under static and cyclic loading. Part B. Mechanical behavior of rock under cyclic loading*.
33. Hammah, R. E., Yacoub, T. E., Corkum, B. C., & Curran, J. H. (2005, June 25–29). *The shear strength reduction method for the generalized Hoek-Brown criterion* [Paper presentation]. 40th U.S. Symposium on Rock Mechanics (USRMS), Anchorage, Alaska, United States.
34. Hammah, R. E., Yacoub, T. , Corkum, B., Wibowo, F., & Curran, J. H. (2007, May 27–31). *Analysis of blocky rock slopes with finite element shear strength reduction analysis* [Paper presentation]. 1st Canada–U.S. Rock Mechanics Symposium, Vancouver, British Columbia, Canada.
35. Hammah, R. E., Yacoub, T. E., & Curran, J. H. (2009, June 28–July 1). *Probabilistic slope analysis with*

the finite element method [Paper presentation]. 43rd U.S. Rock Mechanics Symposium & 4th U.S. – Canada Rock Mechanics Symposium, Asheville, North Carolina, United States.
36. Hoek, E. (2007). *Practical rock engineering*.
37. Hoek, E., & Bray, J. D. (1981). *Rock slope engineering* (3rd ed.). CRC Press.
38. Hoek, E., & Brown, E. T. (1980). *Underground excavations in rock*. CRC Press.
39. Hoek, E., & Marinos, P. (2000). Predicting tunnel squeezing problems in weak heterogeneous rock masses. *Tunnels and tunnelling international*, *32*(11), 45–51.
40. Hoek, E., & Martin, C. D. (2014). Fracture initiation and propagation in intact rock – A review. *Journal of Rock Mechanics and Geotechnical Engineering*, *6*(4), 287–300. https://doi.org/10.1016/j.jrmge.2014.06.001
41. Hudson, J., & Priest, S. D. (1979). Discontinuities and rock mass geometry. *International Journal of Rock Mechanics and Mining Sciences & Geomechanics Abstracts*, *16*(6), 339–362. https://doi.org/10.1016/0148-9062(79)90001-9
42. Indraratna, B., Chu, J., & Rujikiatkamjorn, C. (2015). *Ground improvement case histories: Compaction, grouting and geosynthetics*. Butterworth-Heinemann.
43. Indraratna, B., Oliveira, D., & Jayanathan, M. (2008). Revised shear strength model for infilled rock joints considering overconsolidation effect. https://ro.uow.edu.au/engpapers/485
44. Indraratna, B., Salim, W., & Rujikiatkamjorn, C. (2011). *Advanced rail geotechnology—Ballasted track*. CRC Press.
45. Jalote, P. M., Kumar A., & Kumar V. (1996). Geotechniques applied in the design of the machine hall cavern, Nathpa Jhakri Hydel Project, N.W. Himalaya, India. *J. Engng Geol. (India)*, *XXV*(1–4), 181–192.
46. Karakus, M., Liu, Y., Zhang, G., & Tang, H. (2016). A new shear strength model incorporating influence of infill materials for rock joints. *Geomechanics and Geophysics for Geo-Energy and Geo-Resources*, *2*(3), 183–193. https://doi.org/10.1007/s40948-016-0032-4
47. Kerr, A. D. (2003). *Fundamentals of railway track engineering*. Simmons Boardman Publishing Company.
48. Kikuchi, K., Kuroda, H., & Mito, Y. (1987, August 30–September 3). *Stochastic estimation and modelling of rock joint distribution based on statistical sampling* [Paper presentation]. 6th ISRM Congress, Montreal, Québec, Canada.
49. Kramer, S. L. (1996). *Geotechnical earthquake engineering*. Prentice-Hall.
50. Kulatilake, P. H., & Wu, T. H. (1984). Estimation of mean trace length of discontinuities. *Rock Mechanics and Rock Engineering*, *17*(4), 215–232. https://doi.org/10.1007/bf01032335
51. Lajtai, E. (1974). Brittle fracture in compression. *International Journal of Fracture*, *10*(4), 525–536. https://doi.org/10.1007/bf00155255
52. Lake, L. W., Fanchi, J. R., Mitchell, R. F., Arnold, K. E., Clegg, J. D., Holstein, E. D., & Warner, H. R. J. (2006). *Petroleum engineering handbook*. Society of Petroleum Engineers.
53. Laryea, S., Baghsorkhi, M. S., Ferellec, J.-F., McDowell, G. R., & Chen, C. (2014). Comparison of performance of concrete and steel sleepers using experimental and discrete element methods. *Transportation Geotechnics*, *1*(4), 225–240. https://doi.org/10.1016/j.trgeo.2014.05.001
54. Li, B., Wong, R., Xu, B., & Yang, B. (2018). Comprehensive stability analysis of an inclined wellbore

embedded in Colorado shale formation for thermal recovery. *International Journal of Rock Mechanics and Mining Sciences*, *110*, 168–176. https://doi.org/10.1016/j.ijrmms.2018.07.019

55. Li, D., Hyslip, J., Sussmann, T., & Chrismer, S. (2015). *Railway geotechnics*. CRC Press.
56. Li, L. Y., Che, F. X., & Liu, D. A. (2000). Lei yanshi cailiao duo liewen moxing pohuai fenxi [Multi-crack model failure analysis of rock-like materials]. *Proceedings of Mechanics 2000*.
57. Lin, H., Zhong, W., Xiong, W., & Tang, W. (2014). Slope stability Analysis using limit equilibrium method in nonlinear criterion. *The Scientific World Journal*, *2014*, 1–7. https://doi.org/10.1155/2014/206062
58. Lin, P., Wong, R. H. C., Chau, K. T., & Tang, C. A. (2000). Multi-crack coalescence in rock-like material under uniaxial and biaxial loading. *Key Engineering Materials*, *183–187*, 809–814. https://doi.org/10.4028/www.scientific.net/kem.183-187.809
59. Logan, D. L. (2011). *A first course in the finite element method* (SI version). Cengage Learning.
60. Morriss, P. (1984). Australian mineral foundation: Probabilistic design of rock slopes. In P. Morriss (Ed.), *Rock slope engineering*.
61. Mosayebi, S. A., Esmaeili, M., & Zakeri, J. A. (2020). Dynamic train-track interactions and stress distribution patterns in ballasted track layers. *Journal of Transportation Engineering*, *146*(1), 04019042. https://doi.org/10.1061/jpeodx.0000140
62. Nikishkov, G. P. (2009). Introduction to the finite element method. In G. P. Nikishkov (Ed.), *Introduction to the finite element method*. University of Aizu.
63. Nikolić, M., Roje-Bonacci, T., & Ibrahimbegović, A. (2016). Overview of the numerical methods for the modelling of rock mechanics problems. *Tehnicki Vjesnik-technical Gazette*, *23*(2), 627–637. https://doi.org/10.17559/tv-20140521084228
64. Norrish, N. I., & Wyllie, D. C. (1996). Landslides: Investigation and mitigation. Chapter 15–Rock slope stability analysis. *Transportation Research Board Special Report*, *247*. https://onlinepubs.trb.org/Onlinepubs/sr/sr247/sr247-015.pdf
65. Pahl, P. J. (1981). Estimating the mean length of discontinuity traces. *International Journal of Rock Mechanics and Mining Sciences & Geomechanics Abstracts*, *18*(3), 221–228. https://doi.org/10.1016/0148-9062(81)90976-1
66. Phien-Wej, N., Shrestha, U. B, & Rantucci, G. (1990). Effect of infill thickness on shear behavior of rock joints. *Proceedings of International symposium on rock joints*, 289–294. https://pascal-francis.inist.fr/vibad/index.php?action=getRecordDetail&idt=6527006
67. Priest, S. D., & Hudson, J. A. (1981). Estimation of discontinuity spacing and trace length using scanline surveys. *International Journal of Rock Mechanics and Mining Sciences & Geomechanics Abstracts*, *18*(3), 183–197. https://doi.org/10.1016/0148-9062(81)90973-6
68. Profillidis, V. A. (2014). *Railway management and engineering* (4th ed.). Routledge. https://doi.org/10.4324/9781315245362
69. Railway Track & Structures. (2008). M/W budgets to climb in 2008. *Railway Track & Structures*, *104*(1), 19–25.
70. Rao, S. S. (2017). *The finite element method in engineering*. Butterworth-Heinemann.
71. Reyes, O., & Einstein, H. H. (1991, September 16–20). *Failure mechanisms of fractured rock–A fracture coalescence model* [Paper presentation]. 7th ISRM Congress, Aachen, Germany.
72. Rocscience. (2021). *RS2: Convergence criteria*. Theory manuals. Retrieved August 30, 2023, from

https://www.rocscience.com/help/rs2/verification-theory/theory-manuals/general
73. Rocscience. (2023). *RS2: Joint network overview*. Joint network. Retrieved August 30, 2023, from https://www.rocscience.com/help/rs2/documentation/rs2-model/joints/joint-networks/joint-network-overview
74. Sagong, M., & Bobet, A. (2002). Coalescence of multiple flaws in a rock-model material in uniaxial compression. *International Journal of Rock Mechanics and Mining Sciences*, *39*(2), 229–241. https://doi.org/10.1016/s1365-1609(02)00027-8
75. Saputro, S. E., Ricardianto, P., Mulyani, H., & Susanto, P. C. (2020). Review of track gauge for Trans-Sumatera railway revitalization and development. *Jurnal Penelitian Transportasi Darat*, 22(1), 25–36. https://doi.org/10.25104/jptd.v22i1.1597
76. Sheng, X., Zheng, W., Zhu, Z., Luo, T., & Zheng, Y. (2020). Properties of rubber under-ballast mat used as ballastless track isolation layer in high-speed railway. *Construction and Building Materials*, *240*, 117822. https://doi.org/10.1016/j.conbuildmat.2019.117822
77. Shrivastava, A. K., & Rao, K. S. (2014, May 27 – 29). *Effect of infill thickness on shear behaviour of jointed rock under CNS conditions* [Paper presentation]. ISRM Regional Symposium – EUROCK 2014, Vigo, Spain.
78. Sinha, U. N., & Singh, B. (2000). Testing of rock joints filled with gouge using a triaxial apparatus. *International Journal of Rock Mechanics and Mining Sciences*, *37*(6), 963–981. https://doi.org/10.1016/s1365-1609(00)00030-7
79. Stagg, K. G., & Zienkiewicz, O. C. (1968). *Rock Mechanics in Engineering practice*. John Wiley & Sons.
80. Starns, K. E. M. (2012). *The Russian railways and imperial intersections in the Russian Empire* [M.A. thesis]. University of Washington.
81. Technical Specialist Rolling Stock Performance Standards. (2013). *Wheel and axles reference manual*. RailCorp.
82. Sun, C., Chai, J., Xu, Z., Qin, Y., & Chen, X. (2016). Stability charts for rock mass slopes based on the Hoek-Brown strength reduction technique. *Engineering Geology*, *214*, 94–106. https://doi.org/10.1016/j.enggeo.2016.09.017
83. Transport Canada. (2018). Transportation in Canada 2018. Transport Canada.
84. Transport Canada. (2020). Transportation in Canada 2020. Transport Canada.
85. Transportation Safety Board of Canada [TSB]. (1996). *Railway investigation report* (Report No. R95V0017). Transportation Safety Board of Canada.
86. Transportation Safety Board of Canada [TSB]. (2016). *Railway investigation report* (Report No. R14Q0045). Transportation Safety Board of Canada.
87. Transportation Safety Board of Canada [TSB]. (2020). *Rail transportation occurrences in 2020*. Transportation Safety Board of Canada.
88. Tu, Y., Liu, X., Zhong, Z., & Li, Y. (2016). New criteria for defining slope failure using the strength reduction method. *Engineering Geology*, *212*, 63–71. https://doi.org/10.1016/j.enggeo.2016.08.002
89. Wang, Z., Li, Y., & Wang, J. G. (2008). A method for evaluating dynamic tensile damage of rock. *Engineering Fracture Mechanics*, *75*(10), 2812–2825. https://doi.org/10.1016/j.engfracmech.2008.01.005
90. Railway Tie Association [RTA]. (2016). *The Tie Guide*. TieGuide. Retrieved March 23, 2022, from https://www.rta.org/index.php?option=com_content&view=article&id=58:tieguide&catid=20:site-content

91. Wyllie, D. C. (1999). *Foundations on rock: Engineering practice* (2nd ed.). E & FN Spon.
92. Wyllie, D. C., & Mah, C. W. (2004). *Rock slope engineering: Civil and mining* (4th ed.). Spon Press.
93. Xu, S. (2019). *Effect of rapid drawdown on the stability of railway embankments* [M.A.Sc. thesis]. Concordia University.
94. Zhang, T. W., Cui, Y. J., Lamas-Lopez, F., Calon, N., & D ' Aguiar, S. C. (2016). Modelling stress distribution in substructure of French conventional railway tracks. *Construction and Building Materials*, *116*, 326–334.
https://doi.org/10.1016/j.conbuildmat.2016.04.137
95. Zhang, Y., Han, J., Song, H., & Liu, Y. (2021). Subway embedded track geometric irregularity safety limits. *Chinese Journal of Mechanical Engineering*, *34*(1), 1-10.
https://doi.org/10.1186/s10033-021-00614-y
96. Zheng, Y., & Zhao, S. (2004). Application of strength reduction FEM in soil and rock slope. *Chinese Journal of Rock Mechanics and Engineering*, *23*(19), 3381-3388.
97. Zhou, X. P., Bi, J., & Qian, Q. H. (2014). Numerical simulation of crack growth and coalescence in rock-like materials containing multiple pre-existing flaws. *Rock Mechanics and Rock Engineering*, *48*(3), 1097–1114.
https://doi.org/10.1007/s00603-014-0627-4
98. Zhu, L. (2017). *Jieli kuozhan moshi ji jieli yanti bianpo pohuai jili yanjiu* [*Joint propagation modes and fracture mechanisms of jointed rock slope*, Ph.D. Thesis]. Chengdu University of Technology.
99. Zienkiewicz, O. C., Humpheson, C., & Lewis, R. W. (1975). Associated and non-associated visco-plasticity and plasticity in soil mechanics. *Geotechnique*, *25*(4), 671–689.
https://doi.org/10.1680/geot.1975.25.4.671

Appendix A

Table A1 Cases in Set I – Jointed rock slope model.

Group	Slope ratio H:V	Slope height h (m)	Subgroup	Joint dip θ (°)	Joint spacing s (m)	Joint persistence p	Joint length l (m)
Group 1	1:2	3	**Subgroup 1**	60	1.5	0.5	1, 3, 5
			Subgroup 2	60	1.5	0.7	1, 3, 5
			Subgroup 3	60	1.0	0.5	1, 3, 5
			Subgroup 4	60	1.0	0.7	1, 3, 5
			Subgroup 5	60	0.5	0.5	1, 3, 5
			Subgroup 6	60	0.5	0.7	1, 3, 5
			Subgroup 7	30	1.5	0.5	1, 3, 5
			Subgroup 8	30	1.5	0.7	1, 3, 5
			Subgroup 9	30	1.0	0.5	1, 3, 5
			Subgroup 10	30	1.0	0.7	1, 3, 5
			Subgroup 11	30	0.5	0.5	1, 3, 5
			Subgroup 12	30	0.5	0.7	1, 3, 5
Group 2	1:2	6	**Subgroup 13**	60	1.5	0.5	1, 3, 5
			Subgroup 14	60	1.5	0.7	1, 3, 5
			Subgroup 15	60	1.0	0.5	1, 3, 5
			Subgroup 16	60	1.0	0.7	1, 3, 5
			Subgroup 17	60	0.5	0.5	1, 3, 5
			Subgroup 18	60	0.5	0.7	1, 3, 5
			Subgroup 19	30	1.5	0.5	1, 3, 5
			Subgroup 20	30	1.5	0.7	1, 3, 5
			Subgroup 21	30	1.0	0.5	1, 3, 5
			Subgroup 22	30	1.0	0.7	1, 3, 5
			Subgroup 23	30	0.5	0.5	1, 3, 5
			Subgroup 24	30	0.5	0.7	1, 3, 5
Group 3	1:2	9	**Subgroup 25**	60	1.5	0.5	1, 3, 5
			Subgroup 26	60	1.5	0.7	1, 3, 5
			Subgroup 27	60	1.0	0.5	1, 3, 5
			Subgroup 28	60	1.0	0.7	1, 3, 5
			Subgroup 29	60	0.5	0.5	1, 3, 5
			Subgroup 30	60	0.5	0.7	1, 3, 5
			Subgroup 31	30	1.5	0.5	1, 3, 5
			Subgroup 32	30	1.5	0.7	1, 3, 5
			Subgroup 33	30	1.0	0.5	1, 3, 5
			Subgroup 34	30	1.0	0.7	1, 3, 5

			Subgroup 35	30	0.5	0.5	1, 3, 5
			Subgroup 36	30	0.5	0.7	1, 3, 5
Group 4	1:3	3	**Subgroup 37**	60	1.5	0.5	1, 3, 5
			Subgroup 38	60	1.5	0.7	1, 3, 5
			Subgroup 39	60	1.0	0.5	1, 3, 5
			Subgroup 40	60	1.0	0.7	1, 3, 5
			Subgroup 41	60	0.5	0.5	1, 3, 5
			Subgroup 42	60	0.5	0.7	1, 3, 5
			Subgroup 43	30	1.5	0.5	1, 3, 5
			Subgroup 44	30	1.5	0.7	1, 3, 5
			Subgroup 45	30	1.0	0.5	1, 3, 5
			Subgroup 46	30	1.0	0.7	1, 3, 5
			Subgroup 47	30	0.5	0.5	1, 3, 5
			Subgroup 48	30	0.5	0.7	1, 3, 5
Group 5	1:3	6	**Subgroup 49**	60	1.5	0.5	1, 3, 5
			Subgroup 50	60	1.5	0.7	1, 3, 5
			Subgroup 51	60	1.0	0.5	1, 3, 5
			Subgroup 52	60	1.0	0.7	1, 3, 5
			Subgroup 53	60	0.5	0.5	1, 3, 5
			Subgroup 54	60	0.5	0.7	1, 3, 5
			Subgroup 55	30	1.5	0.5	1, 3, 5
			Subgroup 56	30	1.5	0.7	1, 3, 5
			Subgroup 57	30	1.0	0.5	1, 3, 5
			Subgroup 58	30	1.0	0.7	1, 3, 5
			Subgroup 59	30	0.5	0.5	1, 3, 5
			Subgroup 60	30	0.5	0.7	1, 3, 5
Group 6	1:3	9	**Subgroup 61**	60	1.5	0.5	1, 3, 5
			Subgroup 62	60	1.5	0.7	1, 3, 5
			Subgroup 63	60	1.0	0.5	1, 3, 5
			Subgroup 64	60	1.0	0.7	1, 3, 5
			Subgroup 65	60	0.5	0.5	1, 3, 5
			Subgroup 66	60	0.5	0.7	1, 3, 5
			Subgroup 67	30	1.5	0.5	1, 3, 5
			Subgroup 68	30	1.5	0.7	1, 3, 5
			Subgroup 69	30	1.0	0.5	1, 3, 5
			Subgroup 70	30	1.0	0.7	1, 3, 5
			Subgroup 71	30	0.5	0.5	1, 3, 5
			Subgroup 72	30	0.5	0.7	1, 3, 5

Appendix B

Table B1 Cases in Set II – Jointed rock slope model under train load conditions.

Group	Slope ratio H:V	Slope height h (m)	Subgroup	Joint dip θ (°)	Joint spacing s (m)	Joint persistence p	Joint length l (m)	Maximum safe train speed v km/h
Group 7	1:2	3	**Subgroup 73**	60	1.5	0.5	1, 3, 5	0–120
			Subgroup 74	60	1.5	0.7	1, 3, 5	0–120
			Subgroup 75	60	1.0	0.5	1, 3, 5	0–120
			Subgroup 76	60	1.0	0.7	1, 3, 5	0–120
			Subgroup 77	60	0.5	0.5	1, 3, 5	0–120
			Subgroup 78	60	0.5	0.7	1, 3, 5	0–120
			Subgroup 79	30	1.5	0.5	1, 3, 5	0–120
			Subgroup 80	30	1.5	0.7	1, 3, 5	0–120
			Subgroup 81	30	1.0	0.5	1, 3, 5	0–120
			Subgroup 82	30	1.0	0.7	1, 3, 5	0–120
			Subgroup 83	30	0.5	0.5	1, 3, 5	0–120
			Subgroup 84	30	0.5	0.7	1, 3, 5	0–120
Group 8	1:2	6	**Subgroup 85**	60	1.5	0.5	1, 3, 5	0–120
			Subgroup 86	60	1.5	0.7	1, 3, 5	0–120
			Subgroup 87	60	1.0	0.5	1, 3, 5	0–120
			Subgroup 88	60	1.0	0.7	1, 3, 5	0–120
			Subgroup 89	60	0.5	0.5	1, 3, 5	0–120
			Subgroup 90	60	0.5	0.7	1, 3, 5	0–120
			Subgroup 91	30	1.5	0.5	1, 3, 5	0–120
			Subgroup 92	30	1.5	0.7	1, 3, 5	0–120
			Subgroup 93	30	1.0	0.5	1, 3, 5	0–120
			Subgroup 94	30	1.0	0.7	1, 3, 5	0–120
			Subgroup 95	30	0.5	0.5	1, 3, 5	0–120
			Subgroup 96	30	0.5	0.7	1, 3, 5	0–120
Group 9	1:2	9	**Subgroup 97**	60	1.5	0.5	1, 3, 5	0–120
			Subgroup 98	60	1.5	0.7	1, 3, 5	0–120
			Subgroup 99	60	1.0	0.5	1, 3, 5	0–120
			Subgroup 100	60	1.0	0.7	1, 3, 5	0–120
			Subgroup 101	60	0.5	0.5	1, 3, 5	0–120
			Subgroup 102	60	0.5	0.7	1, 3, 5	0–120
			Subgroup 103	30	1.5	0.5	1, 3, 5	0–120
			Subgroup 104	30	1.5	0.7	1, 3, 5	0–120
			Subgroup 105	30	1.0	0.5	1, 3, 5	0–120

			Subgroup 106	30	1.0	0.7	1, 3, 5	0–120
			Subgroup 107	30	0.5	0.5	1, 3, 5	0–120
			Subgroup 108	30	0.5	0.7	1, 3, 5	0–120
Group 10	1:3	3	**Subgroup 109**	60	1.5	0.5	1, 3, 5	0–120
			Subgroup 110	60	1.5	0.7	1, 3, 5	0–120
			Subgroup 111	60	1.0	0.5	1, 3, 5	0–120
			Subgroup 112	60	1.0	0.7	1, 3, 5	0–120
			Subgroup 113	60	0.5	0.5	1, 3, 5	0–120
			Subgroup 114	60	0.5	0.7	1, 3, 5	0–120
			Subgroup 115	30	1.5	0.5	1, 3, 5	0–120
			Subgroup 116	30	1.5	0.7	1, 3, 5	0–120
			Subgroup 117	30	1.0	0.5	1, 3, 5	0–120
			Subgroup 118	30	1.0	0.7	1, 3, 5	0–120
			Subgroup 119	30	0.5	0.5	1, 3, 5	0–120
			Subgroup 120	30	0.5	0.7	1, 3, 5	0–120
Group 11	1:3	6	**Subgroup 121**	60	1.5	0.5	1, 3, 5	0–120
			Subgroup 122	60	1.5	0.7	1, 3, 5	0–120
			Subgroup 123	60	1.0	0.5	1, 3, 5	0–120
			Subgroup 124	60	1.0	0.7	1, 3, 5	0–120
			Subgroup 125	60	0.5	0.5	1, 3, 5	0–120
			Subgroup 126	60	0.5	0.7	1, 3, 5	0–120
			Subgroup 127	30	1.5	0.5	1, 3, 5	0–120
			Subgroup 128	30	1.5	0.7	1, 3, 5	0–120
			Subgroup 129	30	1.0	0.5	1, 3, 5	0–120
			Subgroup 130	30	1.0	0.7	1, 3, 5	0–120
			Subgroup 131	30	0.5	0.5	1, 3, 5	0–120
			Subgroup 132	30	0.5	0.7	1, 3, 5	0–120
Group 12	1:3	9	**Subgroup 133**	60	1.5	0.5	1, 3, 5	0–120
			Subgroup 134	60	1.5	0.7	1, 3, 5	0–120
			Subgroup 135	60	1.0	0.5	1, 3, 5	0–120
			Subgroup 136	60	1.0	0.7	1, 3, 5	0–120
			Subgroup 137	60	0.5	0.5	1, 3, 5	0–120
			Subgroup 138	60	0.5	0.7	1, 3, 5	0–120
			Subgroup 139	30	1.5	0.5	1, 3, 5	0–120
			Subgroup 140	30	1.5	0.7	1, 3, 5	0–120
			Subgroup 141	30	1.0	0.5	1, 3, 5	0–120
			Subgroup 142	30	1.0	0.7	1, 3, 5	0–120
			Subgroup 143	30	0.5	0.5	1, 3, 5	0–120
			Subgroup 144	30	0.5	0.7	1, 3, 5	0–120

Appendix C

Table C1 Maximum safe train speeds for cases in Set II models.

Group	Subgroup	Maximum safe train speed v (km/h)		
		Joint length l (m)		
		1	3	5
Group 7	Subgroup 73	120	120	120
	Subgroup 74	120	120	120
	Subgroup 75	120	120	120
	Subgroup 76	120	120	120
	Subgroup 77	120	120	120
	Subgroup 78	120	120	48
	Subgroup 79	120	120	120
	Subgroup 80	120	120	120
	Subgroup 81	120	120	88
	Subgroup 82	120	120	56
	Subgroup 83	120	48	–
	Subgroup 84	120	–	–
Group 8	Subgroup 85	120	120	120
	Subgroup 86	120	120	120
	Subgroup 87	120	120	120
	Subgroup 88	120	120	120
	Subgroup 89	120	120	120
	Subgroup 90	120	120	–
	Subgroup 91	120	120	120
	Subgroup 92	120	120	112
	Subgroup 93	120	120	80
	Subgroup 94	120	120	40
	Subgroup 95	120	–	–
	Subgroup 96	120	–	–
Group 9	Subgroup 97	120	120	120
	Subgroup 98	120	120	120
	Subgroup 99	120	120	120
	Subgroup 100	120	120	120
	Subgroup 101	120	120	120
	Subgroup 102	120	120	–
	Subgroup 103	120	120	32
	Subgroup 104	120	120	8
	Subgroup 105	120	120	–

	Subgroup 106	120	64	–
	Subgroup 107	120	–	–
	Subgroup 108	120	–	–
Group 10	**Subgroup 109**	120	120	120
	Subgroup 110	120	120	120
	Subgroup 111	120	120	120
	Subgroup 112	120	120	120
	Subgroup 113	120	120	120
	Subgroup 114	120	120	40
	Subgroup 115	120	120	120
	Subgroup 116	120	120	104
	Subgroup 117	120	120	–
	Subgroup 118	120	120	–
	Subgroup 119	120	32	–
	Subgroup 120	120	–	–
Group 11	**Subgroup 121**	120	120	120
	Subgroup 122	120	120	120
	Subgroup 123	120	120	120
	Subgroup 124	120	120	120
	Subgroup 125	120	120	120
	Subgroup 126	120	120	–
	Subgroup 127	120	120	120
	Subgroup 128	120	120	96
	Subgroup 129	120	120	–
	Subgroup 130	120	120	–
	Subgroup 131	120	–	–
	Subgroup 132	120	–	–
Group 12	**Subgroup 133**	120	120	120
	Subgroup 134	120	120	120
	Subgroup 135	120	120	120
	Subgroup 136	120	120	120
	Subgroup 137	120	120	120
	Subgroup 138	120	120	–
	Subgroup 139	120	120	24
	Subgroup 140	120	120	–
	Subgroup 141	120	120	–
	Subgroup 142	120	32	–
	Subgroup 143	120	–	–
	Subgroup 144	120	–	–